

A Green's Function - Bethe-Salpeter Equation Approach to Investigate the Electronic Structure of First-Row Transition Metal Complexes

by Florian Bogdain
born 11.04.2000 in Eberswalde



Thesis submitted for the degree of
Master of Science (M. Sc.)

Faculty of Mathematics and Natural Sciences
University of Rostock

Supervisor: Prof. Dr. Oliver Kühn, University of Rostock

1. Examiner: Prof. Dr. Oliver Kühn, University of Rostock

2. Examiner: Prof. Dr. Stefan Lochbrunner, University of Rostock

Rostock, 30th of August 2024

Abstract

Climate change is pushing humankind to seek alternative and renewable ways to meet their growing energy demands. Catalytic reactions, such as water splitting into molecular hydrogen and oxygen, offer a promising solution to this problem, as molecular hydrogen is capable of filling this gap. A key role in these reactions is played by transition metal complexes, as they exhibit Metal-to-Ligand Charge Transfer (MLCT) states, which can initiate electron transfers. They may not only be used to drive catalytic reactions, which produce molecular hydrogen but also are applicable to be used in dye-synthesized solar cells. In either way, they work as photosynthesizers, first absorbing sunlight and then driving the reaction. So far, only rare-earth materials, such as ruthenium, have been used, which significantly increases costs. Complexes made of first-row transition metals, such as cobalt, iron, or copper, are promising candidates to replace these expensive materials, decrease the overall cost, and consequently increase the effectiveness of this procedure. Unfortunately, a change in the central metal comes with an altered electronic structure, which leads to their MLCT states being depopulated quickly after excitation.

Therefore, current research is focusing on making chemical modifications to the ligand structure to prolong these lifetimes and make catalytic reactions feasible. Without proper theoretical models, one lacks a deeper understanding of the mechanisms and cannot develop a strategy to investigate future candidates. Unfortunately, commonly used wavefunction or density functional theory methods reach their limits, as these systems exhibit a complex electronic structure and involve many atoms. This work attempts an alternative approach to investigate the electronic structure of these systems using Green's Function and the Bethe-Salpeter Equation. They show good results, eliminating common problems that occur when working with the density functional theory framework. Additionally, they come at acceptable computational costs thus enabling screening of different complexes and paving the way for future molecular dynamics simulations.

Kurzzusammenfassung

Der Klimawandel zwingt die Menschheit dazu, nach alternativen und erneuerbaren Wegen zur Deckung ihres Energiebedarfs zu suchen. Katalytische Reaktionen, bei denen Wasser in molekularen Wasserstoff und Sauerstoff aufgespalten wird, bieten eine vielversprechende Lösung für dieses Problem, da molekularer Wasserstoff in der Lage ist, diese Lücke zu schließen. Eine Schlüsselrolle bei diesen Reaktionen spielen Übergangsmetallkomplexe, da sie über Metall-zu-Ligand-Ladungstransfer (engl. Metal-to-Ligand-Charge-Transfer, MLCT) Zustände verfügen, welche einen Elektronentransfer einleiten kann. Zudem können sie nicht nur für katalytische Reaktionen verwendet werden, bei denen molekularer Wasserstoff erzeugt wird, sondern auch in Farbstoffsolarzellen, sogenannte Grätzel-Zellen, eingesetzt werden. In beiden Fällen wirken sie als Photosynthesizer, welche zunächst das Sonnenlicht absorbieren und dann die Reaktion in Gang setzen. Bisher wurden nur seltene Erden wie Ruthenium verwendet, was die Kosten erheblich erhöht. Komplexe aus Übergangsmetallen der ersten Reihe, wie Kobalt, Eisen oder Kupfer, sind vielversprechende Kandidaten, um diese teuren Materialien zu ersetzen, die Gesamtkosten zu senken und folglich die Effektivität dieses Verfahrens zu erhöhen. Leider geht ein Wechsel des zentralen Metalls mit einer veränderten elektronischen Struktur einher, was dazu führt, dass ihre MLCT-Zustände nach der Anregung schnell entvölkert werden.

Daher konzentriert sich die derzeitige Forschung auf die chemische Veränderung der Ligandenstruktur, um diese Lebenszeiten zu verlängern und katalytische Reaktionen zu ermöglichen. Ohne geeignete theoretische Modelle fehlt es an einem tieferen Verständnis der Mechanismen und man kann keine Strategie zur Untersuchung künftiger Kandidaten entwickeln. Leider stoßen die üblicherweise verwendeten Methoden der Wellenfunktions- oder Dichtefunktionaltheorie an ihre Grenzen, da diese Systeme eine komplexe elektronische Struktur aufweisen und viele Atome beteiligt sind. In dieser Arbeit wird ein alternativer Ansatz zur Untersuchung der elektronischen Struktur dieser Systeme unter Verwendung der Greenschen Funktion und der Bethe-Salpeter-Gleichung versucht. Sie zeigen gute Ergebnisse und beseitigen die üblichen Probleme, die bei der Arbeit mit der Dichtefunktionaltheorie auftreten. Darüber hinaus sind sie mit akzeptablen Rechenkosten verbunden, was die Untersuchung verschiedener Komplexe ermöglicht und den Weg für zukünftige Molekulardynamiksimulationen ebnet.

Abbreviations and Mathematical Symbols

Abbreviation	Description
MLCT	Metal-to-Ligand Charge Transfer
LMCT	Ligand-to-Metal Charge Transfer
MC	Metal Centered
LC	Ligand Centered
LLCT	Ligand-to-Ligand Charge Transfer
IC	Internal Conversion
ISC	Intersystem Crossing
PES	Potential Energy Surface
DFT	Density Functional Theory
TD-DFT	Time-Dependent Density Functional Theory
HF	Hartree Fock
CASSCF	Complete Active Space Self-Consistent Field
CASPT2	Complete Active Space Second-Order Perturbation Theory
ADC(2)	Second Order Algebraic Diagrammatic Construction
MP2	Second Order Møller-Plesset Perturbation Theory
CC	Coupled Cluster
G_0W_0	A Single GW Iteration
evGW	Eigenvalue-Only Self Consistent GW Scheme
BSE	Bethe-Salpeter Equation
CBSE	Correlation augmented Bethe-Salpeter Equation
GW-BSE	Combination of Green's Function and the Bethe-Salpeter Equation
2c-	Two-Component
TDA	Tamm-Dancoff Approximation
SOC	Spin-Orbit Coupling
LVC	Linear Vibronic Coupling
AO	Atomic Orbital
MO	Molecular Orbital
LO	Localized Orbital
HOMO	Highest Occupied Molecular Orbital
LUMO	Lowest Unoccupied Molecular Orbital
occ.	occupied Orbitals
virt.	virtual Orbitals

Symbol	Description
\hat{H}	Many Body Hamiltonian
$\hat{h}(x)$	One-Particle Hamiltonian
$ \Psi_0^N\rangle, N\rangle$	N-Particle Groundstate
$\hat{\psi}(x, t), \hat{\psi}^\dagger(x, t)$	Fermionic Field Annihilation, Creation Operators
\overline{A}	Matrix A
$\text{Tr}[\overline{A}]$	Trace of \overline{A}
$[\hat{A}, \hat{B}]$	Commutator of \hat{A} and \hat{B}
$\{\hat{A}, \hat{B}\}$	Anti Commutator of \hat{A} and \hat{B}
$\Theta(t - t')$	Step Function
$\delta(x - x')$	Delta Distribution
\hat{T}	Time-Ordering Operator
t^+	Shift to an infinitesimal later Time
$G(1, 2)$	One-Particle Green's Function
$G_0(1, 2)$	Non-Interacting One-Particle Green's Function
$G_2(1, 2; 3, 4)$	Two-Particle Green's Function
$M(1, 2)$	Mass Operator
$\Sigma(1, 2)$	Self-Energy Operator
$V(1)$	Hartree Potential
$\Sigma^X(1, 2)$	Exchange Part of the Self-Energy Operator, Fock Exchange
$\Sigma^C(1, 2)$	Correlation Part of the Self-Energy Operator
$\hat{U}_0(t, t')$	Unperturbed Time Evolution Operator
$\hat{U}(t, t')$	Perturbed Time Evolution Operator
$v(x - x')$	Coulomb Potential
$W(1, 2)$	Screened Coulomb Potential
$P(1, 2)$	Polarisation
$\Gamma(1, 2; 3)$	Vertex Function
$L(1, 2; 3, 4)$	Two-Particle Correlation Function
$\Theta(1, 2; 3, 4)$	Bethe-Salpeter Kernel
$\chi(\omega)$	Susceptibility
$\gamma(x, x')^{P,Q}$	Transition Density Matrix from State P to Q
$X(x, x')_{ia}^{P,Q}, Y(x, x')_{ia}^{P,Q}$	Response Vectors between State P and Q in a Molecular Orbital Basis
κ_i^P	Intrastate Coupling Constant for State P
$\lambda_i^{P,Q}$	Interstate Coupling Constant between State P and Q
$\xi_{P,Q}$	Spin-Orbit Coupling Matrix Element

Table of Contents

1	Introduction	1
1.1	Metal Complexes in the Realm of Photocatalysis	1
1.2	The Problem with the MLCT Lifetime	1
2	Theory	5
2.1	Introduction to Green's Functions in the Context of Quantum Field Theory . . .	5
2.2	Lehman Representation	6
2.3	Equation of Motion	6
2.4	Dyson Equation	7
2.5	Hedin's Equations	9
2.5.1	The Quasiparticle Picture	12
2.5.2	Spectral Method and GW Approximation	13
2.5.3	Contour Deformation Techniques	14
2.6	Bethe Salpeter Equation	16
2.6.1	"Casida-like" Equation	16
2.6.2	Tamm Dancoff Approximation and Correlation Augmented BSE	20
2.6.3	Transition Density Matrices	21
2.7	Linear Vibronic Coupling Model	22
2.8	Spin-Orbit Coupling	24
2.9	Computational Details and LVCM Implementation	25
3	Electronic Structure Analysis of different Systems	27
3.1	Long-Range Behavior of Charge-Transfer-States	27
3.2	Assesment of Computational Cost	29
3.3	The Accuracy of MC-States for Systems with Triazacyclononane Ligands	30
3.3.1	Iron(II)	32
3.3.2	Cobalt(III)	33
3.3.3	Chrom(III)	34
3.3.4	Nickel(III)	36
3.3.5	Cobalt(II)	38
3.4	MLCT-States of closed shell Fe(II) Complexes	40
3.5	The Inclusion of Spin-Orbit Coupling	46
3.5.1	Two-component GW-BSE	46
3.5.2	Perturbative Approach to Spin-Orbit Coupling	49
3.6	GW-BSE-LVC Model for Pyrazine	50
3.7	Structure of the Potential Energy Surface and LVC Parameterization for a closed-shell Fe Complex	52
4	Conclusion and Outlook	61

5 Appendix	63
5.1 Equation of Motion	63
5.2 Derivative of Field Operators	66
5.3 Separation of the Mass Operator	67
5.4 Derivation of the screened Coulomb Potential	69
5.5 Derivation of Vertex Function	70
5.6 Derivative of Green's Function	71
5.7 Fock Term of the Self-Energy Operator	72
5.8 First Order Response of the Transition Density Matrix	73
5.9 BSE in Fourier Space	76
5.10 LVC Model for a mixed def2-SVP/def2-TZVP basis set	77
Bibliography	77
Acknowledgements	87
Statement of Authorship	89

1 Introduction

1.1 Metal Complexes in the Realm of Photocatalysis

Climate change is among the most important challenges humankind faces in the foreseeable future.^[1] For this reason, a strong emphasis is put on research that focuses on developing new methods to sustain our future economy. For instance, molecular hydrogen has demonstrated its ability to offer solutions to the ever-growing global energy demand.^{[2] [3]} One question that modern research has to answer in this field is related to environmentally friendly hydrogen production. Photocatalytic reactions involving transition metal complexes are a promising method in this respect. However, these systems come with problems of their own, centered around low yields, unsatisfactory stability of the process, and the low abundance of rare earth materials required by the molecular systems.^[4] These problems pose new challenges that need to be addressed theoretically and experimentally, especially as the recent movement is pushing to replace rare-earth materials with more readily available first-row transition metals.^[5] This step is required by the economic advantage of more readily available materials, however, it comes with the challenge of a significantly altered electronic structure. Transition metal complexes are commonly utilized as photosensitizers, meaning they initiate the catalytic process through an electron transfer after light absorption.^[6] This means that the fundamental understanding of processes occurring after photoexcitation is a key factor. Therefore, experimentalists and theoreticians study dynamic processes, through different means. Experimentalists usually refer to time-resolved spectroscopy methods such as pump-probe experiments or time-resolved luminescence measurements to investigate these systems.^[7] Theoreticians on the other hand can resort to dynamics simulations involving classical trajectory surface hopping techniques or quantum mechanical wave packet dynamics requiring accurate potential energy surfaces.^{[8] [9]} Regardless of the chosen method, it is clear that an accurate understanding of the excited state properties of these systems is necessary to push for advancements in this field of study. In the case of transition metal complexes, commonly employed levels of theory are pushed to their limits. Wavefunction-based methods, such as Complete Active Space Self-Consistent Field (CASSCF), come at immense computational costs, due to the large size of these systems and the number of electrons one has to include. Density Functional Theory (DFT), on the other hand, lacks in many cases the necessary accuracy and shows a strong dependence on the functional and the type of electronic transition.^[10] Altogether, this increases the demand for new methods that are computationally inexpensive yet accurate enough to effectively describe these systems.

This work will be structured in the following way: First, important properties related to transition metal complexes as a whole will be discussed and we will highlight specific aspects we want to investigate. Second, we will introduce the Green's Function Bethe-Salpeter-Equation (GW-BSE) approach, as an alternative to the above-mentioned levels of theory. In the last part, we will investigate individual aspects, such as the dependence on the type of electronic transition or the effects of spin-orbit coupling, step by step, paving the way for possible GW-BSE dynamics simulations using a linear vibronic coupling model.

1.2 The Problem with the MLCT Lifetime

Many physical and chemical properties of transition metal complexes may already be understood using simple models. For instance, Ligand Field Theory already explains that the partially filled d-orbitals of the central metal are not degenerated anymore, due to the presence of the charged ligands.^[11] The splitting between the d orbitals depends on the ligand

field strength and geometry, which means that it is tunable if chemical modifications to the ligands are made. This also has the consequence, that the spin state of metal complexes can be variable. In this study, we will focus on closed-shell ligand systems. However, variations in field strength can influence the electronic configuration. For instance, a strong ligand field may lead to a full occupation of the energetically lower orbitals called t_{2g} , resulting in a low-spin closed-shell configuration. Alternatively, a low field strength usually results in a high spin open-shell configuration, as certain d-orbitals are only partially occupied.^[12] This may also include the energetically higher d-orbitals called e_g . Because of this splitting and additional orbitals localized on the ligand, many different types of electronic transitions are possible. Generally one distinguishes between Metal-Centered- (MC), Ligand-Centered- (LC), Metal-to-Ligand-Charge-Transfer- (MLCT), Ligand-to-Metal-Charge-Transfer- (LMCT), and Ligand-to-Ligand-Charge-Transfer (LLCT) states. This tells one that electronic transitions can occur upon light absorption where electron density either remains near the metal/ligand (MC-/LC transitions) or shifts to the corresponding other region (charge transfer transition). For catalysis, one is particularly interested in the accurate description of charge transfer states, as these are afterwards capable of performing electron transfers.^[13]

A problem now arises with the MLCT lifetime. For most complexes, the MLCT state of interest is not the lowest excited state, meaning its population may decay via intersystem crossing (ISC) or internal conversion (IC) into lower-lying states. The excited MLCT state tends to decay rapidly into MC states which may nonradiatively decay and thus cannot be used for further catalytic reactions. This is especially true for first-row transition metal complexes, as their 3d orbitals are low in energy and the ligand field splitting depends on the principle quantum number n . This has a direct impact on the potential energy surfaces of these states, resulting in a crossing point of the MLCT and MC state that is closer to the MLCT equilibrium position. This will result in a fast transfer according to Marcus theory.^[14] This entire process is depicted in figure 1.1.

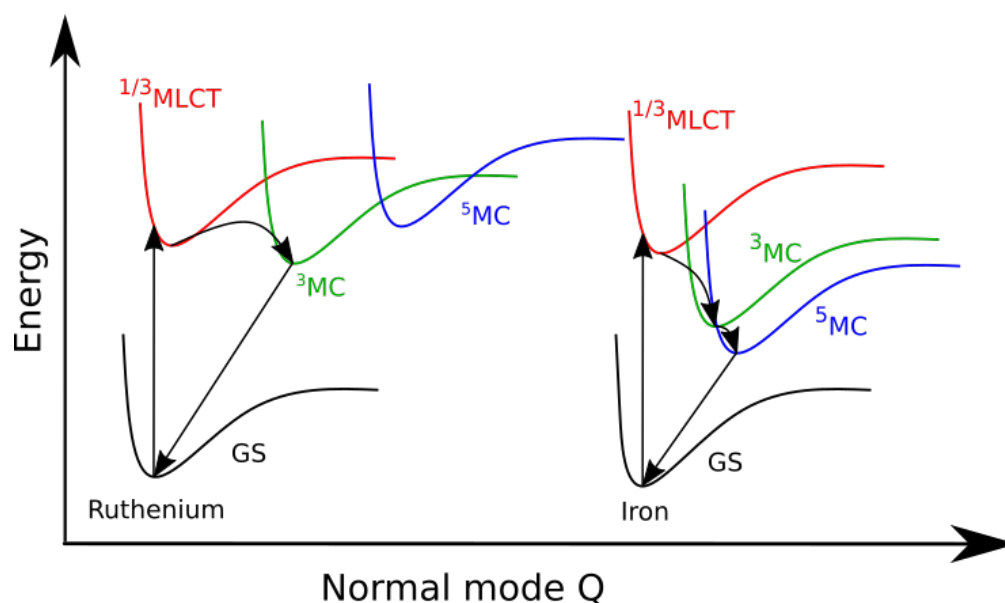


Figure 1.1: Sketch of the potential energy surface along a normal mode Q for two different complexes. For ruthenium, the split d-orbitals (e_g) are high in energy, relative to the π orbitals of the ligand. This means that all MC states are also higher in energy. This lowers significantly the rate at which the MLCT is depleted. In contrast, the iron complex exhibits low-lying MC states which cause the population from the MLCT state to transfer to them.^[15]

As mentioned before, a sufficiently long lifetime is required to drive any catalytic reaction. For Ruthenium, the corresponding MLCT states are long-lived since the MC states lie high in energy. In the case of first-row transition metal, these states are lower in energy and consequently deplete the MLCT state within picoseconds, which means that the system lacks the required time for electron transfers to happen.^[16] In order to make these reactions feasible, one attempts to make chemical modifications to the ligand shifting the MC states upwards in energy. Without proper theoretical models, this resembles a needle in a haystack problem, as there are infinite possibilities to make changes to the ligand structure. For this reason, theories need to be as accurate as possible to make predictions about future candidates. Unfortunately, the well-established methods mentioned above come with their respective weaknesses, so alternative methods are being investigated intensively. A promising new framework combines Green's Function and the Bethe-Salpeter Equation. This combined approach produces notably strong results in the realm of solid-state physics, that align well with experimental data.^[17] Unfortunately, this theory is not well-established in the fields of quantum chemistry and molecular physics. Therefore, this work aims to fill this gap by exploring its potential in this complex area of photocatalysis.

2 Theory

The GW-BSE method is already well-established in the field of solid-state physics.^[18] In contrast, its applications in quantum chemistry remain scarce, despite its potential as a promising alternative to commonly used DFT calculations. Unfortunately, there exists almost no comprehensive step-by-step derivation of the entire framework, which is what we will present in this chapter. It will summarize the most important steps, however technical details, such as the evaluation of commutators, integrals, or functional derivatives are provided in the appendix.

2.1 Introduction to Green's Functions in the Context of Quantum Field Theory

Before deriving the essential theory used in this work, one has to define the most important object of this framework, **the Green's Function**. Green's Functions are a well-known concept in the area of partial differential equations. There, they are the function that produces a delta distribution if its corresponding differential operator acts on the Green's Function.^[19] This yields an important tool to investigate partial differential equations more broadly, for all possible inhomogeneities.

Here one has to focus on the physical properties of the Green's Function in the context of Quantum Field Theory, however, we will justify the name later. One works in second quantization, which means one has to introduce the fermionic creation- and annihilation operator $\hat{\psi}^\dagger(x, t)$ and $\hat{\psi}(x, t)$. They act on the N -particle state $|\Psi_0^N\rangle$ and raise or lower the number of fermions in the system by one each while maintaining normalization. This means they obey the following two expressions and an anti-commutator relation^[20]

$$\begin{aligned}\hat{\psi}^\dagger(x, t) |\Psi_0^N\rangle &= \frac{1}{\sqrt{N+1}} |\Psi_0^{N+1}\rangle \\ \hat{\psi}(x, t) |\Psi_0^N\rangle &= \sqrt{N} |\Psi_0^{N-1}\rangle\end{aligned}\quad (2.1)$$

$$\{\hat{\psi}(x, t), \hat{\psi}^\dagger(x', t')\} = \delta(x - x')\delta(t - t')\hat{1}. \quad (2.2)$$

With these operators, one defines the Green's Function in the following way^[21]

$$iG(x, t, x', t') = \langle \Psi_0^N | \hat{\mathcal{T}} [\hat{\psi}(x, t)\hat{\psi}^\dagger(x', t')] | \Psi_0^N \rangle. \quad (2.3)$$

Here we use the time ordering operator $\hat{\mathcal{T}}$ and the Heisenberg picture by shifting the time dependence into the annihilation field operator¹

$$\hat{\psi}(x, t) = e^{i\hat{H}t}\hat{\psi}(x)e^{-i\hat{H}t}. \quad (2.4)$$

In this context, the Green's Function describes the probability amplitude that one particle is created at (x', t') , propagated in space-time, and ultimately destroyed at (x, t) .^[22] The time ordering operator allows one to consider both possible scenarios where $t' > t$ and $t > t'$. This means that one Green's Function can describe the dynamics of both an electron and a hole at the same time. This information can also be expressed using the step function $\Theta(t - t')$

$$iG(x, t, x', t') = \langle \Psi_0^N | \Theta(t - t')\hat{\psi}(x, t)\hat{\psi}^\dagger(x', t') - \Theta(t' - t)\hat{\psi}^\dagger(x', t')\hat{\psi}(x, t) | \Psi_0^N \rangle. \quad (2.5)$$

¹An equivalent expression for the creation operator can be derived by taking the adjoint of equation (2.4).

2.2 Lehman Representation

With the definition set, one is now in a position to calculate the spectral (or also called Lehman-) representation of the Green's Function. To do so, one starts by inserting $\hat{1} = \sum_k |\Psi_k^N\rangle \langle \Psi_k^N|$ and using the relations (2.1) and (2.2). This will yield the following expression where the first term sums over all virtual and the second term over all occupied orbitals

$$iG(x, t, x', t') = \sum_{m=0}^{virt.} e^{i(E^N - E_m^{N+1})(t-t')} \Theta(t-t') g_m(x) g_m^*(x') - \sum_{l=0}^{occ.} e^{i(E^N - E_l^{N-1})(t'-t)} \Theta(t'-t) f_l(x') f_l^*(x). \quad (2.6)$$

In the equation above the Lehman amplitudes

$g_m(x) = \langle \Psi_0^N | \hat{\psi}(x) | \Psi_m^{N+1} \rangle$ and $f_l(x) = \langle \Psi_l^{N-1} | \hat{\psi}(x) | \Psi_0^N \rangle$ have been defined.

To switch over to the frequency domain, one can now insert the spectral representation of the step function

$$\Theta(t-t') = \mp \lim_{\eta \rightarrow 0} \int \frac{d\omega}{2\pi i} \frac{e^{\mp i\omega(t-t')}}{\omega \pm i\eta}. \quad (2.7)$$

In the following, one drops the limit and sets η to a finite value. After a change of the integral variable, one can identify the Fourier transform of the Green's Function as follows

$$G(x, x', \omega) = \sum_{l=0}^{occ.} \frac{f_l(x) f_l^*(x')}{\omega + (E_l^{N-1} - E_0^N) - i\eta} + \sum_{m=0}^{virt.} \frac{g_m(x') g_m^*(x)}{\omega - (E_m^{N+1} - E_0^N) + i\eta}. \quad (2.8)$$

This expression demonstrates that the Green's Functions includes information about the ionization energies, as well as the electron affinities. One can observe that it is possible to obtain them by searching for poles of G in the complex plane. The construction of G is also possible by calculating these energies along with their respective amplitudes in advance. Furthermore, the position of these energies is well separated, since their position in the complex plane is determined by the sign in front of the $i\eta$ term. All ionization energies will be in the upper half-plane and all electron affinities will be in the lower half-plane of the complex plane.^[23]

2.3 Equation of Motion

To investigate the Green's Function more systematically, one can derive an equation of motion, which we will later use to obtain Hedin's Equations in chapter 2.5. At first, one writes down the general many-particle Hamiltonian for our system, consisting of the one-electron Hamiltonian $h(x)$ and the electron-electron interaction $v(x-x') = \frac{1}{|x-x'|}$ in atomic units.

$$\hat{H} = \int dx \hat{\psi}^\dagger(x) h(x) \hat{\psi}(x) + \frac{1}{2} \iint dx_1 dx_2 \hat{\psi}^\dagger(x_1) \hat{\psi}^\dagger(x_2) v(x_1 - x_2) \hat{\psi}(x_2) \hat{\psi}(x_1) \quad (2.9)$$

At this point, one usually shortens the notation by using $(k) = (x_k, t_k)$, $k \in \mathbb{N}$ and $|N\rangle = |\Psi_0^N\rangle$.² This means that the expression for the Green's Function (2.3) from earlier reduces to

$$iG(1, 2) = \langle N | \hat{T} [\hat{\psi}(1) \hat{\psi}^\dagger(2)] | N \rangle. \quad (2.10)$$

²For us, the natural numbers begin at 1.

Now one takes the derivative of this whole expression, paying attention to the product rule.

$$i \frac{\partial G(1, 2)}{\partial t_1} = \frac{\partial \Theta(t_1 - t_2)}{\partial t_1} \langle N | \hat{\psi}(1) \hat{\psi}^\dagger(2) | N \rangle - \frac{\partial \Theta(t_2 - t_1)}{\partial t_1} \langle N | \hat{\psi}^\dagger(2) \hat{\psi}(1) | N \rangle + \langle N | \hat{\mathcal{T}} \left[\frac{\partial \hat{\psi}(1)}{\partial t_1} \hat{\psi}^\dagger(2) \right] | N \rangle \quad (2.11)$$

Each term now has to be calculated separately, where the derivative of the step function yields a delta distribution. An expression for the derivative of field operators can be found by making use of the equation of motion in the Heisenberg picture $i \frac{\partial \hat{\psi}(1)}{\partial t_1} = [\hat{\psi}(1), \hat{H}]$.^[20]

$$i \frac{\partial \hat{\psi}(1)}{\partial t_1} = e^{i\hat{H}t_1} \left[h(x_1) \hat{\psi}(x_1) + \int dx_2 v(x_1 - x_2) \hat{\psi}^\dagger(x_2) \hat{\psi}(x_2) \hat{\psi}(x_1) \right] e^{-i\hat{H}t_1} \quad (2.12)$$

A more detailed derivation is given in the appendix 5.1. After inserting equation (2.12) into (2.11), one can find the following expression³

$$\left(i \frac{\partial}{\partial t_1} - h(1) \right) G(1, 2) - \int d3 M(1, 3) G(3, 2) = \delta(1, 2). \quad (2.13)$$

Here one already introduced the mass operator

$$M(1, 4) = -i \iint d3 d2 v(1, 3) G_2(1, 3; 2, 3^+) G^{-1}(2, 4) \quad (2.14)$$

, which accounts for all kinds of interactions between two particles. It is defined via the two-particle Green's Function

$$i^2 G_2(1, 3; 2, 3^+) = \langle N | \hat{\mathcal{T}} \left[\hat{\psi}(1) \hat{\psi}^\dagger(3^+) \hat{\psi}(3) \hat{\psi}^\dagger(2) \right] | N \rangle. \quad (2.15)$$

The 3^+ refers to an infinitesimal shift to later times, to produce the correct result from equation (2.12). The Coulomb potential has been replaced with $v(1, 3) = v(x_1, x_3) \delta(t_1, t_3)$, which means that the interaction is instantaneous. The mass operator contains all information about the electron-electron, exchange, and correlation interaction. As can be seen, if M were to be known, one can solve this equation to obtain G .

2.4 Dyson Equation

With the equation of motion at hand, it is now possible to find an expression that is more suitable for calculations. However first, one can separate the Hartree potential from the mass operator by making the following definition

$$M(1, 2) = V(1, 2) + \Sigma(1, 2). \quad (2.16)$$

Through this way the Hartree potential $V(1, 2) = V(1) \delta(1, 2)$ and the self-energy operator $\Sigma(1, 2)$ have been introduced.⁴ The latter includes all exchange and correlation effects that go beyond the Hartree exchange.^[24] In the next chapter, we will examine these terms in greater detail, to derive a more explicit expression to justify this separation.

For now one continues by inserting this definition into the equation of motion (2.13), which

³ $h(k) = h(x_k)$, $\delta(k, k') = \delta(x_k - x_{k'}) \delta(t_k - t_{k'})$ and $dk = dx_k dt_k$ for $k, k' \in \mathbb{N}$.

⁴Please note that the definitions vary a lot. In particular, it is also popular to define the self-energy operator as the sum of the Hartree potential and the mass operator^[22]

will lead to

$$\left(i\frac{\partial}{\partial t_1} - h(1) - V(1)\right)G(1,2) - \int d3\Sigma(1,3)G(3,2) = \delta(1,2). \quad (2.17)$$

We now assume a non-interacting Green's Function $G_0(1,2)$ by setting $\Sigma = 0$ in equation (2.17) resulting in

$$\left(i\frac{\partial}{\partial t_1} - h(1) - V(1)\right)G_0(1,2) = \delta(1,2). \quad (2.18)$$

At this point, it is clear why the name Green's Function is justified, since in the equation (2.18) one can observe a differential operator on the left-hand side, which acts on the Green's Function to generate a delta distribution.

As a next step, one can make use of the relation $\int d2G(3,2)G^{-1}(2,4) = \delta(3,4)$ for any Green's Function^[25], to find the following expression

$$G(1,2) = \int d3\delta(1,3)G(3,2) = \iint d3d4G_0(1,4)G_0^{-1}(4,3)G(3,2). \quad (2.19)$$

After inserting (2.19) into (2.17), this will result in^[26]

$$\iint d3d4\left(i\frac{\partial}{\partial t_1} - h(1) - V(1)\right)G_0(1,4)G_0^{-1}(4,3)G(3,2) - i\int d3\Sigma(1,3)G(3,2) = \delta(1,2). \quad (2.20)$$

One can insert equation (2.18) on the left-hand side, which will allow one to perform one integration.

$$\int d3G_0^{-1}(1,3)G(3,2) - i\int d3\Sigma(1,3)G(3,2) = \delta(1,2) \quad (2.21)$$

This equation can be solved for $G(1,2)$ to obtain the Dyson equation

$$G(1,2) = G_0(1,2) + \iint d3d4G_0(1,3)\Sigma(3,4)G(4,2) \quad (2.22)$$

or

$$G^{-1}(1,2) = G_0^{-1}(1,2) - \Sigma(1,2). \quad (2.23)$$

By using the self-energy operator, it is possible to calculate the full Green's Function from the non-interacting one. As by equation (2.8), one is able to construct $G_0(1,2)$ by simply calculating the ionization potentials and electron affinities of a given system. Therefore, it will later be possible to construct $G_0(1,2)$ through an initial Hartree Fock (HF) or Density Functional Theory (DFT) calculation.^[27] It is also clear that if the Hartree potential has not been taken into account when constructing $G_0(1,2)$, the self-energy operator can be replaced with the mass operator to also include these effects. Nevertheless, all success depends on the existence of an accurate scheme to calculate the self-energy operator or the mass operator, which we will cover in the next chapter.

2.5 Hedin's Equations

As previously stated, the goal of this chapter will be to find a straightforward way to calculate the self-energy Σ . For this, we will follow the derivation done by Lars Hedin.^[28] This will result in a set of equations named after him. To start, one assumes a perturbative potential H_1 , which will later be set to 0.

$$\begin{aligned}\hat{H} &= \hat{H}_0 + \hat{H}_1 \\ \hat{H}_1 &= \int dx \hat{\rho}(x) w(x, t) \\ \hat{\rho}(x) &= \hat{\psi}^\dagger(x) \hat{\psi}(x)\end{aligned}\tag{2.24}$$

In equation (2.4), the time evolution operator $\hat{U}_0(t, t')$ of the unperturbed system was already introduced as

$$\hat{U}_0(t, t') = e^{-i\hat{H}_0 t}.\tag{2.25}$$

Since the perturbation is small, one can make use of perturbation theory, which yields an expression for the perturbed time evolution operator.

$$\hat{U}(t, t') = \hat{U}_0(t, t') - i \int_{t'}^t dt'' \hat{U}_0(t, t'') \hat{H}_1(t'') \hat{U}(t'', t')\tag{2.26}$$

The goal is now to compute the response of the system, for the introduced perturbation \hat{H}_1 . To do so, one starts by calculating the variational derivative of \hat{U} by evaluating

$$\delta \hat{U} = \left[\frac{\partial}{\partial \epsilon} \hat{U}(w + \epsilon \cdot f) \right]_{\epsilon=0} = \iiint dx dt \frac{\delta \hat{U}}{\delta w} f(x, t).\tag{2.27}$$

In equation (2.27), $f(x, t)$ is an arbitrary differentiable function. By performing the evaluations one finds⁵

$$\frac{\delta \hat{U}(t, t')}{\delta w(x, t'')} = -i \text{sgn}(t - t') \Theta(t - t'') \Theta(t'' - t') \hat{U}_0(t, t'') \hat{\rho}(x) \hat{U}(t'', t').\tag{2.28}$$

One uses one again the Heisenberg picture with the convention

$\hat{\psi}(x, t) = \hat{U}(-T_0, t) \hat{\psi}(x) \hat{U}(t, -T_0)$, where T_0 is a large number. By evaluating the commutator of $\hat{\psi}(x)$ with H_1 , one can derive a new equation of motion for this new Hamiltonian, as it was done for equation (2.13). This yields an additional contribution with $w(1)$.⁶

$$\begin{aligned}& \left[i \frac{\partial}{\partial t_1} - h(1) - w(1) \right] \langle N | \hat{T} \left(\hat{\psi}(1), \hat{\psi}^\dagger(2) \right) | N \rangle \\ & - \int dx_3 v(x_1, x_3) \langle N | \hat{T} \left(\hat{\psi}^\dagger(x_3, t_1) \hat{\psi}(x_3, t_1) \hat{\psi}(1) \hat{\psi}^\dagger(2) \right) | N \rangle = \delta(1, 2)\end{aligned}\tag{2.29}$$

One can make use of the following relation to rewrite the expression above in a way that produces a variational derivative of the Green's Function.

$$\begin{aligned}& \frac{\delta}{\delta w(3)} \left[\hat{U}(T_0, -T_0) \left(\Theta(t_1 - t_2) \hat{\psi}(1) \hat{\psi}^\dagger(2) - \Theta(t_2 - t_1) \hat{\psi}^\dagger(2) \hat{\psi}(1) \right) \right] \\ & = -i \hat{U}(T_0, -T_0) \hat{T} \left(\hat{\rho}(3) \hat{\psi}(1) \hat{\psi}^\dagger(2) \right)\end{aligned}\tag{2.30}$$

⁵In the original Hedin paper this expression is linearized to $\hat{U}_0(t, t'') \hat{\rho}(x) \hat{U}_0(t'', t')$

⁶This will also change to Dyson equation to $G^{-1}(1, 2) = G_0^{-1}(1, 2) - \Sigma(1, 2) - \omega(1) \delta(1, 2)$ ^[29]

A detailed derivation is demonstrated in the appendix 5.2. The new Hamiltonian will consequently lead to a new expression for the Green's Function in the following way

$$iG(1, 2) = \frac{\langle N | \hat{U}_0(-T_0, T_0) \hat{U}(T_0, -T_0) \hat{T} \left(\hat{\psi}(1) \hat{\psi}^\dagger(2) \right) | N \rangle}{\langle N | \hat{U}_0(-T_0, T_0) \hat{U}(T_0, -T_0) | N \rangle}. \quad (2.31)$$

These two results can be combined with equation (2.29). This will result in a slightly modified equation of motion when compared to equation (2.13)

$$\left[i \frac{\partial}{\partial t_1} - h(1) - V(1) \right] G(1, 2) - i \int d^3v(1, 3) \frac{\delta}{\delta w(3)} G(1, 2) = \delta(1, 2). \quad (2.32)$$

Here,

$$\begin{aligned} V(1) &= w(1) + \int d^3v(1, 3) \frac{\langle N | \hat{U}_0(-T_0, T_0) \hat{U}(T_0, -T_0) \hat{\rho}(3) | N \rangle}{\langle N | \hat{U}_0(-T_0, T_0) \hat{U}(T_0, -T_0) | N \rangle} \\ &= w(1) - i \int d^3v(1, 3) G(3, 3^+) \end{aligned} \quad (2.33)$$

is the previously introduced Hartree potential.

To simplify the integral expression one can step away for a moment and investigate the following equation which originates from the relation used to derive the Dyson equation (2.22).

$$\begin{aligned} 0 &= \frac{\delta}{\delta w(4)} \int d^3G(1, 3) G^{-1}(3, 2) \\ &= \int d^3 \left[\frac{\delta G(1, 3)}{\delta w(4)} G^{-1}(3, 2) + G(1, 3) \frac{\delta G^{-1}(3, 2)}{\delta w(4)} \right] \end{aligned} \quad (2.34)$$

This equation can be solved for the variational derivative of $G(1, 3)$ to find an elegant way to simplify the integral term in equation (2.32).

$$\frac{\delta G(1, 2)}{\delta w(3)} = - \iint d^4d^5 G(1, 4) \frac{\delta G^{-1}(4, 5)}{\delta w(3)} G(5, 2) \quad (2.35)$$

It is now possible to find an expression for the self-energy operator by inserting (2.35) into (2.32).

$$\left[i \frac{\partial}{\partial t_1} - h(1) - V(1) \right] G(1, 2) - \int d^3 \Sigma(1, 3) G(3, 2) = \delta(1, 2) \quad (2.36)$$

In the equation above, an expression for the self-energy operator $\Sigma(1, 2)$ has been introduced in the following way

$$\Sigma(1, 2) = i \iint d^3d^4v(1, 3) \frac{\delta G^{-1}(1, 4)}{\delta w(3)} G^{-1}(4, 2). \quad (2.37)$$

If one compares this expression to the definition of the self-energy operator as a part of the mass operator in equation (2.16), one can find the following relation

$$\Sigma(1, 2) = -i \iint d^3d^4v(1, 3) G(1, 4) \frac{\delta G^{-1}(4, 2)}{\delta w(3)}. \quad (2.38)$$

This fact, as well as addition steps, are elaborated in the appendix 5.3. At this point, one can introduce the next important quantity in this framework.

$$W(1, 2) = \int d^3v(1, 3) \frac{\delta V(2)}{\delta w(3)} \quad (2.39)$$

$W(1, 2)$ describes the screened Coulomb exchange. This occurs between two quasiparticles, however, this physical interpretation will be discussed in greater detail in the next chapter. For now one has to continue with the calculation of the variational derivative of $W(1, 2)$ since the Hartree potential was already defined in equation (2.33). Therefore, one starts with the derivative of $V(1)$.

$$\frac{\delta V(1)}{\delta w(3)} = \delta(1, 3) - i \int d3 v(1, 3) \frac{\delta G(3, 3^+)}{\delta w(3)} \quad (2.40)$$

Using the chain rule $\frac{\delta}{\delta w(1)} = \int d2 \frac{\delta V(2)}{\delta w(1)} \frac{\delta}{\delta V(2)}$ [29] and by inserting this into equation (2.39), it is possible to write down a compact expression for the screened Coulomb interaction. This step also makes use of equation (2.35). The exact steps are again given in the appendix 5.4. This yields

$$\begin{aligned} W(1, 2) &= v(1, 2) + \iint d3d4 W(1, 3) P(3, 4) v(2, 4) \\ P(2, 4) &= -i \iint d5d6 G(4, 5) G(6, 4) \frac{\delta G^{-1}(5, 6)}{\delta V(2)}. \end{aligned} \quad (2.41)$$

Here, $P(2, 4)$ is called the polarisation. The remaining term, which one cannot calculate directly, is called the vertex function and is defined by

$$\Gamma(1, 2; 3) = -\frac{\delta G^{-1}(1, 2)}{\delta V(3)}. \quad (2.42)$$

To investigate this term one has to rewrite the Dyson equation (2.22) in the following way. [30]

$$G_0^{-1}(1, 2) = G^{-1}(1, 2) + \Sigma(1, 2) + w(1)\delta(1, 2) \quad (2.43)$$

By taking the derivative on both sides, one can observe the vertex function appear on the right-hand side.

$$\frac{\delta G_0^{-1}(1, 2)}{\delta V(3)} = -\Gamma(1, 2; 3) + \frac{\delta \Sigma(1, 2)}{\delta V(3)} \quad (2.44)$$

Rewriting equation (2.18) yields a way of calculating the derivative $\frac{\delta G_0^{-1}(1, 2)}{\delta V(3)} = -\delta(1, 3)\delta(1, 2)$. This is explained in detail in the appendix 5.5. The result is that one can solve (2.44) for the vertex function the following way

$$\Gamma(1, 2; 3) = \delta(1, 2)\delta(1, 3) + \frac{\delta \Sigma(1, 2)}{\delta V(3)}. \quad (2.45)$$

As a final result, we can insert all the derived expressions into equation (2.37) to obtain

$$\Sigma(1, 2) = i \iint d3d4 G(1, 4) W(1, 3) \Gamma(4, 2; 3). \quad (2.46)$$

2.5.1 The Quasiparticle Picture

At this point, it is important to briefly discuss the quantities introduced in the previous chapter. So far we have not made any assumption about the type of particles we want to investigate, besides the fact that fermionic creation and annihilation operators have been used, however, it is clear that the goal of this work is to investigate many-electron systems. We saw in the derivation above that the introduction of the Coulomb interaction between the particles led to the definitions of the screened Coulomb interaction. This is an expected outcome since we switched over to a quasiparticle picture. This has been done in the sense that the Green's Function describes the movement of an electron (or hole) and its interaction with all remaining particles in the system. This Coulomb interaction is however screened due to the polarisation of the medium. This way one obtains a system of particles that consists of electrons (or holes) alongside the positively (or negatively) charged Coulomb cloud they are surrounded by, which yields a quasiparticle. This charged cloud reduces the effectiveness of the Coulomb interaction and will thus result in a weaker force.^{[31] [32]} These quasiparticles will have properties of their own, particularly energy, mass, and lifetime.^[33] Most importantly, through this concept one no longer has to treat all particles individually with their respective interaction with all other particles, but instead this problem reduces to the above-mentioned properties of the quasiparticles.

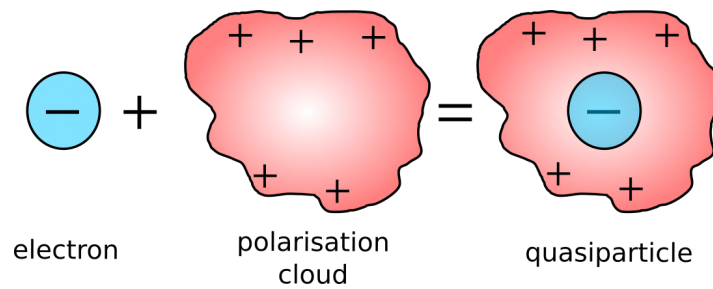


Figure 2.1: Sketch to demonstrate the essential idea behind the quasiparticle concept. Instead of investigating a system of different electrons, one is now interested in quasiparticles that consist of electrons/holes along with their respective polarisation cloud, which screens the Coulomb interaction.^[34]

This makes it also clear why the polarization of the medium affects the screened Coulomb potential since the polarizability of a medium corresponds to its effectiveness at screening an external electric field. The self-energy now includes all possible ways in which quasiparticles can interact with each other. It is important to note that the quasiparticle picture is a tool used to express the complex motions performed by electrons. This concept will break down inside of highly correlated materials.^[35]

2.5.2 Spectral Method and GW Approximation

With Hedin's Equations at our disposal, it will be the next objective to derive a scheme to solve them. A possible approach is in the spectral domain by making use of the GW approximation. The latter can be easily introduced by taking a closer look at the definition of the vertex function in equation (2.45). By assuming that the self-energy does not change with respect to the Hartree potential, one can observe that the expression simplifies to a product of delta distributions.

$$\Gamma^{\text{GW}}(1, 2; 3) = \delta(1, 2)\delta(1, 3) \quad (2.47)$$

This results in us expanding the self-energy in a power series of the screened Coulomb potential but only considering the first term. Inserting this expression into equation (2.41) and (2.46) will allow one to perform the integration, which yields an efficient way to calculate the self-energy, through the polarization.

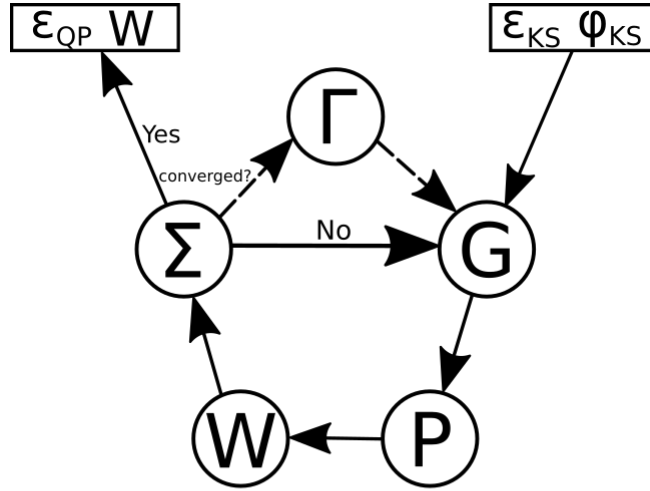
$$\Sigma^{\text{GW}}(1, 2) = iG(1, 2)W(1, 2) \quad (2.48)$$

$$P^{\text{GW}}(1, 2) = -iG(1, 2)G(2, 1) \quad (2.49)$$

$$W^{\text{GW}}(1, 2) = v(1, 2) + \iint d3d4W^{\text{GW}}(1, 3)P^{\text{GW}}(3, 4)v(2, 4) \quad (2.50)$$

One can see the reason behind the name GW-Approximation since the remaining term to calculate the self-energy is simply the product of the Green's Function and the screened Coulomb potential.

If one now remembers the possibility of constructing an initial Green's Function based upon equation (2.8), the next steps become clear. The idea is to start with a first ab initio calculation to generate a set of molecular orbitals. For this it is possible to make use of the HF or DFT method, however, as we will see in the chapter related to the results, the latter is our preferred method of choice. With these, one can calculate an initial set of ionization energies and electron affinities, which serve as a first guess for our quasiparticle energies. If one replaces the Lehmann amplitudes with the molecular orbitals one can calculate an initial Green's Function using equation (2.8). With that, the polarization, screened Coulomb potential, and finally, the self-energy are computed, using equations (2.47) - (2.50). Through the self-energy, it is then possible to solve equation (2.22) to generate a new and ideally improved Green's Function.^[36] From then onwards, one can exit and continue with supplementary calculations or repeat this cycle until convergence is reached. Since all equations are solved in the spectral domain, this approach is called the spectral method. The entire cycle is depicted in the figure 2.2.



$$\begin{aligned}
 G(1,2) &= G_0(1,2) + \int d(3,4) G_0(1,3) \Sigma(3,4) G(4,2) \\
 P(1,2) &= -i \int d(3,4) G(1,3) G(4,1) \Gamma(3,2;4) \\
 W(1,2) &= v(1,2) + \int d(3,4) W(1,3) P(3,4) v(4,2) \\
 \Sigma(1,2) &= i \int d(3,4) G(1,3) \Gamma(3,2;4) W(1,4) \\
 \Gamma(1,2;3) &= \delta(1,2) \delta(1,3)
 \end{aligned}$$

Figure 2.2: A scheme illustrating the essential steps to perform a complete GW cycle. The process begins with the construction of an initial Green's Function using the initial Kohn-Sham energies ϵ_{KS} and wavefunctions ϕ_{KS} . Quasiparticle energies ϵ_{QP} , as well as the screened Coulomb potential, are obtained once convergence is reached.^[37] Below the figure, the full set of Hedin's Equations are shown.

As explained above, one does not only improve the resulting Green's Function but also other calculated properties. This is especially interesting since the self-energy contains the exchange and correlation energy of the system, similar to the exchange correlations functional in the DFT framework. This means it is also possible to improve the quasiparticle energies by replacing the energy contribution of the exchange-correlation functional with the self-energy as seen below.^[38]

$$\epsilon_i^{GW} = \epsilon_i^{DFT} + \langle \Psi_i^{DFT} | \Sigma(\epsilon_i^{GW}) - V^{xc} | \Psi_i^{DFT} \rangle \quad (2.51)$$

Ideally, this would result in a description of the electronic system that is independent of the initially guessed wavefunction and particularly the initial exchange-correlation functional. Unfortunately, a full self-consistent solution of Hedin's equations comes at a high computational cost. This is why one has to refer once again to approximations. In particular, the eigenvalue-only self-consistent GW (often abbreviated as evGW) is the most commonly employed. In this case, one only improves the quasiparticle energies iteratively until convergence is reached while remaining with the original guess wavefunctions that replaced the Lehman amplitudes. The alternative approach is called single shot GW and is often denoted as G_0W_0 and consists only of a single iteration using the KS energies.^[39]

2.5.3 Contour Deformation Techniques

The high computational cost of solving Hedin's equations will usually force one to make approximations to calculate the self-energy operator. Possible solutions are contour deformation techniques, which have been used excessively during this work. This idea has been introduced in earlier work^[40], which is why only the basic idea is discussed at this point. Technical details about the implementation in Turbomole can be found in the referred literature.^[37]

In general, the self-energy operator can be separated into an exchange and a correlation

part.^[33] This fact is introduced very briefly at this point, however, it will be of greater importance in the following chapter 2.6.1, where the Bethe-Salpeter Equation is derived. The majority of computational effort lies in calculating the correlation part. As discussed in the previous chapter, it is possible to apply the GW approximation to the self-energy operator.

$$\begin{aligned}\Sigma(1, 2) &= iG(1, 2)W(1, 2) \\ &= iG(1, 2)v(1, 2) + iG(1, 2)(W(1, 2) - v(1, 2)) \\ &= \Sigma^X(1, 2) + \Sigma^C(1, 2)\end{aligned}\quad (2.52)$$

By making use of the convolution theorem, one can express the correlation part of the self-energy operator in the spectral domain.^[37]

$$\Sigma^X(x, x', \omega) = \frac{i}{2\pi} \oint d\omega' G(x, x', \omega + \omega') v(x, x') \quad (2.53)$$

$$\Sigma^C(x, x', \omega) = \frac{i}{2\pi} \oint d\omega' G(x, x', \omega + \omega') [W(x, x', \omega') - v(x, x')] \quad (2.54)$$

The exchange part Σ^X will reduce to the Fock Term upon insertion of a basis. This is shown in appendix 5.7. This integral expression can be solved by making use of the residue theorem. To do so the contour integral is split into two parts, which each align with the real and imaginary axis. This separation enables one to neglect the poles of W since they are not located inside the closed path, as can be seen in figure 2.3.^[41]

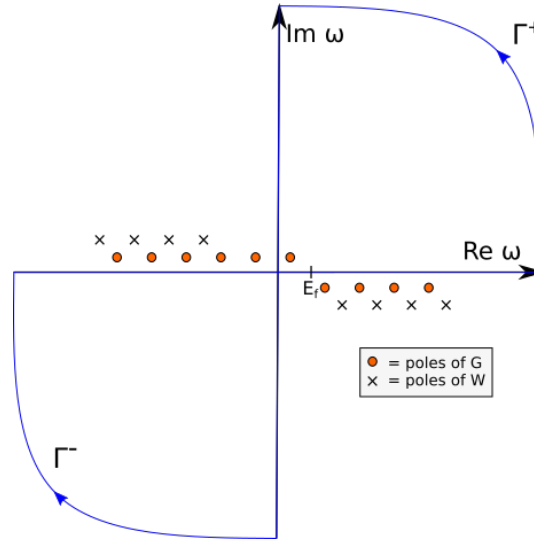


Figure 2.3: The contour paths Γ^\pm are selected such that all significant poles of G are enclosed within the area bounded by Γ^\pm , whereas all poles of W remain outside this area. This way one can make use of the residue theorem to simplify the calculation of the occurring integrals.^[42]

All GW quasiparticle energies are located on the real axis since the η parameter in equation (2.8) is set to zero. This will mean that the integration along the real axis can be skipped, by adding all residues at the location of the quasiparticle energies.^[42]

The main advantage of this method is the reduction in computational effort. This approach scales with $\mathcal{O}(N^4)$, while the spectral method scales with $\mathcal{O}(N^6)$.^[43] Furthermore, it is possible to limit the amount of quasiparticle energies that need to be calculated, whereas the spectral method always has to calculate the full spectrum.

2.6 Bethe Salpeter Equation

So far, we only discussed ways to calculate quasiparticle energies, which correspond to ionization energies and electron affinities. To describe excited states within metal complexes we will need to extend this framework to properly describe transitions within the molecule. To do this, one has to shift their attention to the Bether-Salpeter Equation (BSE).

2.6.1 "Casida-like" Equation

In order to treat transitions within a molecule, one has to investigate the correlated motion of electron-hole pairs. For this, we will roughly follow a derivation shown by Carina Faber.^[35] A particular quantity of interest in this context is the two-particle correlation function L , as we will see that it is connected to the susceptibility χ . The idea is to derive an equation of motion for L , which we can then solve to calculate observables. The two-particle correlation function is defined as

$$L(1, x't; 2, xt^+) = -G_2(1, x't; 2, xt^+) + G_1(1, 2)G_1(x't, xt^+). \quad (2.55)$$

It is possible to observe that also a variational derivative of the Green's Function produces an expression that is similar to the one introduced above. Therefore, the following expression holds^[29]

$$L(1, x't; 2, xt^+) = \frac{\delta G_1(1, 2)}{\delta w(x, x', t)}. \quad (2.56)$$

Its derivation is also shown in the appendix 5.6. With the insertion of equation (2.35) and (2.23) on the right-hand side, one can find a new relation.

$$\begin{aligned} L(1, x't; 2, xt^+) &= - \int d3d4G(1, 3) \left[\frac{\delta G^{-1}(3, 4)}{\delta w(x, x', t)} \right] G(4, 2) \\ &= - \int d3d4G(1, 3) \left[\frac{\delta G_0^{-1}(3, 4)}{\delta w(x, x', t)} - \frac{\delta M(3, 4)}{\delta w(x, x', t)} - \frac{\delta w(3, 4)}{\delta w(x, x', t)} \right] G(4, 2) \end{aligned} \quad (2.57)$$

In this case, we explicitly want to include the Hartree potential, so we replaced the self-energy with the mass operator. The derivative of G_0^{-1} vanishes and one obtains

$$\begin{aligned} L(1, x't; 2, xt^+) &= \int d3d4G(1, 3) \left[\delta(x_3, x)\delta(x_4, x')\delta(t_3 - t_4)\delta(t_3 - t) \right. \\ &\quad \left. + \frac{\delta M(3, 4)}{\delta w(x, x', t)} \right] G(4, 2). \end{aligned} \quad (2.58)$$

Evaluating the integrals by integrating over the delta distributions and applying the chain rule to the second term will result in an equation of motion for the two-particle correlation function, which is called the Bethe-Salpeter Equation (BSE)^[29]

$$\begin{aligned} L(1, x't; 2, xt^+) &= L_0(1, x't; 2, xt^+) + \int d3d4d5d6L_0(1, 4; 2, 3) \frac{\delta M(3, 4)}{\delta G(5, 6)} \frac{\delta G(5, 6)}{\delta w(x, x', t)} \\ &= L_0(1, x't; 2, xt^+) \\ &\quad + \int d3d4d5d6L_0(1, 4; 2, 3)\Theta^{\text{BSE}}(3, 5; 4, 6)L(5, x't; 6, t^+). \end{aligned} \quad (2.59)$$

Here, the non interacting correlation function $L_0(1, 2; 1', 2') = G(1, 2')G(2, 1')$ and the Bethe Salpeter Kernel $\Theta^{\text{BSE}}(3, 5; 4, 6) = \frac{\delta M(3, 4)}{\delta G(5, 6)}$ were defined.

Our goal is to simplify equation (2.59) by making use of the previously discussed GW approximation. Therefore, one separates the self-energy operator in an exchange and a correlation part, in the same way, it has been done in the last chapter⁷

$$M(1, 2) = V(1, 2) + \Sigma^X(1, 2) + \Sigma^C(1, 2). \quad (2.60)$$

The exchange part reduces to the already known Fock term.^[35] Afterwards, one has to find an expression for the Bethe Salpeter Kernel, to simplify it. This can be done by inserting the aforementioned GW approximation and performing the derivative while considering the chain rule.

$$\begin{aligned} \Theta^{\text{BSE}}(3, 5; 4, 6) &= i \frac{\delta G(3, 4)}{\delta G(5, 6)} W(3, 4) + i G(3, 4) \frac{\delta W(3, 4)}{\delta G(5, 6)} + \frac{\delta V(3, 4)}{\delta G(5, 6)} \\ &= \frac{1}{i} [-\delta(3, 6)\delta(4, 5)W(3, 4) + \delta(3, 4)v(3, 6)\delta(5, 6)] \end{aligned} \quad (2.61)$$

In the last step, we assume that the variation of W is small with respect to G so we can neglect the second term. This approach corresponds to neglecting the changes in screening for the excited states.^[37] If one assumes a static approximation for the screened Coulomb interaction, one obtains

$$W(1, 2) = W_{\text{stat}}(x_1, x_2)\delta(t_1 - t_2). \quad (2.62)$$

Inserting this result into equation (2.59) and making use of the convolution theorem, one will be able to express the BSE in Fourier space^[35]

$$L(\omega) = L_0(\omega) + iL_0(\omega)L(\omega) (W(x_3, x_4) - v(x_3, x_4)). \quad (2.63)$$

This step is shown in the appendix 5.9. The non-interacting two-particle correlation function $L_0(\omega)$ is obtained through the same method.

$$L_0(\omega) = \frac{1}{2\pi} \int d\omega' G(\omega + \omega')G(\omega') \quad (2.64)$$

With the goal of evaluating this expression, one can insert the spectral representation from equation (2.8). This yields a set of products, which one can rearrange in the following way

$$\begin{aligned} L_0(x_1, x_2, x'_1, x'_2, \omega) &= \frac{1}{2\pi} \sum_{lm} \int d\omega' \left(\frac{f_l(x_1)f_l^*(x'_2)}{\omega + \omega' - \epsilon_l - i\eta} \right) \left(\frac{f_l(x_2)f_l^*(x'_1)}{\omega' - \epsilon_l - i\eta} \right) \\ &+ \left(\frac{g_m(x_1)g_m^*(x'_2)}{\omega + \omega' - \epsilon_m + i\eta} \right) \left(\frac{f_l(x_2)f_l^*(x'_1)}{\omega' - \epsilon_l - i\eta} \right) \\ &+ \left(\frac{f_l(x_1)f_l^*(x'_2)}{\omega + \omega' - \epsilon_l - i\eta} \right) \left(\frac{g_m(x_2)g_m^*(x'_1)}{\omega' - \epsilon_m + i\eta} \right) \\ &+ \left(\frac{g_m(x_1)g_m^*(x'_2)}{\omega + \omega' - \epsilon_m + i\eta} \right) \left(\frac{g_m(x_2)g_m^*(x'_1)}{\omega' - \epsilon_m + i\eta} \right) \\ &= \frac{1}{2\pi} \sum_{lm} \sum_{i=1}^4 \int d\omega' I_i(\omega, \omega'). \end{aligned} \quad (2.65)$$

with $\epsilon_l = E_0^N - E_l^{N-1}$ and $\epsilon_m = E_m^{N+1} - E_0^N$, which are the quasiparticle energies obtained from a preceding GW calculation. The l index sums over all occupied states, while m sums over all unoccupied states.

It is clear, that the contribution to the integral results from each product $I_i(\omega, \omega')$ individually.

⁷ $V(1, 2) = V(1)\delta(1, 2)$

However, it is also clear that one can make use of the residue theorem at this point since each product has a set of poles in the complex plane.

The position of each term in the complex plane is determined by the sign in front of $i\eta$, which means one can neglect the terms I_1 and I_4 , by choosing to integrate only along the upper half of the complex plane.^{[35]⁸} The calculation of each residue is therefore not difficult and can be done analytically the following way for $I_2(\omega, \omega')$

$$\begin{aligned} \text{Res}(I_2, \omega_i) &= \left[(\omega' - \epsilon_l - i\eta) \frac{g_m(x_1)g_m^*(x'_2)}{\omega + \omega' - \epsilon_m + i\eta} \frac{f_l(x_2)f_l^*(x'_1)}{\omega' - \epsilon_l - i\eta} \right]_{\omega'=\epsilon_l+i\eta} \\ &= \frac{g_m(x_1)g_m^*(x'_2)f_l(x_2)f_l^*(x'_1)}{\omega + \epsilon_l - \epsilon_m + 2i\eta}. \end{aligned} \quad (2.66)$$

One neglects the factor of 2 in front of η , since the term is infinitesimal, which yields an expression for L_0

$$\begin{aligned} L_0(x_1, x_2, x'_1, x'_2, \omega) &= 2\pi i \frac{1}{2\pi} \sum_{m,l} \sum_i \text{Res}(I_i) \\ &= i \sum_{m,l} \frac{g_m(x_1)g_m^*(x'_2)f_l(x_2)f_l^*(x'_1)}{\omega + (\epsilon_l - \epsilon_m) + i\eta} - \frac{f_l(x_1)f_l^*(x'_2)g_m(x_2)g_m^*(x'_1)}{\omega + (\epsilon_m - \epsilon_l) - i\eta}. \end{aligned} \quad (2.67)$$

To perform calculations one chooses an orthonormal basis to represent the BSE.

$$L^{n_1, n_2, n_3, n_4} = \iiint dx_1 dx'_1 dx_2 dx'_2 \phi_{n_1}(x'_1) \phi_{n_2}^*(x_1) L(x_1, x'_1, x_2, x'_2) \phi_{n_3}^*(x_2) \phi_{n_4}(x'_2) \quad (2.68)$$

This will result in a tensor equation, which needs to be solved.

$$\overline{\overline{L}}(\omega) = \overline{\overline{L_0}}(\omega) + \overline{\overline{L_0}}(\omega) \cdot \overline{\overline{\Theta}} \cdot \overline{\overline{L}}(\omega) \quad (2.69)$$

To specify the matrices we first insert the expression (2.67) into equation (2.59). This way the integrals can be solved to obtain the matrix elements. Fortunately, most matrix elements will be equal to 0, since one has chosen an orthonormal basis set. The remaining terms are those where $n_1 = n_3$ and $n_2 = n_4$, which means that one has to solve a matrix equation over the two remaining independent parameters. We define $\Delta\epsilon_{n_2, n_1} = \epsilon_{n_2} - \epsilon_{n_1}$ and set $\eta = 0$.

$$\overline{\overline{L_0}} = i \begin{bmatrix} 0 & 0 & 0 & 0 \\ 0 & 0 & 0 & 0 \\ 0 & 0 & \frac{-1}{\Delta\epsilon_{n_2, n_1} - \omega} & 0 \\ 0 & 0 & 0 & \frac{1}{\Delta\epsilon_{n_2, n_1} - \omega} \end{bmatrix} \quad (2.70)$$

One can see that both non-vanishing matrix elements are structurally similar, which motivates the definition of the occupation factor

$$f_i = \begin{cases} 1 & \text{if } i = m \\ 0 & \text{if } i = l \end{cases}. \quad (2.71)$$

With this, one can separate the matrix into a term that covers the energy and an occupation matrix $\overline{\overline{F}}$

$$-iL_0^{n_1, n_2}(\omega) = \frac{(f_{n_2} - f_{n_1}) \delta(n_1, n_3) \delta(n_2, n_4)}{\Delta\epsilon_{n_2, n_1} - \omega} \quad (2.72)$$

⁸The same result is obtained if we chose to integrate along the lower half plane

$$\begin{aligned}\overline{\overline{L}}_0 &= \overline{\overline{L}}'_0 \cdot \overline{\overline{F}} \\ &= \begin{bmatrix} \frac{1}{\Delta\epsilon_{n_2, n_1} - \omega} & 0 \\ 0 & \frac{1}{\Delta\epsilon_{n_2, n_1} - \omega} \end{bmatrix} \cdot \begin{bmatrix} f_{n_2} - f_{n_1} & 0 \\ 0 & f_{n_2} - f_{n_1} \end{bmatrix}.\end{aligned}\quad (2.73)$$

This result can be inserted into equation (2.69). The final form of the BSE is obtained by solving equation (2.69) for $-i\overline{\overline{L}}(\omega)$.

$$-i\overline{\overline{L}}(\omega) = \left[\left[-i\overline{\overline{L}}'_0 \right]^{-1}(\omega) - i\overline{\overline{F}} \cdot \overline{\overline{\Theta}} \right]^{-1} \overline{\overline{F}} \quad (2.74)$$

Here one can create a connection to regular linear response theory by introducing the susceptibility. The susceptibility matrix is equal to the left-hand side of the equation above^[44]

$$\overline{\overline{\chi}}(\omega) = -i\overline{\overline{L}}(\omega). \quad (2.75)$$

The result is now that one has derived a way to calculate the susceptibility by solving the BSE.

$$\overline{\overline{\chi}}(\omega) = \frac{\overline{\overline{F}}}{\overline{\overline{H}}_{2p} - \omega \cdot \overline{\overline{1}}} \quad (2.76)$$

with the two-particle Hamiltonian H_{2p} ^[35]

$$\overline{\overline{H}}_{2p} = \begin{bmatrix} \Delta\epsilon_{n_2, n_1} & 0 \\ 0 & \Delta\epsilon_{n_2, n_1} \end{bmatrix} + i \begin{bmatrix} \Theta_{ml, m'l'} & \Theta_{ml, l'm'} \\ -\Theta_{lm, m'l'} & -\Theta_{lm, l'm'} \end{bmatrix}. \quad (2.77)$$

The additional matrix elements result from the evaluation of the Bethe Salpeter Kernel. However, as shown in equation (2.63), one can make use of the GW approximation to reduce this term to the difference of the screened and full Coulomb potential. This way it is also possible to express the resonant (diagonal) terms in an orthonormal basis

$$\begin{aligned}H_{ml, m'l'}^{\text{res}} &= \Delta\epsilon_{lm} \delta_{mm'} \delta_{ll'} + \int dx_1 dx_2 \phi_m(x_1) \phi_l^*(x_1) \phi_{m'}(x_2) \phi_{l'}^*(x_2) v(x_1, x_2) \\ &\quad - \int dx_1 dx_2 \phi_m(x_1) \phi_l^*(x_2) \phi_{m'}^*(x_1) \phi_{l'}(x_2) W_{\text{stat}}(x_1, x_2) \\ &= H_{ml, m'l'}^{\text{diag}} + H_{ml, m'l'}^{\text{exch}} + H_{ml, m'l'}^{\text{scr}}.\end{aligned}\quad (2.78)$$

This equation is often referred to as a "Casida-like" equation, due to its similarity to the Casida equation from time-dependent DFT (TD-DFT). The eigenvectors of this matrix are also called response vectors with their respective eigenvalues corresponding to transition energies. This can be seen by the fact that transitions and consequently the absorption spectrum are linked to the imaginary part of the susceptibility.^[45] Equation (2.76) bridges the connection by linking the poles of the susceptibility to the eigenvalue problem of equation (2.77).

2.6.2 Tamm Dancoff Approximation and Correlation Augmented BSE

The most common way of writing down the Bethe-Salpeter Equation is in the following way, which emphasizes the structural similarities to the Casida equation^[46]

$$\begin{bmatrix} A & B \\ -B & -A \end{bmatrix} \begin{bmatrix} X \\ Y \end{bmatrix} = \omega \begin{bmatrix} X \\ Y \end{bmatrix}. \quad (2.79)$$

$A_{ii',aa'}$ and $B_{ii',aa'}$ correspond to the matrix elements (2.77) derived in the last chapter. As in the later implementation, a basis of molecular orbitals is chosen, where i is the index of the occupied and a of the virtual orbitals. X_{ia}^P and Y_{ia}^P are called the response vectors of the system for a particular transition P with a specific vertical transition energy ω_P . At this point, it is also possible to formulate an electron-hole wavefunction in the following manner^[47]

$$\psi_P^{\text{eh}}(x_e, x_h) = \sum_{ia} X_{ia}^P \phi_i(x_h) \phi_a(x_e) + Y_{ia}^P \phi_i(x_e) \phi_a(x_h). \quad (2.80)$$

This expression can be used to calculate other observables such as oscillator strengths^[48] or, as we will see in chapter 2.8, spin-orbit coupling matrix elements by using the linear or quadratic response of the transition density matrix, which we obtain through equation (2.80). The latter can also be used to identify charge transfer characters.^[49] In the following, we always used the length gauge to calculate oscillator strengths. It is known, that different gauges do not coincide with each other, due to the BSE not following the sum rule.^[50] We opted for it because it provided better alignment with experimental values.

The most direct approximation that one can perform at this stage is neglecting the contribution from $B_{ii',aa'}$ by setting it to 0. This leads to the Tamm-Dancoff-Approximation, a well-established method within the field of TD-DFT, which is known for potentially enhancing the accuracy of triplet state descriptions.^[51] It is expected that GW-BSE follows a similar behavior as TD-DFT^[52], which is why this approximation will become a valuable asset when investigating the possibilities of dynamics simulations in chapter 3.6. The physical interpretation is that we primarily focus on the creation of electron-hole pairs, which is the dominant contribution while neglecting higher-order couplings that involve simultaneous excitation and de-excitation processes.

A possible improvement to the "Casida-like" equation is called the correlated augmented BSE.^[53] It is abbreviated to cBSE and attempts to combine TD-DFT and the BSE. Due to the structural similarities, this is accomplished with the straightforward inclusion of additional correlation in the form of the correlation part of the exchange-correlation potential. It can be added to the matrix elements $A_{ii',aa'}$ and $B_{ii',aa'}$ before solving equation (2.79).

2.6.3 Transition Density Matrices

As mentioned in the introduction, it is of crucial importance to distinguish between the different types of possible transitions in the analysis. The character can be obtained by performing an analysis of the one-particle transition density matrix. It is defined in the following way in coordinate space.^[54]

$$\gamma_1^{P,Q}(x, x') = N \int dx_2 \dots dx_n \Psi^P(x, x_2, \dots, x_n) \Psi^Q(x', x_2, \dots, x_n) \quad (2.81)$$

In this case, N is the particle number, and P, Q are indices for different electronic states. It has already been rigorously studied and it is possible to show that, given a complete one-electron basis set $\phi_j(x)$, each entry of the one particle transition density matrix takes the following form^[55]

$$\gamma^{P,Q}(x, x') = \sum_{ia} D_{ia}^{P,Q} \phi_i(x) \phi_a(x') \quad (2.82)$$

along with

$$D_{ia}^{P,Q} = \langle \Psi^P | \hat{a}_i^\dagger \hat{a}_a | \Psi^Q \rangle. \quad (2.83)$$

This occurs because the occupied-to-occupied and virtual-to-virtual blocks are zero, while the mixed blocks contain finite entries. A more detailed argument for this can be found in the appendix 5.8. In general, equation (2.82) yields an expression that is similar to the electron-hole wavefunction we derived in equation (2.80). Especially if the Tamm-Dancoff Approximation is used, one can observe that each entry of the one-particle transition density matrix can be obtained by evaluating the response vector X_{ia} . This will also be of great significance, as it is well-established in wavefunction methods that if the ground state is represented by a single determinant, then the one-particle transition density matrix corresponds to the configuration interaction (CI) vector.^[49] Therefore, this will be the method of choice to approximate the configuration interaction vector for GW-BSE in chapter 2.7. In addition to that, the one-particle transition density matrix can also be used to calculate charge transfer numbers. In general, one can define a charge transfer number if one separates the molecular system into at least two fragments A and B. In such a case the charge transfer number is defined as follows^[56]

$$\Omega_{AB}^Q = \frac{1}{2} \sum_{a \in A, b \in B} \left(D_{ab}^{0Q, [LO]} \right)^2. \quad (2.84)$$

LO stands for the usage of a basis set that is localized on one fragment. To perform calculations, one has to find an expression for Ω_{AB}^Q based on an atomic orbital or molecular orbital basis set. In the case of this work, only a Löwdin-style formula was used^[57]

$$\Omega_{AB}^Q = \sum_{\mu \in A} \sum_{\nu \in B} \left(\overline{S}^{\frac{1}{2}} \overline{D}^{0Q} \overline{S}^{\frac{1}{2}} \right)_{\mu\nu}^2. \quad (2.85)$$

μ and ν refer to an expression in an atomic orbital basis set, which was obtained by transforming the X_{ia} response vector from a molecular orbital into an atomic orbital basis. $S_{\mu\nu}$ is the overlap matrix between different atomic orbitals. Finally, the charge transfer character can be calculated by summing over the off-diagonal elements^[56]

$$CT = \frac{\sum_{A, B \neq A} \Omega_{AB}^Q}{\sum_{A, B} \Omega_{AB}^Q}. \quad (2.86)$$

Further information, as well as technical details, can be found in the literature. [57]

2.7 Linear Vibronic Coupling Model

In the chapter 3.6, we will investigate an approach to perform molecular dynamics simulations by making use of a linear vibronic coupling model. The central quantity of any molecular dynamics simulation is the potential energy surface $\hat{U}_i(R)$. It arises naturally based on the Born-Oppenheimer approximation since it acts as an effective potential for the nuclei. [58] The molecular wavefunction $\Psi_a(r, R)$ reads

$$\Psi_a(r, R) = \sum_i \chi_{ia}(R) \phi_i(r, R). \quad (2.87)$$

Here $\chi_{ia}(R)$ describes the nuclear wavefunction, as it depends only on the nuclear coordinates R . $\phi_i(r, R)$ is the adiabatic electronic wavefunction, that depends not only parametrically on all nuclear coordinates R , but also on the electronic coordinates r . The product of the two yields the Born-Oppenheimer wavefunction ψ^{BOA} .

There are two major ways to express the molecular Hamiltonian of the entire system. The adiabatic Hamiltonian is obtained by choosing the eigenfunctions of the electronic Hamiltonian as a basis set. In such a case the molecular Hamiltonian reads. [59]

$$\hat{H}_{\text{mol}}^{\text{adiabatic}} = \sum_{ij} \left(\delta_{ij} \hat{H}_i + (1 - \delta_{ij}) \hat{\Theta}_{ij} \right) |\phi_i\rangle \langle \phi_j| \quad (2.88)$$

\hat{H}_i is the sum of the kinetic energy of the nuclei \hat{T}_{nuc} and the potential energy surface $\hat{U}_i(R)$, while $\hat{\Theta}_{ij}$ is called the nonadiabatic coupling operator which accounts for the coupling between different states as a result of nuclear motion and reads.

$$\hat{\Theta}_{ij} = \langle \phi_i | \hat{T}_{\text{nuc}} | \phi_j \rangle - \sum_n \frac{1}{m_n} \langle \phi_i | \nabla_n | \phi_j \rangle \nabla_n \quad (2.89)$$

In the Born-Oppenheimer the kinetic energy of the nuclei is 0. The separation of nuclear and electronic degrees of freedom, as in equation (2.87) will consequently hold, if the entries of $\hat{\Theta}_{ij}$ are small and can be neglected. However, if the coupling between two states becomes important, the Born-Oppenheimer Approximation breaks down, its entries become large, and non-radiative transitions become possible, such as internal conversion (IC). Additionally, intersystem crossing (ISC) may occur as a second type of non-radiative transition due to spin-orbit coupling. This will be the topic of chapter 2.8.

An alternative approach would be to change the electronic Hamiltonian, by removing the dependence on the nuclear coordinate and instead choose only a fixed position R_0 . This has the immediate effect that $\hat{\Theta}_{ij}$ vanishes since the electronic wavefunctions do not depend on the nuclear coordinate anymore. Instead, the electronic Hamiltonian will no longer be diagonal, since the chosen basis functions are not eigenfunctions, except at R_0 . [59] Instead the coupling between different states will now be encoded in an additional interaction term $\hat{V}(R, R_0)$.

$$\hat{H}_{\text{elec}}(R) = \hat{H}_0(R_0) + \underbrace{\hat{H}_{\text{elec}}(R) - \hat{H}_0(R_0)}_{\hat{V}(R, R_0)} \quad (2.90)$$

This will lead to a new molecular Hamiltonian in the diabatic representation.^[60]

$$\hat{H}_{\text{mol}}^{\text{diabatic}} = \sum_{ij} \left(\delta_{ij} \hat{H}_i + (1 - \delta_{ij}) \hat{V}_{ij} \right) |\phi_i\rangle \langle \phi_j| \quad (2.91)$$

Since both basis sets are complete, both representations will yield the same observables. Furthermore, the diagonal elements will coincide except at the possible crossing points between two potential energy surfaces. Here the two diabatic surfaces will intersect, whereas the adiabatic surfaces experience avoided crossing with a gap of two times the coupling between the states.^[61] A common example is sodium chloride which is depicted below in figure 2.4.

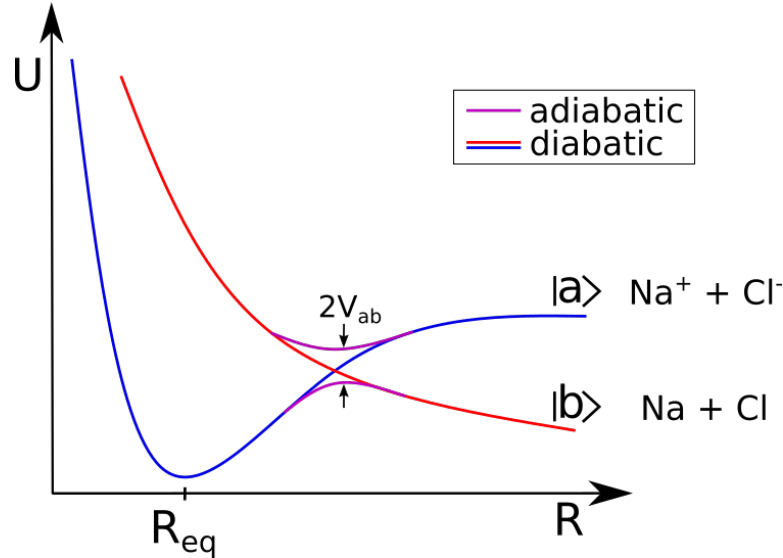


Figure 2.4: Potential energy surfaces of NaCl for the ground- and lowest excited state. Both adiabatic and diabatic representations of the potential energy surface are drawn. Both representations overlap, except at the crossing point, where the adiabatic surfaces experience avoided crossing.^[62]

In order to perform dynamics simulations, one has to find a good approximation to the potential energy surface. To do so, we make use of a linear vibronic coupling model, which has already been discussed in detail in the literature.^[63] Here one approximates the coupling matrix \bar{V} in the diabatic representation in the following way

$$\bar{V} = V_0 \bar{1} + \bar{W}. \quad (2.92)$$

To express the individual terms, one introduces a set of normal coordinates q_i , which lead to the following expressions

$$V_0 = \sum_i \frac{\omega_i}{2} q_i^2 \quad (2.93)$$

and

$$W_{\alpha\alpha} = \epsilon_\alpha + \sum_i \underbrace{\frac{\partial \bar{V}_{\alpha\alpha}}{\partial q_i}}_{\kappa_i^\alpha} q_i \quad (2.94)$$

$$W_{\alpha\beta} = \xi_{\alpha\beta} + \sum_i \underbrace{\frac{\partial \bar{V}_{\alpha\beta}}{\partial q_i}}_{\lambda_i^{\alpha\beta}} q_i, \alpha \neq \beta.$$

The expression in equation (2.93) refers to a harmonic approximation to the potential energy surface around the equilibrium position R_{eq} . ω_i are the frequencies to the corresponding normal mode. ϵ_α refers to the vertical transition energy, calculated on the GW-BSE level of theory, and $\xi_{\alpha\beta}$ are spin-orbit coupling parameters, which were calculated using the PROPER module, whose functionalities were extended by Christof Holzer as part of a collaboration. The two parameters κ_i^α and $\lambda_i^{\alpha,\beta}$ are intra- and interstate coupling constants, which have to be determined numerically with the use of wavefunction overlaps between states at geometries with different displacements $\pm\delta Q_i$.^[64]

$$\kappa_i^\alpha = \frac{1}{2\delta Q_i} \left[\left(\overline{\overline{S}}(Q_i + \delta Q_i) \overline{\overline{H}}(Q_i + \delta Q_i) \overline{\overline{S}}^T(Q_i + \delta Q_i) \right)_{\alpha\alpha} - \left(\overline{\overline{S}}(Q_i - \delta Q_i) \overline{\overline{H}}(Q_i - \delta Q_i) \overline{\overline{S}}^T(Q_i - \delta Q_i) \right)_{\alpha\alpha} \right] \quad (2.95)$$

$$\lambda_i^{\alpha\beta} = \frac{1}{2\delta Q_i} \left[\left(\overline{\overline{S}}(Q_i + \delta Q_i) \overline{\overline{H}}(Q_i + \delta Q_i) \overline{\overline{S}}^T(Q_i + \delta Q_i) \right)_{\alpha\beta} - \left(\overline{\overline{S}}(Q_i - \delta Q_i) \overline{\overline{H}}(Q_i - \delta Q_i) \overline{\overline{S}}^T(Q_i - \delta Q_i) \right)_{\alpha\beta} \right] \quad (2.96)$$

$S_{\alpha\beta}$ is the overlap matrix between two molecular wavefunctions at different displacements. The theory behind its complete calculation is outside the scope of this work, which is why additional information regarding it can be found in the literature.^[65]

2.8 Spin-Orbit Coupling

In order to accurately perform dynamics simulations involving states of different multiplicities, we will have to include spin-orbit coupling (SOC) effects in our model. Without them, transitions between states of different multiplicity cannot be taken into account, which is a phenomenon that will occur in transition metal complexes. There exist two possible solutions to include SOC in our model. In the first approach, one has the opportunity to describe molecular orbitals as spinors.^[66] This method offers the advantage of directly including SOC effects since a relativistic description of quantum mechanics is used. However, this method will come with additional computational effort and the problem of correctly assigning states due to the higher number of possible transitions. Furthermore, unphysical states may occur due to numerical instabilities, which makes this framework unsuitable for dynamics simulations. We thus investigated the option to calculate SOC matrix elements directly in linear or quadratic response.

In general, expectation values $f(t)$ of observables \hat{O} may be expressed using the state-to-state transition density matrix, with a certain coupling strength λ to an external field.^[67]

$$f_\lambda(t) = \langle \hat{O}(t) \rangle = \text{Tr} \left[\hat{O}(t) \gamma_\lambda(t) \right] \quad (2.97)$$

This suggests an expansion of the transition density matrix γ into a power series, based upon the coupling strength λ . The expansion up to the quadratic response leads to the following expression^{[67] [68]}

$$\gamma^{nm} = \begin{pmatrix} K_{ij}^{PQ} & X_{ia}^{PQ} \\ (Y_{ai}^{PQ})^\dagger & K_{ab}^{PQ} \end{pmatrix}. \quad (2.98)$$

Here we make use of the response vectors introduced in chapter 2.6.2 as the solution of the Bethe-Salpeter equation. The indices a, b refer to occupied and i, j to virtual orbitals and P, Q to different electronic states. The diagonal elements are defined as follows^[68]

$$K_{ij}^{PQ} = - \sum_a X_{ai}^P Y_{aj}^Q + X_{ai}^Q Y_{aj}^P \quad (2.99)$$

$$K_{ab}^{PQ} = \sum_i X_{ai}^P Y_{bi}^Q + X_{ai}^Q Y_{bi}^P. \quad (2.100)$$

In the case of linear response, this step is shown in the appendix 5.8. This can be expanded for higher orders to obtain equation (2.98). With this, one can calculate the right-hand side of equation (2.97) in quadratic response, if one utilizes the one-electron part of the Breit-Pauli operator to account for SOC.^[69]

$$\begin{aligned} \hat{H}_{\text{SOC}} &= \frac{1}{2c^2} \sum_i^{N_{el}} \sum_{\alpha}^{N_{nuc}} Z_{eff}(\alpha) \left(\frac{\hat{r}_{i\alpha}}{r_{i\alpha}^3} \times \hat{p}_i \right) \cdot \hat{s}_i \\ &= \sum_i^{N_{el}} \zeta(r_i) \hat{l}_i \cdot \hat{s}_i \end{aligned} \quad (2.101)$$

with

$$\zeta(r_i) = \frac{1}{2c^2} \sum_{\alpha}^{N_{nuc}} \frac{Z_{eff}(\alpha)}{r_{i\alpha}^3} \quad (2.102)$$

For this, an effective nuclear charge has been introduced that is obtained from the literature.^[70] This Hamiltonian will take the place of the aforementioned external field and consequently lead to the following expression for SOC matrix elements between singlet and triplet states if a molecular orbital basis is chosen to transform the SOC Hamiltonian.

$$\xi_{PQ}^d = \langle S_Q | \hat{H}_{\text{SOC}} | T_P \rangle = \sum_{ij} K_{ij}^{PQ} H_{ij}^{d,\text{SOC}} + \sum_{ab} K_{ab}^{PQ} H_{ab}^{d,\text{SOC}}, \quad d = \{x, y, z\} \quad (2.103)$$

These expressions hold for all states but the ground state, which is why the linear response was chosen for this case.

$$\langle S_0 | \hat{H}_{\text{SOC}} | T_P \rangle = \sum_{ai} (X - Y)_{ai}^P H_{ai}^{d,\text{SOC}}. \quad (2.104)$$

2.9 Computational Details and LVCM Implementation

All quantum chemical calculations were performed on the latest Turbomole versions 7.8 and 7.8.1.^{[71] [72]} In particular, the GW-BSE calculations were performed in the ESCF module^[66] with preceding self-consistent field calculations from the DSCF^[73] or RIDFT^[74] modules. Normal modes and their corresponding frequencies were obtained by the AOFORCE module.^[75] In some cases we included solvation effects through an additional dielectric continuum model. This was done through the COSMO module of Turbomole.^[76]

Equilibrium geometries were obtained using either literature values, through the above-mentioned DFT- or Turbomoles RI-MP2 module.^[77] In some cases results were compared to their corresponding Coupled Clustered counterparts which were obtained in the RICC2 modules.^{[78] [79] [80]}

The analysis of the transition density matrices was performed in a slightly modified version of the Theodore program package, to make them compatible with the preceding open shell GW-BSE calculations.^[57]

All calculations regarding the LVC model were carried out in a modified version of the SHARC program package.^{[81][82]} To do so, a new interface between SHARC and the ESCF/PROPER module from Turbomole was developed, through this work. It enables one to carry out a full LVC parametrization of the potential energy surfaces using the GW-BSE level of theory. Furthermore, it includes a new scheme derived and implemented into the latest version of Turbomole by Christof Holzer to compute SOC matrix elements as explained in the previous chapter. This last aspect was part of a cooperation between him, Sebastian Mai, and this work.

3 Electronic Structure Analysis of different Systems

With a theoretical framework set up, we are now in a position to perform calculations. In particular, we will initially focus on a smaller dimer system, where it is possible to investigate charge transfer transitions, alongside their long-range behavior. As mentioned in the introduction, inside transition metal complexes, we will find a mixture of charge transfer and metal-centered states, so all types of transition will become important at once when we want to cover these larger systems. In particular, we must investigate whether the GW-BSE framework yields possible solutions to problems occurring when treating transition metal complexes in the DFT framework. One has to pay special attention to distinguish between all the possible types of transitions particularly charge transfer transitions which pose a problem in regular density functional theory calculations. We will then continue with a short investigation of the computational cost, before as well examining the accuracy of metal-centered states. In the end, the possibility of including spin-orbit coupling effects will be tested to pave the way for possible dynamics simulations using the GW-BSE framework.

3.1 Long-Range Behavior of Charge-Transfer-States

A common limitation within the DFT framework is the incorrect description of charge transfer states for common exchange-correlation functionals. Many example studies exist where DFT fails to accurately describe the long-range behavior of inter- or intramolecular charge transfer transitions.^{[83] [84]} This happens, because most matrix elements of the Casida equation in TD-DFT vanish for a long range so that only the difference between the involved molecular orbitals persists.^[85]

To show that the GW-BSE framework does not suffer from similar problems, we investigated a small system consisting of an ethene-tetrafluoroethylene dimer, which is a textbook example of a system that exhibits strong charge transfer transitions.^[86] In detail, we performed a set of single-point calculations for different intermolecular distances, as shown in figure 3.1.

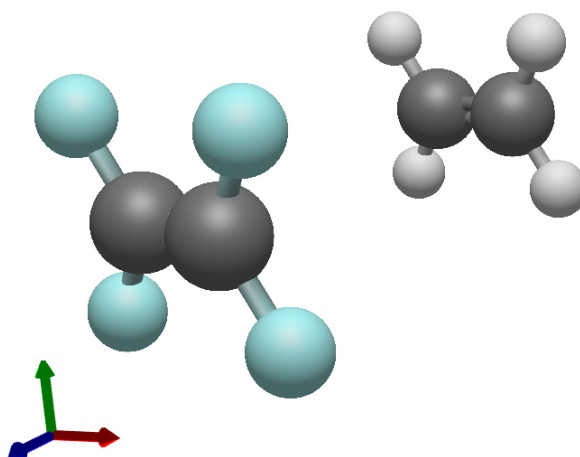


Figure 3.1: Geometry of the ethene-tetrafluoroethylene dimer. The spacing between the two molecules along the Z-axis (blue) was gradually increased from 4.1 Å to 10 Å. At each point, single-point calculations for different levels of theory were performed. Finally, the transition density matrix was analyzed to follow the energy of the lowest charge transfer state.

At each point, the transition density matrix was analyzed to track the energy of the first charge transfer state with the lowest vertical transition energy. We expect to observe an increase in the energy that follows the Coulomb potential like $\frac{1}{r}$ for long distances, where r is the center of mass distance.^[86] For all calculations we used a def2-TZVP basis set. The results for different levels of theory are shown below in figure 3.2.

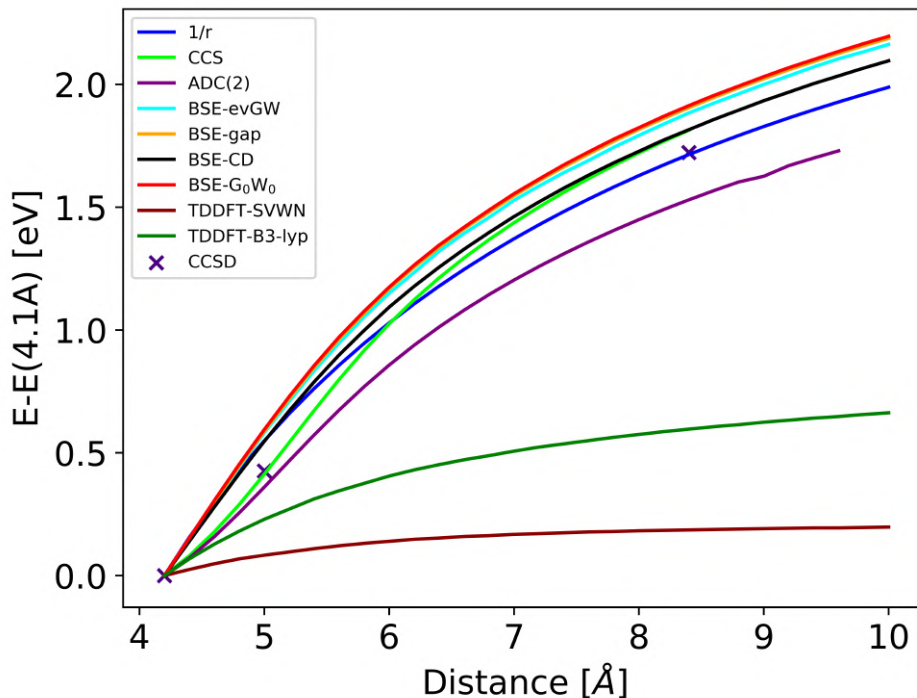


Figure 3.2: Long-range behavior of the vertical transition energy of the system shown in figure 3.1. Each color indicates the behavior for a different level of theory. Time-dependent density functional theory calculations are denoted as TDDFT followed by the employed functional. CCS and ADC refer to the coupled cluster methods CC Singles and algebraic diagrammatic construction at second-order. Calculations done in the GW-BSE framework are shown as BSE. Contour denotes the application of contour deformation techniques, while gap indicates that the correlation component of the self-energy was exclusively computed for the HOMO and the LUMO. Single-shot G_0W_0 calculations were consistently performed, except for BSE-evGW. All transition energies are normalized to their respective energies at 4.1 Å

As shown above in figure 3.2, the DFT framework cannot properly predict the long-range behavior. The description is especially poor for simple exchange-correlation functionals that rely on local density approximation, such as SVWN. Here, it is observed that the curve transitions rapidly into a region where it remains constant. This behavior is independent of the chosen exchange-correlation functional, as demonstrated by the failure of the B3-LYP functional. A typical solution to this problem offer wavefunction-based methods, such as coupled cluster methods. Even cheaper methods, such as coupled cluster singles produce already an acceptable result, which is only improved by more expensive calculations, such as coupled clusters with singles and doubles. In the case of GW-BSE, we observe that it can reproduce the correct behavior, independent of the employed theory. It appears that it does not play a significant role whether self-consistency is taken into account or not. The contour deformation technique also produces the correct result, no matter if the correlation part of the self-energy operator was calculated for the entire quasiparticle spectrum or only the HOMO-LUMO gap. This investigation demonstrates that, besides all the structural similarities between GW-BSE and TD-DFT, there are more significant differences between the two theories that lead to GW-BSE

describing the system more accurately than DFT. This phenomenon is also not unique to this type of system, as it has already been observed in related work.^[87] Nevertheless, this better description comes at a computational cost, which will be discussed in the next chapter.

3.2 Assessment of Computational Cost

We saw in the initial investigation above that GW-BSE yields an improvement to the description of charge transfer states. We made a rough estimation of the additional computational cost by comparing the wall-time of the investigated system from chapter 3.1. More rigorous investigations of the true computational cost involving many systems can be found in the literature.^[88] This is why the following results are only an estimation for calculations on our local infrastructure for small systems. All calculations were performed on an Intel(R) Xeon(R) CPU E5-2660 v2 2.20GHz in parallel via OpenMP over all 20 threads. The results are showcased in the following figure 3.3.

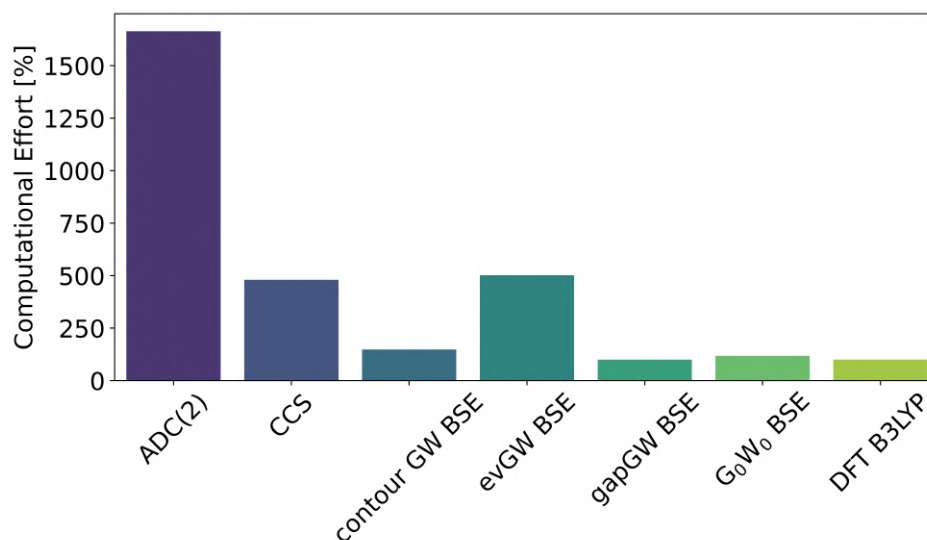


Figure 3.3: Total wall time for a single point calculation for the dimer in chapter 3.1. All calculations are normalized to the DFT calculations performed using the B3LYP functional, which is set to 100%. The calculation at the CCSD level is excluded due to its significantly higher cost, reaching 97000%. It is possible to observe the similarities in the computational cost of G₀W₀-BSE and TD-DFT calculations. Self-consistency increases the computational cost by approximately 5 times. However, all GW-BSE calculations are either less expensive or comparable in cost to the tested coupled cluster methods.

It is clear from the figure above that the computational cost of all GW-BSE methods is comparable to other common electronic structure methods. Particularly, the single-shot G₀W₀-BSE methods show a similar computational cost to the TD-DFT methods. Especially the BSE part has almost the same cost, due to the structural similarities between the Bethe-Salpeter and Casida equation. The limiting factor is however the preceding GW calculation. Its calculation in a self-consistent scheme requires 12 times more computational time compared to the single-shot variation, as 12 quasiparticle iterations were necessary to achieve convergence. For other larger systems, we will later observe in chapter 3.4 that a minimum of 6 iterations is usually required. Nonetheless, it seems that achieving self-consistency results in a total cost comparable to that of cheaper coupled cluster methods. For a system of this size, the computational cost is significantly lower than that of ADC(2) or CCSD.

3.3 The Accuracy of MC-States for Systems with Triazacyclononane Ligands

As we have seen in the previous chapter, the GW-BSE framework is capable of accurately describing the long-range behavior of charge transfer states, whereas DFT fails at the same task. Now, we would like to investigate transitions with significant MC characters. As discussed in the introduction, they play an important role in the dynamics that occur after the absorption of light. Usually, they occur in way that they are strongly mixed with other MLCT states. Metal complexes involving triazacyclononane ligands in contrast exhibit almost pure low-lying d-d transitions, which is why we will investigate them in greater detail in this chapter.^[89] We will pair them with different central metals, allowing us to control the spin state of the entire molecular system, as it is determined by the oxidation state of the central metal. This means that we will have the opportunity to investigate the capabilities of this framework for open- and closed-shell systems. This fact is illustrated in figure 3.4, which shows all investigated central atoms, alongside their electronic configuration.











Cr(III) HS	Fe(II) LS	Co(III) LS	Ni(II) LS	Co(II) HS
d^3 e_g 	d^6 e_g 	d^6 e_g 	d^7 e_g 	d^7 e_g 
 t_{2g}	 t_{2g}	 t_{2g}	 t_{2g}	 t_{2g}

Figure 3.4: Electronic configurations of the d orbitals of the investigated central metals. High-spin systems are denoted as HS, whereas LS refers to low-spin. The energetically higher d orbitals are denoted as e_g according to their irreducible representation in the O_h point group. The energetically lower orbitals are denoted as t_{2g} .

This complex also has the advantage that it usually exhibits isolated MC transitions in the visible range for some central metals, such that no MLCT transitions appears at similar energies. Furthermore, they are an ideal system since they have been subject to a lot of studies, which means that experimental data is readily available.^[90] Not only spectra but also crystal structures can be obtained for comparison.^{[89] [91]} The structure of the system is depicted in figure 3.5.

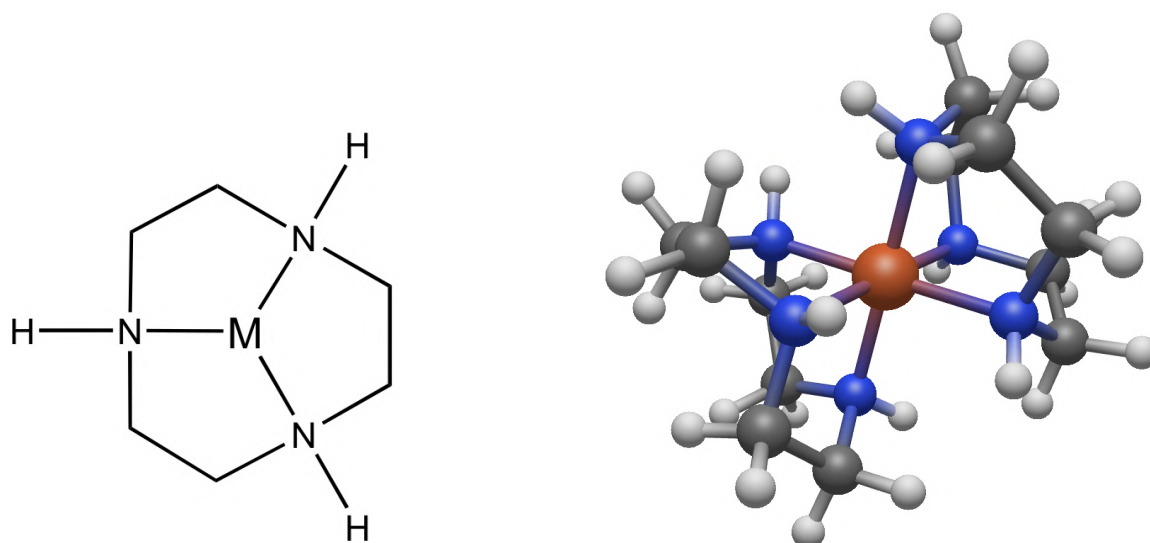


Figure 3.5: Structure of one triazacyclononane ligand together with its 3D equilibrium geometry. We will modify the central metal and/or its oxidation state to investigate the effect on MC transitions.

An important factor will be the exact geometry of the system, in particular for different spin states. It is known, that DFT has problems in predicting the accurate spin-state, equilibrium geometry, and spectrum unless specialized functionals are employed.^[92] We initially made use of geometries derived from the DFT or given in the literature.^[92] However, as this resulted in unsatisfactory results, we referred to geometries derived from Møller–Plesset second-order perturbation theory (MP2) level geometry optimizations. MP2 was chosen because it comes at an acceptable computational cost and yields results that are closer to experimental values when compared to DFT. Additionally, it is a method that has already been tested for similar systems.^[93] The reference calculations from the literature were performed using the LDA functional for the corresponding spin state. If not stated otherwise, B3-LYP was used both as a starting point for GW-BSE and for the TD-DFT calculations. All spectra were obtained by broadening the vertical transitions with a Lorentzian with a full-width-half-maxima of 0.25 eV. The same broadening was applied to the experimental values, as the experimental data was only available in terms of the absorption coefficient for each peak maximum at specific wavelengths. All GW calculations were performed for a limited amount of orbitals while making use of contour deformation techniques, the resolution of identity approximation, and the *evGW* scheme. We estimated the number of orbitals required by starting with the DFT calculation and selecting orbitals around the Fermi energy, such that the norm of the transition density matrix was sufficient. We made use of a def2-TZVP basis set for both the regular and the auxiliary basis sets *cbas* and *jbas*.

3.3.1 Iron(II)

As our first example, we will investigate an iron complex $[\text{Fe}(\text{tacn})_2]^{2+}$, due to its simple d^6 structure, for which we expect a closed shell configuration with no Jahn-Teller distortion.^[94], where all t_{2g} orbitals are occupied twice. Nevertheless, we will perform geometry optimizations in both D_3 and C_1 symmetry. All geometry optimizations yet converged into the D_3 point group even if no symmetry was enforced. To perform an analysis of the transitions density matrix, which is only available in the C_1 point group in the Theodore program package, all following DFT and GW-BSE calculations are performed in C_1 symmetry. Experimental values are obtained from the referred literature.^[90] The results are shown in the figures 3.6 and 3.7.

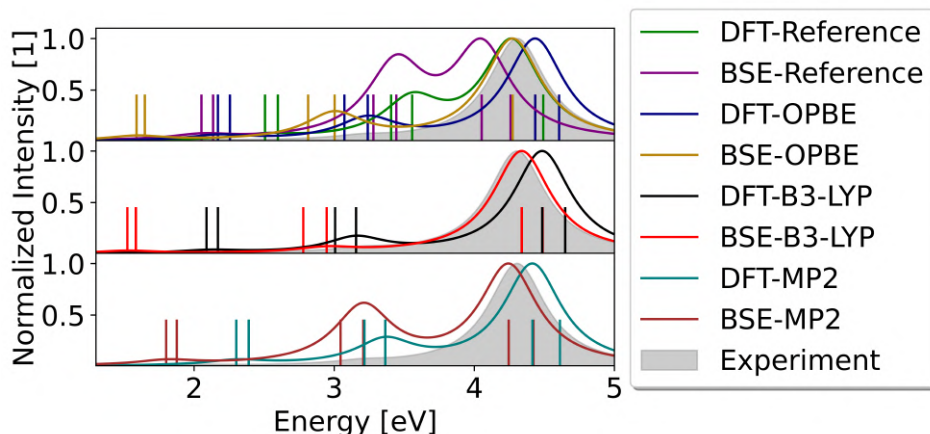


Figure 3.6: Calculated spectrum for $[\text{Fe}(\text{tacn})_2]^{2+}$, using different levels of theory and equilibrium geometries. All entries are sorted by the level of theory used to calculate the spectrum, followed by the method used to generate the geometry. The reference corresponds to calculations based on the geometry reported in the literature, using the LDA functional, whereas OPBE calculations utilize the OPBE functional.^[92] All spectra were generated using a B3-LYP starting point. One observes major differences between the calculated spectra, even when changes in the geometry are small. In particular, the oscillator strength appears to be overestimated for MC transitions.

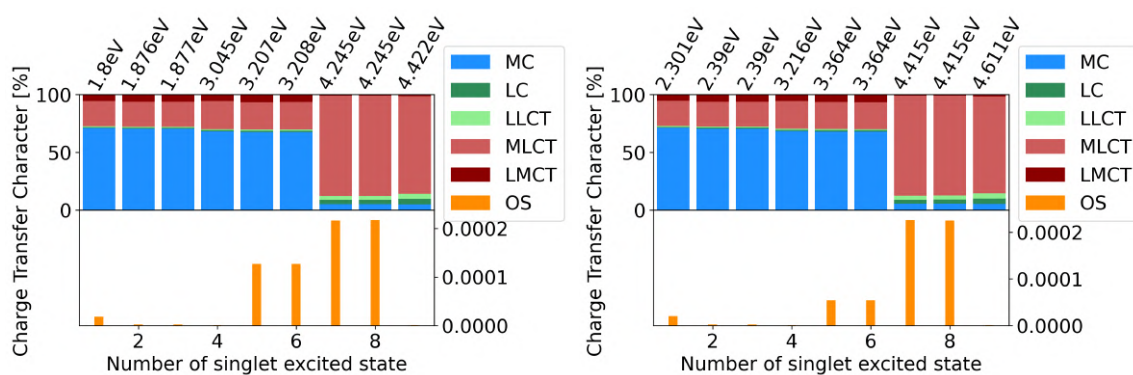


Figure 3.7: Analysis of the TDM. The left figure was done for the BSE-MP2 and the right figure for the DFT-MP2 calculation. Oscillator strength is abbreviated by OS. Both analyses yield similar results, with the first six transitions being dominantly MC transitions. The last peak has an MLCT character.

Figure 3.6 always shows the lowest 9 excitation. An analysis of the transition density matrix demonstrated that transitions beyond 4 eV have a dominant MLCT character. We are therefore more interested in the range up to 4 eV, where 3 peaks can be observed in the experimental

spectrum. They lie at 2.06 eV, 3.204 eV and 4.305 eV.^[90] All levels of theory correctly predict 2 peaks with MC character, followed by one with MLCT character, however with vastly different transition energies and oscillator strengths. For example for the BSE-MP2 level of theory, these 3 transitions are located at approximately 1.8 eV, 3.208 eV and 4.245 eV. These values are of similar quality for the first and third peaks, and of better quality for the second peak, compared to the DFT-MP2 results, which are 2.301 eV, 3.364 eV, and 4.415 eV, respectively. We see that BSE yields at least a similar but in some cases a better quality of system description relative to DFT. However, both theories are limited by accurately predicting the lowest-lying transition. We observe a similar behavior for all geometries, even though the spectra depend strongly on them. Regular DFT has problems in accurately describing the equilibrium geometry. This can be seen, by the fact mentioned above and that different functionals yield different geometries, which impacts the obtained spectra. Even if variations are small, we observe that the oscillator strengths are especially highly sensitive to them, as they can change rapidly. We obtained the best alignment when starting our calculations from an MP2 geometry or if the OPBE functional was used in combination with TD-DFT. We generally observe that the MLCT peak stays almost consistent across all calculations, whereas the MC transitions change. The BSE transitions seem to be consistently lower in energy when compared to their DFT counterparts, which appears to be a more accurate description of the spectra for this system. All in all, we see that the BSE is capable of describing the MC transitions in this complex, even if especially the oscillator strengths depend strongly on the geometry. However, this problem also arises in the DFT framework.

3.3.2 Cobalt(III)

As the next system, we have chosen $[\text{Co}(\text{tacn})_2]^{3+}$, due to its structural similarities to the iron system. Once again it will be a d^6 low spin system, which means that we do not expect a Jahn-Teller-distortion in the low spin configuration, so that all 3 t_{2g} orbitals are fully occupied, whereas the e_g orbitals are empty. This means we will proceed just like in the previous example but we will directly perform the geometry optimization in the D_3 point group. The DFT and GW-BSE steps are performed in C_1 . All results are shown below in figure 3.8 and 3.9.

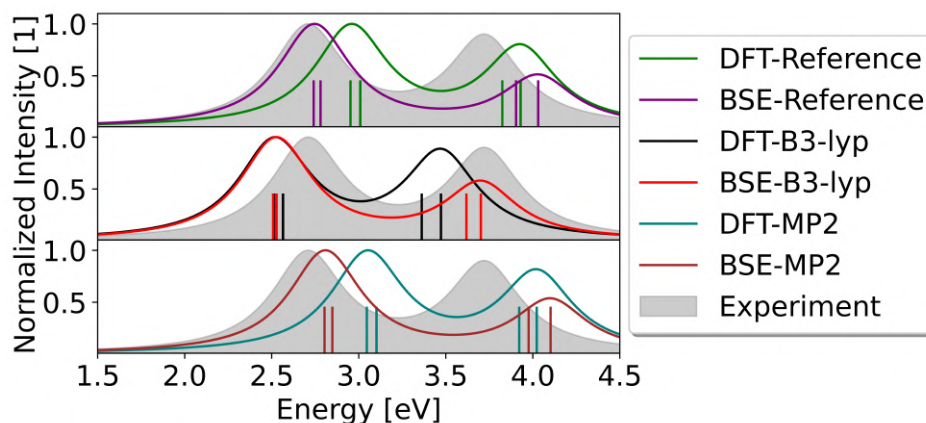


Figure 3.8: Calculated $[\text{Co}(\text{tacn})_2]^{3+}$ spectra for different levels of theory with different equilibrium geometries. Reference refers to an equilibrium geometry taken from the referred literature, which uses the LDA functional.^[92] We observe again a strong sensitivity to the equilibrium geometry for both theories. This sensitivity seems to be weaker for BSE, as it appears that BSE always corrects the energy of its DFT counterparts towards the experimental values.

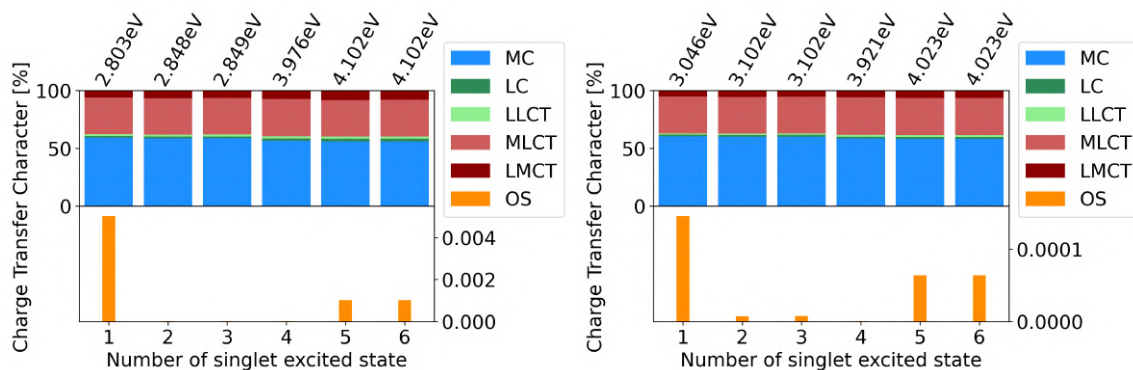


Figure 3.9: Results of the analysis of the transition density matrix. The left figure shows the results for BSE with MP2 geometry, while the right figure displays the results for DFT with MP2 geometry. All calculated transitions have a dominant MC character. Oscillator strength is abbreviated by OS.

In this case, we have the opportunity to investigate electronic transitions, that have a dominant MC character, as shown in figure 3.9. We observe once again the strong sensitivity to the geometry, as already witnessed for the iron complex. All calculations can predict a total of 6 MC transitions, even if the transition energies and oscillator strengths vary again. Interestingly, the dependence on the equilibrium geometry appears to be weaker for the GW-BSE, when compared to the DFT spectra. This can be seen, by the fact that BSE transition energies show a better alignment with experimental values. They appear to be shifted to higher or lower energies instead of just in one direction, as we have seen in the first example. In addition, they always yield spectra that are closer to the experimental values, independently of the geometry, when compared to the DFT calculation. This hints at a more accurate description of the MC states by the BSE in comparison to DFT. Both of these investigations show that the BSE yields at least similar, if not better results than DFT, which is in line with other observations, that show that BSE results are particularly good for singlet systems.^[39] Therefore, we will now proceed with open-shell systems to determine if this result holds for them as well.

3.3.3 Chrom(III)

In an attempt to investigate an open-shell system, we will start with a Chrom(III) complex. This complex has a d^3 structure, with each t_{2g} orbital occupied once. Consequently, this will be a high-spin system with a quartet multiplicity. We expect no Jahn-Teller distortions for such a system, so all geometry optimizations were performed in D_3 symmetry. However, a calculation in C_2 symmetry for the MP2 level of theory was performed, which led to an optimized D_3 geometry and confirmed this assumption. All calculated spectra, alongside the analysis of the transition density matrix, are shown in the following figures 3.10 and 3.11 and were performed without symmetry.

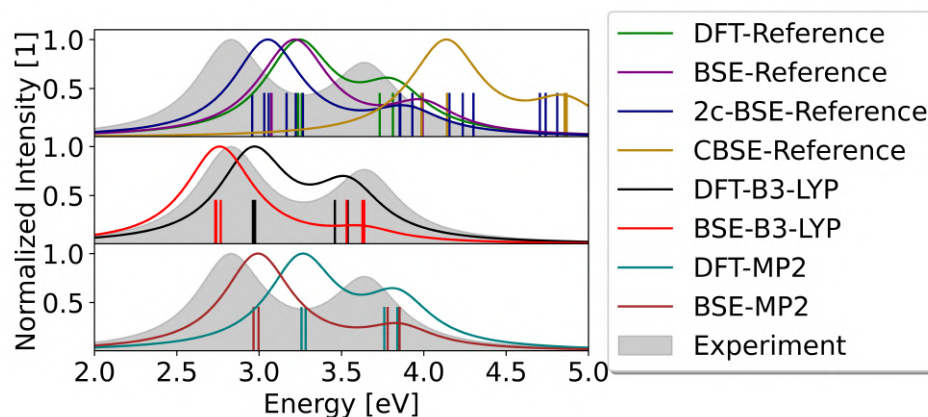


Figure 3.10: Calculated spectra for $[\text{Cr}(\text{tacn})_2]^{3+}$. The same notation as in the previous examples was used. As in all calculations, we observe a strong variation of the spectra as a function of the equilibrium geometry. Both theories overestimate transition energies by approximately 0.5 eV for the reference geometry. GW-BSE calculations with additional calculations appear to worsen the alignment with the experimental values, shifting the entire spectrum to higher energies. In contrast, accounting for spin-orbit coupling by performing the calculation with two component spinors results in a shift towards lower energies and a better alignment. DFT with the B3-lyp functional tends to overestimate the Cr-N distance, which therefore leads to lower transition energies.

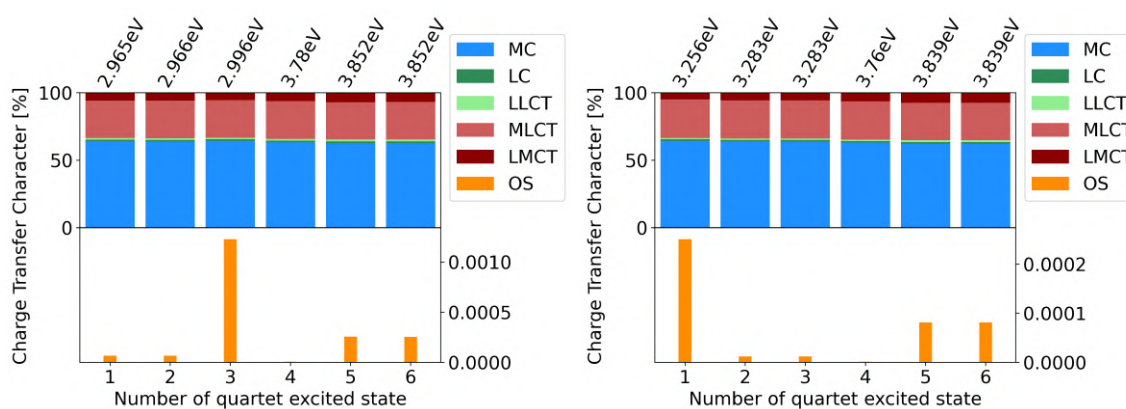


Figure 3.11: Analysis of the transition density matrix for the BSE-MP2(left) and DFT-MP2(right) levels of theory. Oscillator strength is abbreviated by OS. All investigated states have a dominant MC character, as can be seen in both figures. Nevertheless, the oscillator strengths vary strongly.

The figures above make it clear that geometry dependence persists in the case of open-shell systems. This again emphasizes that accurate theories to predict the geometries are required since both the DFT and GW-BSE results are susceptible to them. We observe that both theories predict 6 possible low-lying transitions with MC character but at the same time, they tend to overestimate the transition energies of the system. However, DFT seems to yield results that align worse with the experimental values when compared to the GW-BSE calculations. The reference and MP2 calculation yield similar geometries and therefore similar spectra for both levels of theory. The DFT B3-lyp optimized structure overestimated the Cr-N bond length at 2.129 Å when compared to experimental values which predict a bond length of about 2.062 Å - 2.085 Å^[95]. In comparison, the MP2 geometry optimization results in a Cr-N bond length of 2.071 Å. The larger bond length in the DFT framework lowers all vertical transition energies. In addition to the standard DFT and GW-BSE procedures we also performed two-component

and correlation augmented calculations. We observe that additional correlation shifts the entire spectrum to higher energies, without changing its shape. This is not the desired result, as both levels of theory already appear to overestimate the vertical transition energy. The inclusion of spin-orbit coupling by performing the calculation with two-component spinors instead of regular molecular orbitals improves the results slightly, however, a more detailed investigation of spin-orbit coupling effects will be done in chapter 3.5. While the transition energies show a decent alignment, the oscillator strengths appear to be vastly different for both levels of theories. Overall, we can conclude that the GW-BSE yields similar results for this particular open-shell system as for the closed-shell case. We observe that GW-BSE appears to be able to improve the DFT results, however, it yields no solution to the problem with the equilibrium geometry due to its nature of being a framework only for the excited state. Furthermore, the issue of inaccurate oscillator strengths persists.

3.3.4 Nickel(III)

To continue with further open-shell systems we decided to investigate a Nickel complex. For such a d^7 system one can expect Jahn-Teller distortion, particularly for a low-spin configuration. Since it is known that DFT lacks the needed accuracy to predict the correct spin state for the electronic ground state of such a system, we opted for CASPT2 calculations. These calculations were performed by Sergey Bokarev using the CASSCF and CASPT2 Module of openMolcas, using MP2-optimized geometries.^{[96][97]} For the CASSCF calculation an active space of 11 electrons in 10 orbitals was chosen. This resulted in a low-spin (doublet) configuration, which lies approximately 0.053 Ha below the high-spin (quartet) configuration. We have therefore chosen to perform the geometry optimization and spectra calculation in the doublet state, for which we expect a strong Jahn-Teller distortion, which is why all geometry optimizations were performed in C_2 symmetry. For this system, we will also use different functionals as starting points for the GW calculation. All obtained results are depicted below in the figures 3.12 and 3.13.

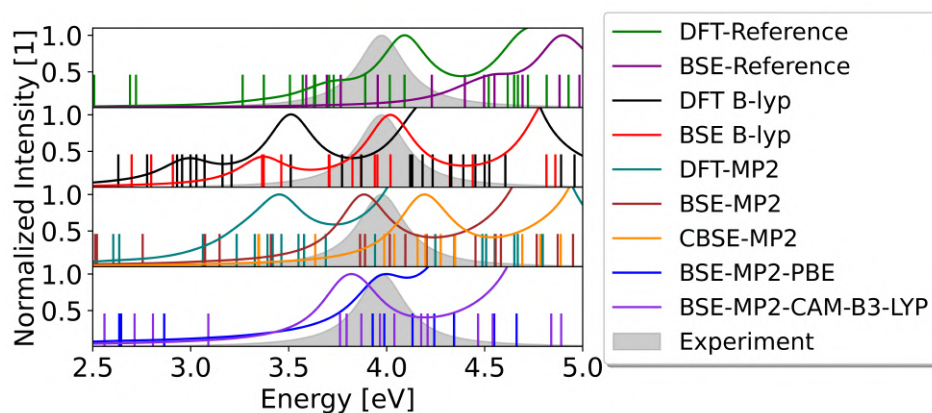


Figure 3.12: Calculated spectra for $[\text{Ni}(\text{tacn})_2]^{3+}$. The same notation as in the previous examples has been used. However, in the final case, additional GW-BSE calculations on the MP2 geometry were performed using two different functionals. We see that geometries that have been generated based on DFT exhibit completely different spectra when compared to the MP2 geometry. In particular, the shape of the spectra changes, resulting in the appearance of two peaks, whereas the experiment indicates the presence of only one peak. Calculations with the MP2 geometry yield spectra that align with experimental values, yet GW-BSE appears to further improve them compared to regular TD-DFT calculations. Different starting-point functionals for the GW part lead only to small changes since the GW cycle is solved self-consistently.

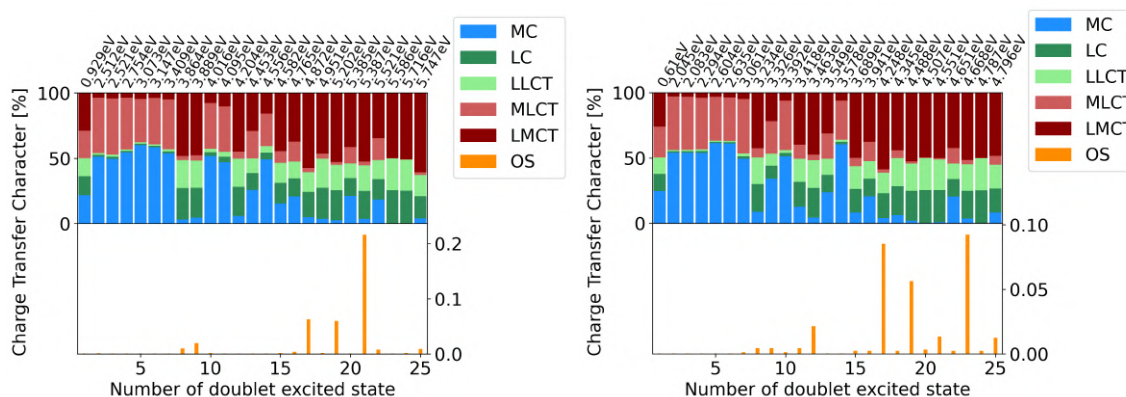


Figure 3.13: Decomposition and analysis of the transition density matrix for $[\text{Ni}(\text{tacn})_2]^{3+}$. The left figure shows the obtained results for the BSE-MP2 and the right figure for the DFT-MP2 calculations. All transitions with non-zero oscillator strength have a mixed character with the largest contribution being LMCT.

For the first time, the DFT geometries result in spectra that differ not only in their energies but also in their shape when compared to the MP2 geometries. All DFT geometries produce a spectrum with two peaks, whereas the MP2 geometries result in only a single peak. The latter is also what we expect based on experimental values. This demonstrates not only that DFT lacks the accuracy needed to predict the spin state, but also the equilibrium geometry. This failure can be seen clearly if one takes a look at the Ni-N bond lengths. DFT B3-lyp predicts a bond length of 2.266 Å for the long and 2.046 Å for the two short axes, whereas experimental values hint at 2.109 Å and 1.971 Å for the two axes.^[98] The MP2-optimized structure yields a more accurate description at 2.137 Å and 1.989 Å and therefore a spectrum that shows a better alignment with experimental values. A look at figure 3.13 suggests a strong mixing of different states that play a role in these spectra. We also observe that GW-BSE yields no improved solutions, if fundamental properties such as the spin state and the equilibrium geometry are not properly described in advance. For the MP2 geometry, we observe once again that the GW-BSE theory improves the results obtained from TD-DFT calculations. Based on the analysis of the transition density matrix in Figure 3.13, we observe that the peak of interest at 4 eV has a mixed character. While the largest contribution comes from LMCT, LLCT and LC also play significant roles. This is confirmed by the TD-DFT calculation, which yields similar results and demonstrates that GW-BSE does not favor a certain type of transition, since its spectra align well with the experimental values, even if the transition has a mixed character. Although different functionals result in slightly different spectra, they all produce a single peak at around 4 eV. This observation is consistent with the experimental results. We will find in the next chapter, that the inclusion of self-consistency in the GW step can nearly eliminated the dependence on the original exchange-correlation functional. The same can be seen in this case already, since completely different functionals yield similar spectra. Overall, we observe that the GW-BSE spectra show a decent alignment with the experimental values for the MP2 structure. This indicates that GW-BSE is capable of properly describing states with a strong mixing of different charge transfer characters. Since DFT is incapable of achieving the same, this appears to be a significant advantage of the GW-BSE framework.

3.3.5 Cobalt(II)

As a final example, we investigated a Cobalt(II) system. We opted for a similar scheme as in the case of the previous Nickel complex. $[\text{Co}(\text{tacn})_2]^{2+}$ is a d^7 system for which DFT is unable to accurately predict the spin state. CASPT2 calculations on the MP2 optimized equilibrium geometry suggested a high-spin configuration with a quartet multiplicity. The low-spin total energy was approximately 0.04 Ha higher than the high-spin total energy. For the CASSCF step, 11 electrons in 10 active orbitals were chosen as the active space. Experimental values suggest no Jahn-Teller distortion for such a system and a Co-N bond length of 2.161 Å^[99]. The obtained results are shown below in figures 3.14 and 3.15.

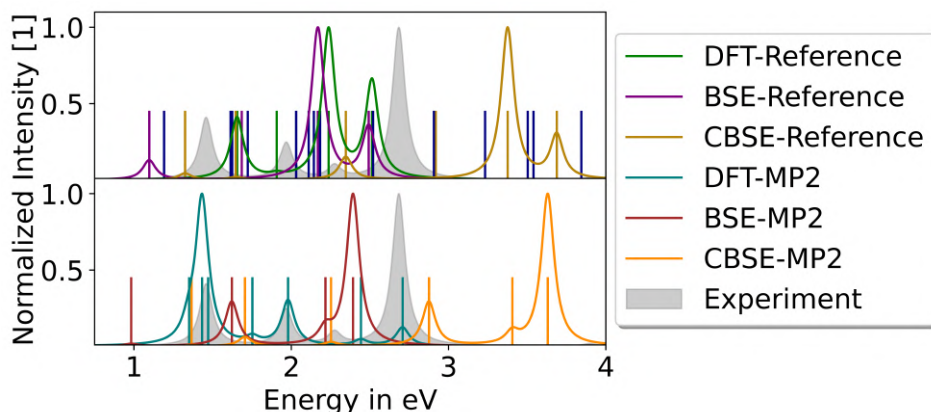


Figure 3.14: Calculated spectra for $[\text{Co}(\text{tacn})_2]^{2+}$. Both DFT and GW-BSE are not capable of confirming the experimental spectrum. We observe a strong misalignment for both geometries. The inclusion of additional correlations worsens the alignment, since it shifts the entire spectrum to higher energies, without changing its shape. This system is a demonstration of the limitations when working in the GW-BSE framework.

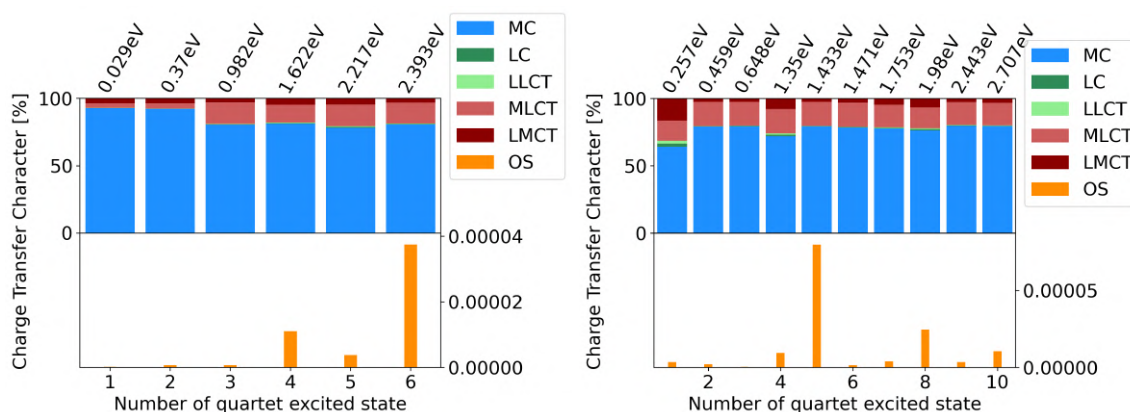


Figure 3.15: Decomposition of the transition density matrix for the BSE-MP2 (left figure) and the DFT-MP2 (right figure) calculation. All observed transitions exhibit a dominant MC character, although DFT predicts more possible transitions below 3 eV compared to GW-BSE.

For the first time in this work, we observe a strong mismatch between the calculated and the experimental spectra. GW-BSE also is not capable of improving these results. The inclusion of additional correlation in the form of CBSE only shifts the entire spectra to higher energies, which is not sufficient because the shape of the theoretical spectrum does not align with the experiment. A possible explanation for this behavior could be a wrong geometry. Both MP2 and DFT fail at predicting the correct Co-N bond length, for which they predict 2.225 Å in the

MP2 case and 2.032 Å for DFT. These values are either an underestimation or an overestimation of the experimental value of 2.161 Å. As part of the CASSCF calculation, we witnessed already that a rather large active space was necessary, which hints at this system being highly multi-configurational. We estimate that DFT's incapability to describe these systems accurately originates from the fact that DFT is a framework built only on a single determinant. Since GW-BSE takes a DFT input as a starting point, we estimate that the same holds here, as it inherits this property. This would also explain, why the obtained equilibrium geometries are incorrect, which ultimately leads to worse spectra since GW-BSE is not able to make predictions on the structure. This system greatly demonstrates the limitations of the GW-BSE theory.

Overall, we can learn from these previous five examples that the GW-BSE theory does not only yield proper results for the charge transfer transitions but also metal-centered transitions for a lot of systems. This advantage comes however at additional computational cost in the form of the calculation of the GW quasiparticle energies. Furthermore, the GW-BSE is exclusively a method to calculate excited state properties. This means that it does not offer an option to predict ground state properties, such as the ground state geometry or the spin state. This has the consequence that these properties have to be calculated using different methods, such as DFT or MP2. Unfortunately, the results of GW-BSE are susceptible to these properties, thereby requiring their calculation with exceptional precision in advance. If this is not the case, as seen in the case of the Co(II) complex, this will lead to spectra incapable of predicting experimental spectra. It might be true that the same can be said for features that are not captured by the starting point calculations. If a system must be described by more than one determinant, we cannot expect GW-BSE to improve these aspects.

With our newly developed understanding of the accuracy of the long-range behavior of charge transfer states, the accuracy of MC transitions, and the accuracy of states with mixed characters, the question arises whether this accuracy extends to larger systems. As mentioned earlier, large metal complexes often contain numerous states with dominant MLCT but also mixed characters. Therefore, we will continue in the next chapter with larger systems that include these transitions.

3.4 MLCT-States of closed shell Fe(II) Complexes

Much effort has lately been put into developing accurate theories to describe the electronic structure of transition metal complexes. A common method involves using range-separated exchange-correlation functionals, such as LC-BLYP. The conceptual idea is to perform TD-DFT calculations with exchange-correlation functionals that involve a set of parameters $\{\alpha, \beta, \omega, \dots\}$. They are used to increase the amount of exact HF exchange gradually. These parameters are then tuned based on exact DFT properties or experimental values.^[100] Numerous case studies have already successfully applied this framework to predict the spectra of various molecular systems.^[101] It results in MOs with a usually better description of charge transfer states at the cost of perhaps worsening the description of other states. As mentioned before, both types of transitions are unfortunately relevant, so we will now apply the GW-BSE theory to calculate the UV-vis spectrum of iron complexes as important test systems. As a case study, we have chosen 3 examples for which TD-DFT and experimental data were already available.^[102] In this instance, the effect of the position of the nitrogen on the spectra was examined. The presence of nitrogen is expected to have an impact on the location of the corresponding MLCT or MC states. At first, we confirmed the reference calculation, by calculating the spectrum using different exchange-correlation functionals. From now on, all vertical transitions calculated were broadened by a Lorentzian function with a full-width-half-maximum of 0.25 eV to obtain the spectra. If not explicitly stated otherwise, all calculations were performed using a def2-TZVP basis set. For all calculations, we decided to opt for the resolution of identity (RI) approximation, to lower the computation cost. The auxiliary basis sets (jbas and cbas) were always of the same quality as the regular ones. The result is shown below.

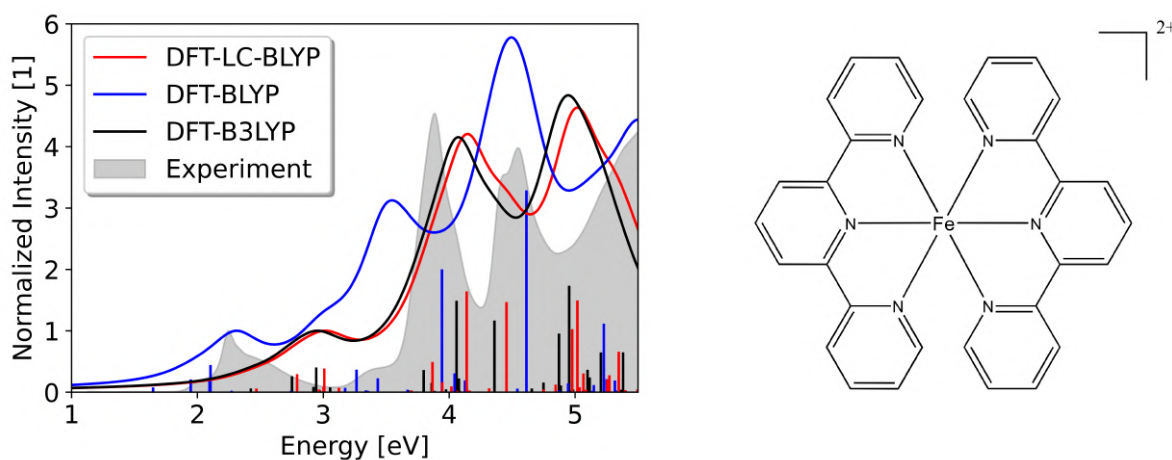


Figure 3.16: Structure of the investigated iron complex $[Fe(terpy)_2]^{2+}$ (complex K5 of the literature).^[102], along with its calculated UV-vis spectrum. Each line shows a spectrum calculated with a different exchange-correlation functional. For the LC-BLYP functional we have chosen $\alpha = 0.2$, $\beta = 0.8$, and $\omega = 0.07$ in alignment with the literature. One can witness the issues that arise naturally when relying on DFT calculations. One observes significant differences between different functionals and consequently differences in the quality of the description. In particular, the MLCT transition at 2.3 eV is not properly described by this calculation. Moreover, the intra- and interligand transitions at energies higher than 3 eV vary strongly.

A comparison to the experiment demonstrates clearly the problems that arise when working in the DFT framework. The calculated spectrum depends strongly on the chosen functional, which leads to a strong misalignment when compared to the experiment. Especially, the first transition peak (which we will later in figure 3.19 identify as the MLCT peak) at around

2.3 eV is described poorly. In the case of the B-LYP, the first peak appears to align, however at the expense of a worse description of the transitions beyond 3 eV. In general, the calculated transitions beyond 3 eV appear inaccurate for all functionals. Unfortunately, there appears to be no systematic approach to improve the results by modifying the used functional, as each yields different transition energies and oscillator strengths. For this reason, we performed the calculation again, but within the GW-BSE framework, in hopes of finding a more systematic approach to deal with this problem. The results are shown below in figure 3.17 and 3.18.

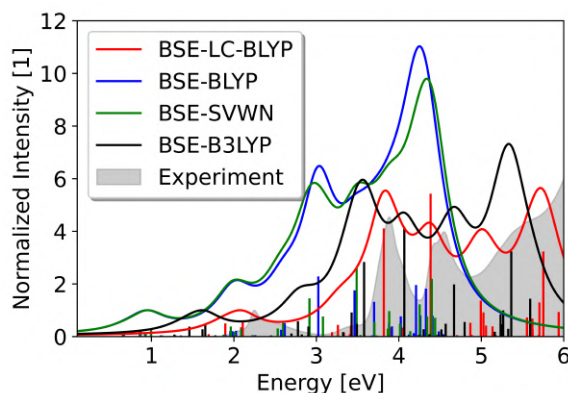


Figure 3.17: Calculated UV-vis spectrum at the G_0W_0 -BSE level of theory, using the spectral method. Major differences between different starting points can be seen, as each functional yields a different spectrum. Particularly, the rather cheap SVWN functional fails to predict the experimental values. In contrast, the LC-BLYP functional yields already improved results that align with the experiment.

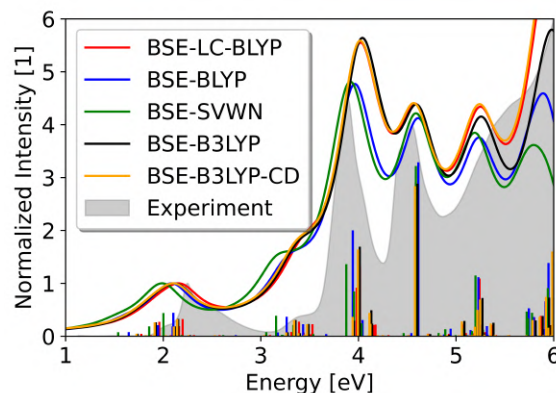


Figure 3.18: Calculated UV-vis spectrum at the $evGW$ -BSE level of theory. All spectra are calculated using the spectral methods, besides the last calculation, which involved the B3-LYP functional and contour deformations (CD) techniques. All calculations required at least five to seven GW interactions to reach convergence. It is noteworthy, that all calculated spectra are independent of the starting point. Furthermore, one observes an excellent agreement of all spectra with experimental values.

The first figure 3.17 shows single shot G_0W_0 -BSE calculations. Here we observe that the results still depend as expected heavily on the starting point aka. the underlying DFT calculation. It appears that for certain functionals the quality of the obtained results worsens, as the MLCT peak is strongly shifted to lower energies. This is the case for all functionals, however, to a lesser extend for the range-separated functional LC-BLYP. This is an important result, as it is known that single-shot GW energies align well with experimental values if functionals with large exact HF exchanges are used.^[103] Apparently, this also applies to systems of metal complexes, where a single GW iteration is sufficient, to produce results that align roughly with experimental spectra.

In the next step, we performed self-consistent GW calculations, as can be seen in figure 3.18. It is evident that from the very beginning, through several GW iterations, most information about the initial exchange-correlation functional is lost. This can be seen by the fact that the SVWN and LC-BLYP functionals, which initially produced vastly different results, now yield nearly identical outcomes. We assume that the minor differences between them result from the approximations used, such as the eigenvalue-only self-consistent approximation. Moreover, we observe a good alignment with the experimental spectrum, not only energy-wise but also because the oscillator strengths appear to rather be accurate. Figure 3.18 also shows the validity of contour deformation techniques, as discussed in chapter 2.5.3. We observe that both spectra calculated using the spectral and contour deformation methods align, especially for low-lying transition.

To further investigate this system, the transition density matrix was analyzed to determine each transition's charge transfer character. The results are shown in figures 3.19 and 3.20 for both the DFT and the GW-BSE levels of theory.

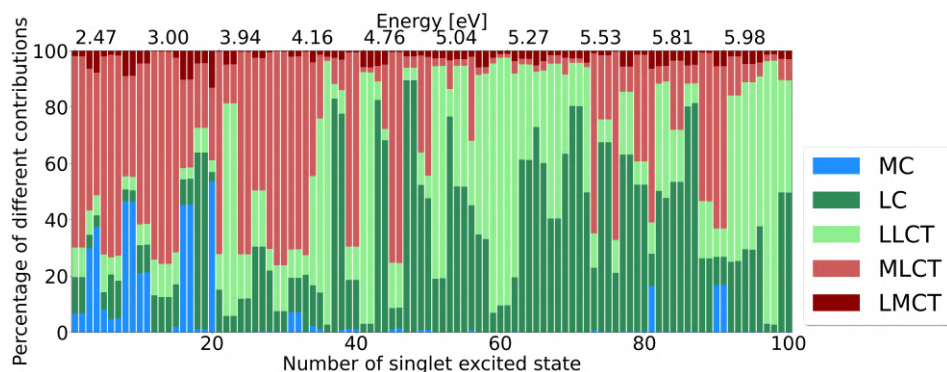


Figure 3.19: Analysis of the DFT transition density matrix for the LC-BLYP functional and a def2-TZVP basis set. Most MLCT transitions are located before 4.2 eV. The remaining transitions are mostly characterized by transitions taking place on the ligand. 2 low-lying MC transitions can also be observed, however, most states demonstrate a strong mixing.

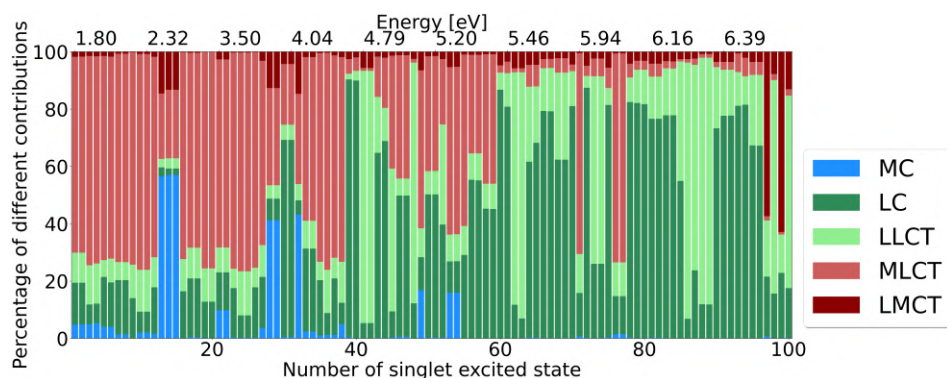


Figure 3.20: Analysis of the BSE transition density matrix for the LC-BLYP functional. The calculation was performed using a regular def2-TZVP basis set. We observe that most transitions in the low energy region of below 4 eV have a dominant MLCT character. A small amount of MC states exist as well at higher energy such that the lowest singlet states all have an MLCT character. This aligns well with CASSCF results which suggest the same. Beyond 4.5 eV, most transitions take place on the ligand.

Remarkably, both theories produce spectra that differ not only in their transition energies and oscillator strengths but also are composed of transitions with different characters. DFT predicts that most low-lying states have an MLCT or a strongly mixed character, whereas the GW-BSE transitions show a weaker mixing. However, we find that both theories accurately predict that the lowest singlet state has a dominant MLCT character, which is what we expect based on CASSCF calculations.^[102] CASSCF predicts the lowest MLCT state at 2.23 eV and MC state at 2.27 eV. In the DFT case, the lowest excited MLCT state is located at 2.47 eV. For the MC states, the mixing between different states is too strong to accurately assign an MC character to a single state. GW-BSE predicts the first excited MLCT state at 1.80 eV, which is an underestimation of the CASSCF value. However in this case it is possible to assign an MC character to states 13,14 and 15. The lowest of them is located at 2.66 eV, which is an overestimation.

The next important factor is the charge transfer characters of the states at the triplet equilibrium geometry, as it is not only necessary to describe the singlet but also the triplet states accurately. For this, we performed a geometry optimization for the triplet ground state, followed by a GW-BSE calculation, using the same parameters as before, to compute the spectrum. The differences in the Metal-to-Ligand bond length are shown in the table 3.1.

Bond	Singlet (Å)	Triplet (Å)
Fe-N ₁	1.96372	2.14757
Fe-N ₂	1.96372	2.14757
Fe-N ₃	1.96372	2.14757
Fe-N ₄	1.96372	2.14757
Fe-N ₅	1.87903	1.93599
Fe-N ₆	1.87903	1.93599

Table 3.1: Comparison of bond lengths between the singlet and triplet equilibrium geometry.

We observe that the triplet equilibrium geometry comes with a longer bond length between the metal and ligand, which is expected. At this new equilibrium geometry, we performed an analysis of the charge transfer character, which is shown in figure 3.21.

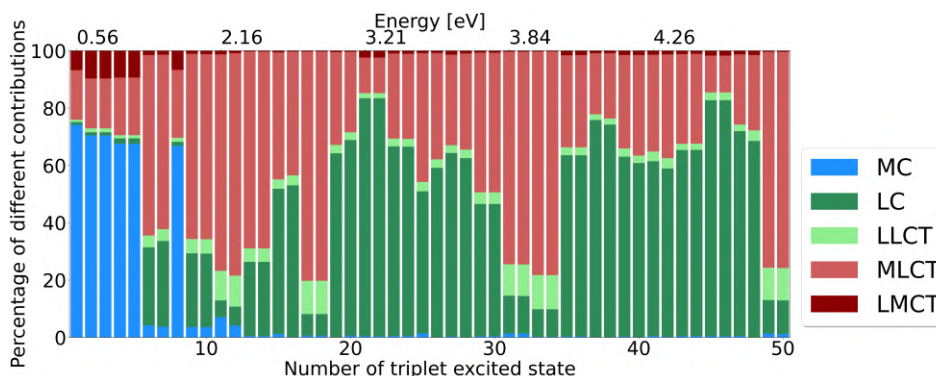


Figure 3.21: Analysis of the BSE transition density matrix for triplet excitations at the triplet equilibrium geometry, involving the LC-BLYP functional and def2-TZVP basis set. The lowest excited states are predicted to have an MC character, which is the expected behavior. In contrast to TD-DFT, the GW-BSE framework appears to naturally produce this correct ordering of triplet MC states being located below triplet MLCT states.

We can observe that the GW-BSE framework is capable of accurately predicting that the triplet MC states are the lowest excited states. This suggests that the GW-BSE framework has the advantage of naturally including such effects, whereas TD-DFT calculations are unable to predict the correct ordering unless tuned range-separated functionals are used.^[102] However this advantage comes at the additional computational cost of calculating quasiparticle energy through the GW cycle.

This short analysis hints at the fact that the GW-BSE treats all possible types of transitions equally. We put more emphasis on the alignment with the experimental spectra than the CASSCF calculation, which suggests that a more accurate description of MLCT transitions does not appear to lower the quality of the MC/LC/LLCT transitions, as in the case of TD-DFT. This can be seen by the fact that the spectra in figure 3.18 show a better alignment with the experiment across the entire energy range, which includes different types of states. Furthermore, we observe that the assignment of different states is more clear and

the ordering of the triplet states appears to be correct for the GW-BSE case, even if the exact vertical transition energies differ from CASSCF calculations.

Before proceeding, it is crucial to ensure that all this discussed behavior is not unique to the investigated system, so we will perform a similar analysis for two additional iron complexes, where the ligand was slightly modified.

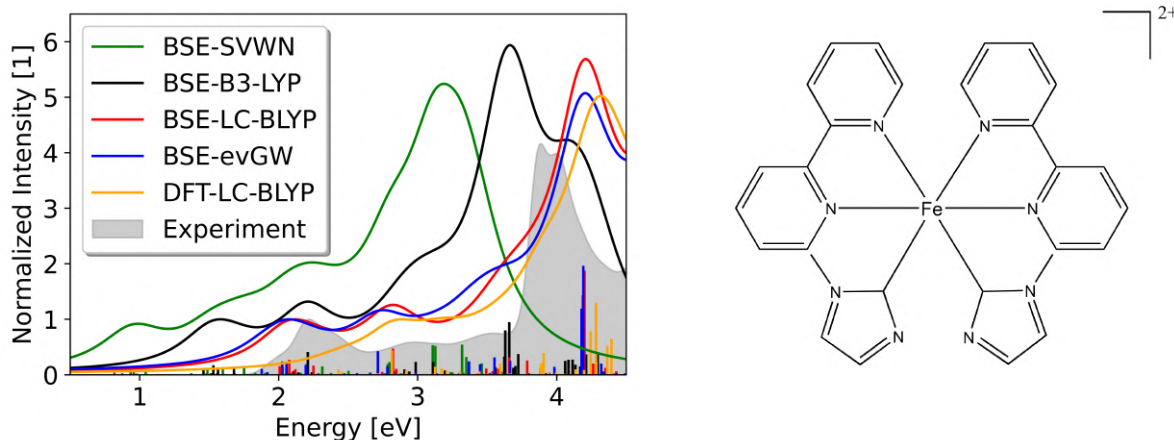


Figure 3.22: Spectrum and structure of $[\text{Fe}[\text{1-(2,20-bipyridyl)-3-methyl-imidazol-2-ylidene}]_2]^{2+}$ (complex K4 of the literature).^[102], calculated using the spectral method. All computations were conducted using the single-shot GW approach, except the final evGW calculations, which included self-consistency in the GW step starting from an LC-BLYP reference. As discussed in the previous example in figure 3.18 and 3.17, one can observe a similar behavior. Once again the single-shot calculations fail to properly predict the experimental values, except if a range-separated functional was used. The self-consistent calculation demonstrates a decent alignment with experimental data, with a deviation of the MLCT peak of about 0.15 eV from the experimental value.

Figure 3.22 shows the calculated spectrum for a similar system as in the first example. It is possible to immediately observe similarities between those two calculations. Again, the single-shot GW calculations lack the required accuracy needed to reproduce the experimental results. Self-consistency is required to confirm the experimental spectrum, except in the case where the range-separated functional was used. We observe that the theoretical results still slightly underestimate the position of the MLCT peak at 2.2 eV, in a similar manner as in figure 3.18. Overall, we still obtained improved results when compared with the DFT results and if self-consistency is achieved. This is especially seen in the case of the MLCT peak, which DFT predicts to be slightly below 3 eV, which is an overestimation when compared to the experiment. Furthermore, results are now mostly independent of the exchange-correlation functional in the self-consistent case. For the LC-BLYP functional we observe once more that a single GW cycle is almost sufficient to obtain the self-consistent results. A third and last example is shown below in figure 3.23.

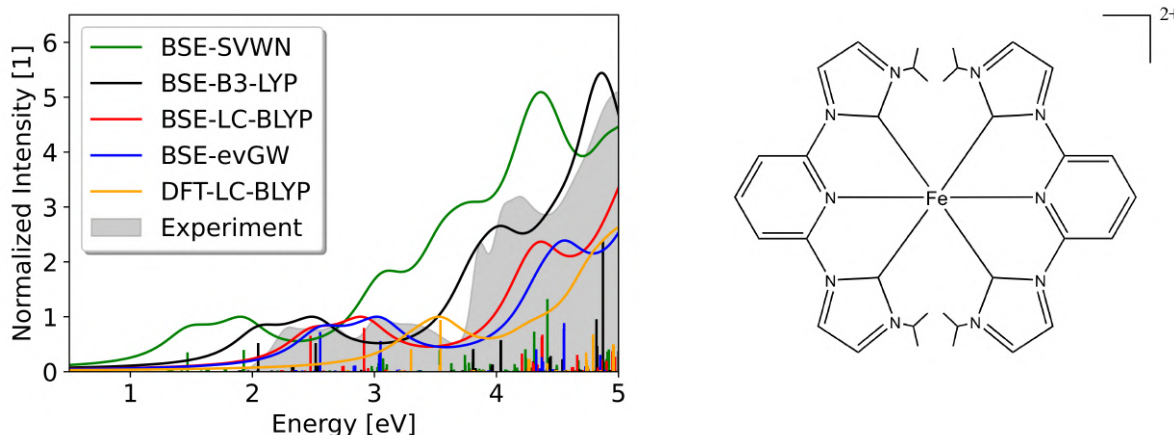


Figure 3.23: Spectrum and structure of $[\text{Fe}[2,6\text{-bis}[3\text{-isopropylimidazol-2-ylidene]pyridine}]_2]^{2+}$ (complex K2 of the literature).^[102] The same methodology as in the previous two examples was employed. However, for the self-consistent calculation, contour-deformation techniques were utilized this time due to the higher computational cost. Similar trends to those observed in the preceding examples persist, emphasizing the capability of the GW-BSE framework to accurately predict experimental spectra for MLCT transitions in transition metal complexes.

With this calculation, we observe the ability of the GW-BSE framework to successfully improve existing DFT calculations, while also removing the dependency on an exchange-correlation functional. This comes with additional computational effort. This additional effort was primarily due to the computation of quasiparticle energies since the self-consistent GW-BSE calculations required approximately four times the effort compared to the TD-DFT calculations. This is in line with our findings in the previous chapter 3.2. We observe again that the locations of the transitions are accurate in comparison with the experiment for self-consistent calculations.

With this knowledge, we can close this chapter about the investigation of MLCT transitions. We have seen that the GW-BSE framework yields acceptable results, even if states have a strong mixed character. This aligns with our findings from the previous chapter where we have seen similar effects in a Nickel complex. However, before we can investigate the possibility of performing dynamic simulations we will have to take a closer look at the accuracy of the Tamm-Dancoff approximation, as discussed in the chapter 2.6.2, as this will yield an important tool. This will also allow us to investigate in greater detail the impact spin-orbit coupling has on the spectra computed with GW-BSE. This will therefore be the topic of the next chapter.

3.5 The Inclusion of Spin-Orbit Coupling

We need to investigate two remaining aspects to prepare for dynamics simulations with this new framework. At first, comes the necessity to approximate CI vectors using transition density matrices. This is an essential step to compute the overlap matrix for a potential LVC model, as explained in chapter 2.7 and the literature.^[65] A possible solution to this offers the Tamm-Dancoff Approximation (TDA), as discussed in chapter 2.6.3. We can potentially approximate the CI vector at the cost of some accuracy through this approximation. Therefore, we need to investigate whether this approximation still yields acceptable results. Furthermore, we are interested in the accuracy of the spin-orbit coupling (SOC) between different states, as it is a major factor in computing the inter-system crossing rate during the dynamics simulations. Therefore, we will perform two different investigations using the two major methods introduced in chapter 2.8. At first, we will perform a full two-component GW-BSE calculations for a Vanadium complex. In the Second stage, we will test obtained SOC parameters against the ones obtained from other levels of theory, mainly ADC(2). These are two different techniques, as full two-component calculations do not yield the SOC strength but instead the energy of different states under the influence of SOC. We assume that if SOC effects are accurately described by these two component calculations, then the perturbative computation of these effects will also be accurate if the coupling does not become too large.

3.5.1 Two-component GW-BSE

The investigated system is a Vanadium complex called $[V(Cl)_3(ddpd)]$ with $(ddpd) = (N,N'$ -dimethyl- N,N' -dipyridine-2-yl-pyridine-2,6-diamine) and has already been studied in great depth in related work.^[104] Its structure is shown below in figure 3.24.

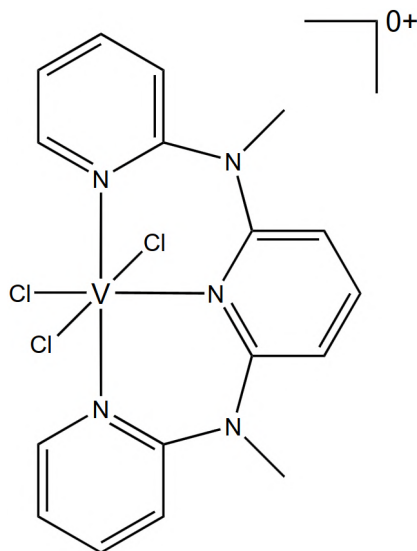


Figure 3.24: Structure of $[V(Cl)_3(ddpd)]$. The goal will be to perform full two-component GW-BSE calculations and compare them to their DFT or CASSCF counterparts. We will investigate the obtained spectra, with a particular interest in the low energy region, as this system is known for exhibiting a small splitting of the triplet ground state due to spin-orbit coupling.

We will perform both regular GW-BSE, as well as two-component calculations. This way it allows us to test the capabilities of the TDA, as well as SOC effects. Both calculations will be performed with an additional dielectric continuum model to mimic solvation effects. For this, we have chosen a dielectric constant of 37.5.^[105] This corresponds to acetonitrile, which is the solvent used in the experimental work. For the one-component calculations, a def2-TZVPP basis set was used and Hedin's equations were solved within the evGW scheme using the spectral method. For the two-component calculations, we opted for an x2c-TZVPall-2c basis set and the GW step was performed self-consistently with contour deformation techniques. For the latter, the correlation part of the self-energy was calculated for all spinors ranging from HOMO-47 to LUMO+21. As a starting point we used either a B-LYP DFT calculation or orbitals obtained from HF. All one-component calculations were performed using the DFT starting point. All obtained results are shown in the following figure 3.25.

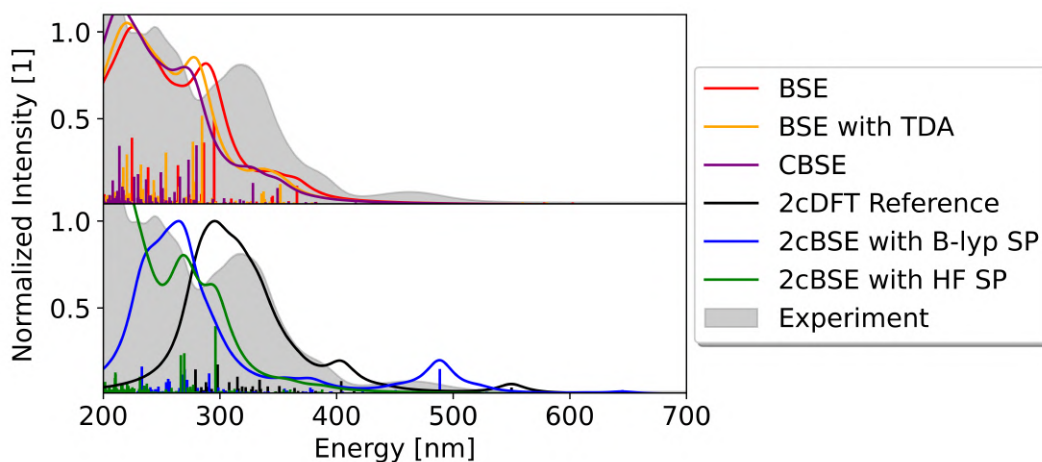


Figure 3.25: All computed spectra for the one-component (top figure) and two-component framework (bottom figure). The latter includes spin-orbit coupling, as a spinor describes each molecular orbital. The starting point is abbreviated to SP. Reference refers to calculations taken from the literature.^[104] All one-component computations used a B-LYP starting point. In this case, we observe that TDA does not greatly deteriorate the quality of the obtained spectra. We observe a small shift towards higher frequencies, which results from higher correlation. However, a lack of oscillator strengths can be observed, especially for transitions before 300 nm. We observe that spin-orbit coupling is required to explain excitations that appear at long wavelengths. The experimental spectrum exhibits low-lying transitions at around 700 nm, caused by the triplet splitting due to spin-orbit coupling. BSE appears to be capable of predicting these transitions, with decent accuracy. Nevertheless, full two-component calculations do not greatly improve the oscillator strengths.

In the figure above we can directly observe the impact TDA and spin-orbit coupling have on the obtained spectra. At first sight, the one-component calculations appear to yield reasonable results for high-lying transitions. The application of TDA results in a slight shift of the entire spectrum towards higher energies. Overall, it does not appear to change to obtained spectrum a lot. Nevertheless, the one-component calculations lack the necessary accuracy to predict low-lying transitions accurately. This can be seen by the fact that no transitions with significant oscillator strengths are observed before 400 nm. This is also a phenomenon we already observed in the previous chapters. The two-component calculations result in additional transitions at low energies. The experiment suggests transitions around 702 nm ($14\,245\text{ cm}^{-1}$), which CASPT2 can confirm by predicting the lowest excited triplet state at $14\,968\text{ cm}^{-1}/16\,464\text{ cm}^{-1}/17\,393\text{ cm}^{-1}$ above the ground state.^[104] The performed GW-BSE calculations with a DFT starting point yield 3 low-lying transitions with significant

oscillator strength at $15\,500\text{ cm}^{-1}/16\,319\text{ cm}^{-1}/19\,144\text{ cm}^{-1}$. We assume that these transitions correspond to the lowest split triplet states. Unfortunately, the two-component BSE results yield a significant number of ghost and mixed states in the low energy range, which makes it necessary to investigate this system further to confirm this hypothesis. In addition to the lowest split state, we also observe that the two-component calculations predict transitions around 470 nm , which were not included in the one-component spectra. This additional peak is also described more accurately than its DFT counterpart, as it is closer to the experimental value. For both BSE and DFT, higher states beyond 400 nm are present however, they lack significant oscillator strength. Interestingly, whereas we have previously seen that a change of the starting point only has limited impact on the obtained spectra, as long as Hedin's equations are solved self-consistently, we observe in this case that a HF starting point is not optimal, as it is incapable of accurately describing the low-energy region, since it predicts the lowest possible transition at $25\,798\text{ cm}^{-1}$ or 387.63 nm .

Besides the success of the two-component GW-BSE framework, both DFT and BSE are not able to describe the split ground state, which CASPT2 suggests at $0\text{ cm}^{-1}/755\text{ cm}^{-1}/1076\text{ cm}^{-1}$.^[104] It is known that systems with degenerate or nearly degenerate states are inadequately described by a single determinant.^{[106][107]} We therefore assume that this is another limitation of this theory since DFT relies only on a single determinant and BSE inherits the limitations of DFT.

In general, we conclude from this investigation that TDA yields reliable spectra that do not change drastically in comparison to the results obtained in random phase approximation. We see that it leads to small but acceptable changes to the spectrum which justifies its use for possible dynamics simulations. However, so far our obtained data is not sufficient to confirm that it improves the results as some literature suggests.^[52]

The inclusion of spin-orbit coupling is possible, either directly by using spinors or, as we will see in the next two chapters, through the calculation of spin-orbit coupling matrix elements. The first method appears to yield decent results, however, they produce a large amount of possible states, which seems unfit for dynamics simulations. We therefore opted for the second approach, which consists of calculating SOC matrix elements directly from the response vectors, as introduced in chapter 2.8.

3.5.2 Perturbative Approach to Spin-Orbit Coupling

To test the accuracy of the spin-orbit coupling matrix elements, we performed calculations for SO_2 utilizing both the GW-BSE and ADC(2). This rather small system yields the advantage, that data is readily available to enable an analysis in more depth. For the GW-BSE calculation, we opted for a B3-LYP DFT starting point and used contour deformation techniques to solve Hedin's equations for the evGW level of theory. The correlation part of the self-energy operator was calculated for the orbital range [14, 18]. A def2-TZVP basis set was used for both calculations. The results with the obtained parameters for both theories are shown in the table below.

P multiplicity IRREP \leftrightarrow Q multiplicity IRREP	GW-BSE	ADC(2)
$1^3B_2 \leftrightarrow 1^1A_2$	45.79 (Y)	45.57 (Y)
$1^3B_2 \leftrightarrow 1^1A_2$	15.58 (Z)	11.72 (Z)
$1^3B_2 \leftrightarrow 1^1A_1$	75.37 (X)	88.26 (X)
$1^3B_1 \leftrightarrow 1^1A_2$	36.61 (X)	40.75 (X)
$1^3B_1 \leftrightarrow 1^1B_2$	15.10 (Z)	11.50 (Z)
$1^3B_1 \leftrightarrow 1^1A_1$	6.14 (Y)	3.81 (Y)
$1^3A_2 \leftrightarrow 1^1B_2$	48.42 (Y)	48.49 (Y)
$1^3A_2 \leftrightarrow 1^1B_1$	81.81 (X)	69.24 (X)
$1^3A_2 \leftrightarrow 1^1A_1$	1.65 (Z)	3.26 (Z)

Table 3.2: SO_2 SOC matrix elements for all non-vanishing contributions for the GW-BSE and ADC(2) levels of theory. All results are given in cm^{-1} . IRREP refers to irreducible representation.

We know from the referred literature that ADC(2) is an already established tool to perform surface hopping dynamics simulations.^[108] This is due to its capability to accurately predict the excited state energies as well as spin-orbit coupling energies. From the results above we can conclude that the perturbative approach alongside the GW-BSE theory yields reliable results, as the obtained values match closely the ADC(2) results. This will therefore be our method of choice when we attempt to set up a Hamiltonian for dynamics simulations.

3.6 GW-BSE-LVC Model for Pyrazine

In chapter 2.7 we discussed that the goal of this work will be to implement an LVC model suited to perform dynamics simulations. With our previously obtained knowledge, we are now in a position to calculate the required parameters κ and λ to investigate the potential energy surface of different systems. To test the accuracy of this model we commence with the simple system of pyrazine, depicted in figure 3.26. This system has already been studied in great detail in the referred literature, making use of the CASSCF method.^[109] To compare our calculations to these results, we opted for a simple model consisting only of a single tuning and coupling mode. For now, we only focus on the lowest 3 singlet states, consisting of the ground and the first two excited states. Pyrazine belongs to the D_{2h} point group. To classify the normal modes we use of Wilson's numbering scheme for benzene.^[110] The lowest excited states are the B_{3u} followed by the A_u state. Therefore, we chose the Q_{8b} mode, as it is a B_{3g} mode. The product of the irreducible representation of the normal mode with the states yields the totally symmetric irreducible representations A_g , which means we expect coupling between the two states along this mode.^[111] We chose Q_{9a} as our tuning mode. We used an aug-cc-pVDZ basis set and B3-LYP as a starting point to compare the results with the literature. Hedin's equations were solved self-consistently using the evGW scheme. Contour deformation techniques were employed for all orbitals between HOMO-2 and LUMO+4. The TDA was used for the BSE step, to fasten up calculations and to approximate CI vectors. The obtained results are shown below for the adiabatic representation in figure 3.27.

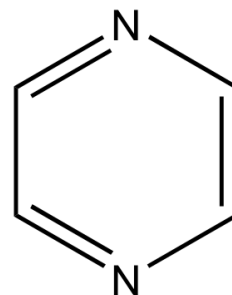


Figure 3.26: Geometry of pyrazine. The goal is to investigate the system along a tuning and a coupling mode, to demonstrate the validity of the LVC model, and to investigate the accuracy of the BSE potential energy surfaces compared to other levels of theory.

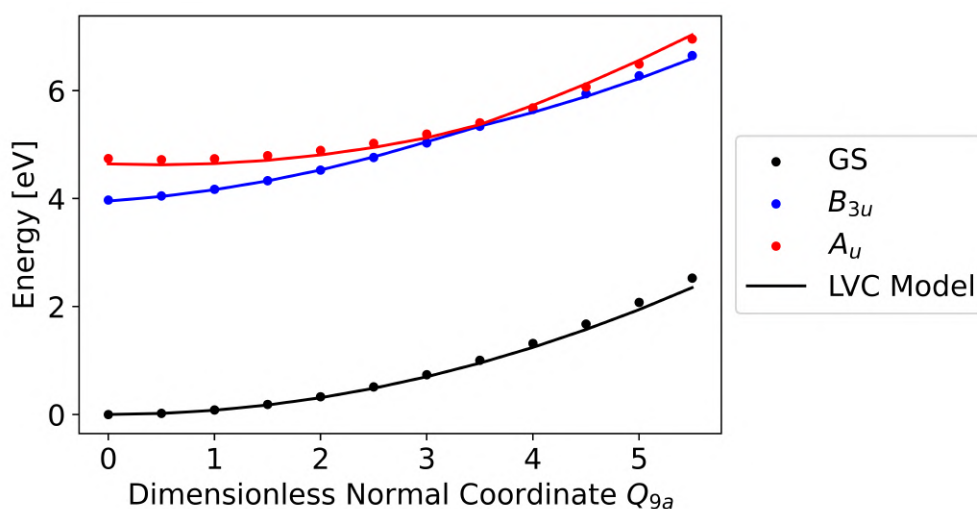


Figure 3.27: Potential energy surface (PES) of the lowest three singlet states. Q_{9a} is chosen as the tuning mode. The dots represent single-point GW-BSE calculations at the corresponding geometry. We observe that the LVC Model is capable of approximating the PES, especially for small displacements. Additionally, we observe that the coupling between the two states leads to a conical intersection around 3.5. However, the grid used is too coarse to estimate the exact position.

One can see that the coupling between the two states leads to a conical intersection between them at around 3.5 on our grid, which unfortunately is too coarse to estimate the exact position. We observe a decent alignment of the LVC model with the single-point GW-BSE transition energies. Especially around the equilibrium the PES demonstrates a strong harmonic character, which results in the LVC model being particularly effective in this range. Besides only the visual alignment, we can also compare the obtained parameters with those from similar calculations. For instance, CASSCF calculations predict the κ parameters to be $\kappa_{B_{3u}}^{ref} = 0.120$ eV and $\kappa_{Au}^{ref} = -0.064$ eV.^[109] Our GW-BSE model estimates $\kappa_{B_{3u}}^{GW BSE} = 0.133$ eV and $\kappa_{Au}^{GW BSE} = -0.073$ eV, which is a difference of approximately 10%. The experiment suggests transition energies at the equilibrium geometry of $\epsilon_{B_{3u}}^{ref} = 3.83$ eV^[112] and $\epsilon_{Au}^{ref} = 5.0$ eV^[113]. Our GW-BSE predicts these states at $\epsilon_{B_{3u}}^{GW BSE} = 3.95$ eV and $\epsilon_{Au}^{GW BSE} = 5.25$ eV. This means that GW-BSE tends to overestimate the transition energies for this system slightly.

The next important step is to investigate the behavior of the PES along the coupling mode, through the conical intersection, which is shown in figure 3.28.

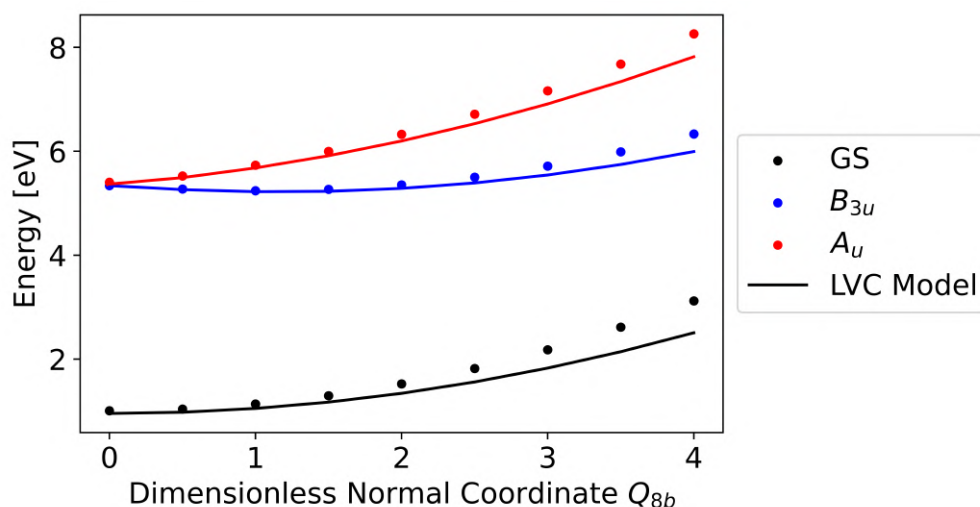


Figure 3.28: PES of the lowest three singlet states along the coupling mode Q_{8b} , starting at the conical intersection. We observe a decent alignment of the LVC Model with the single-point GW-BSE calculations. Significant discrepancies can only be witnessed beyond displacements of about 2.5, which already corresponds to an energy difference of approximately 1 eV for the groundstate and relative to the position of the conical intersection.

We observe a good alignment of the LVC model with the GW-BSE transition energies for small displacement. However, for larger displacement, the results are not as ideal as those of the tuning mode. The two PESs show a mismatch of approximately 0.4 eV for very large displacements at 4. However, this is an acceptable result, as small displacements already cover a large energy range and consequently many vibrational states. Once again one can compare the obtained λ parameter with the ones found in the literature. CASSCF calculations estimate that $|\lambda_{B_{3g}}^{ref}| = 0.205$ eV.^[109] In a similar way, our GW-BSE-LVC model estimates the coupling coefficient to be $|\lambda_{B_{3g}}^{GW BSE}| = 0.228$ eV, which is again a discrepancy of approximately 10%. We conclude from this investigation that the GW-BSE-LVC model yields decent results for the PES, especially if the PES does not show strong anharmonic characteristics. Additionally, the GW-BSE yields PES that show a decent alignment with more expensive calculations, such as CASSCF, for such small systems. In the last step, we will have to investigate whether this behavior is also true for larger systems where states of different multiplicities come into play.

3.7 Structure of the Potential Energy Surface and IVC Parameterization for a closed-shell Fe Complex

As we have seen throughout this work, the spectra obtained by GW-BSE appear to be a more accurate description of the molecular system in comparison to DFT. We have seen that GW-BSE offers the enormous advantage of providing a balanced description of charge transfer and regular states. In addition, the evGW-BSE framework removes the dependence on the exchange-correlation functional, used for the starting molecular orbitals, to a certain degree. The remaining unanswered question is whether the PESs obtained by GW-BSE are accurate as well, in particular for larger systems such as a transition metal complex. For a small system, consisting of singlet states, we have seen in the previous chapter that this is the case particularly if the PES shows a strong harmonic behavior. Now we want to investigate a large iron metal complex called $[\text{Fe}(\text{cpmp})_2]^{2+}$ (cpmp = 6,2''-carboxypyridyl-2,2'-methylamine-pyridyl-pyridine). This complex has been studied using TD-DFT with a range-separated functional, which is why we can easily compare the obtained parameters with each other.^[114] The geometry of the system is shown in figure 3.29.

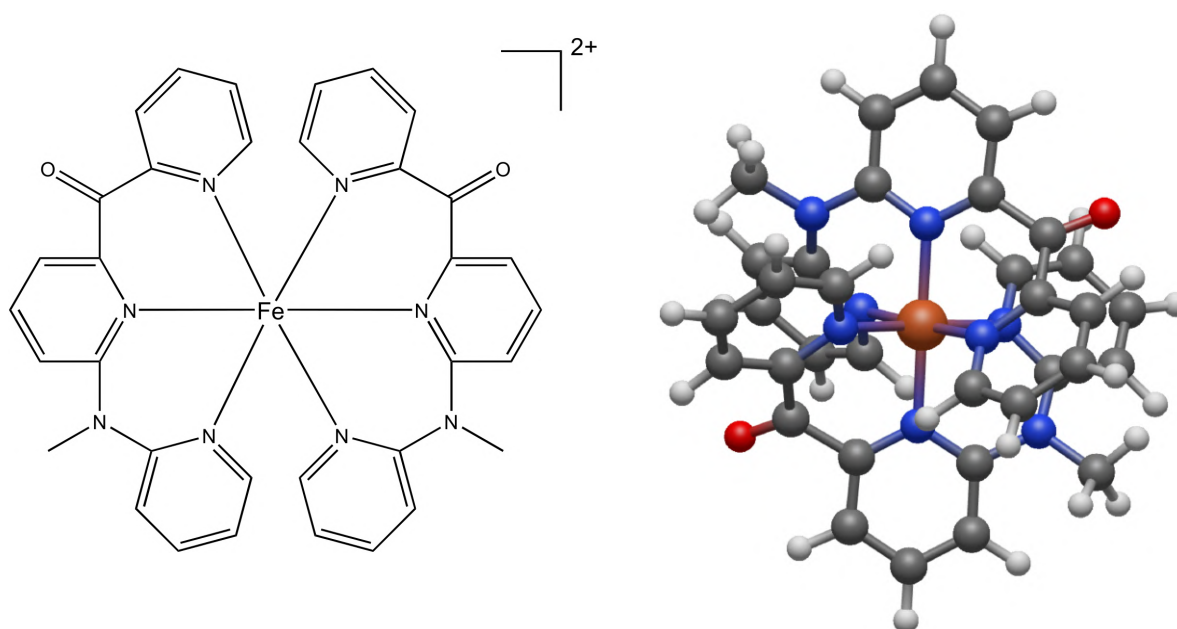


Figure 3.29: Structure of $[\text{Fe}(\text{cpmp})_2]^{2+}$ along with its 3D geometry. We will use the newly developed interface between Turbomole and Sharc to perform an IVC parameterization of the PES. The required SOC parameters will also be calculated using the methods presented earlier in this work.

We used a DFT starting point with the LC-BLYP functional for this system. The parameters, such as $\alpha = 0.2$, $\beta = 0.8$, and $\omega = 0.08$, for this range-separated functional were obtained from the literature.^[114] All ground state properties are obtained through this method, particularly the equilibrium geometry and molecular orbitals for the GW cycle. Initially, we attempted to perform calculations for a def2-TZVP basis, however because of the high computational cost we will opt for a def2-SVP basis set for the ligands and mix them with a def2-TZVP basis set for the central iron atom to better describe the 3d orbitals. The geometry optimization was performed in the C_2 point group.

As a first investigation, we computed the spectra to ensure that the GW-BSE framework yields the correct ordering of excited states compared to the DFT case. We solved

Hedin's equations self-consistently using the evGW scheme with contour deformation techniques. The correlation part of the self-energy operator was calculated for all molecular orbitals in the range [140,194]. The Tamm-Dancoff approximation was taken into account. We will compare them to spectra obtained through TD-DFT. Firstly, we will perform computations for the above-mentioned mixed basis set, composed of def2-SVP and def2-TZVP basis functions. After that, we compared the obtained results to the spectra obtained using only the def2-TZVP basis set for all atoms to investigate the validity of using a smaller basis set. Based on the literature, we expect that increasing the initial exact HF exchange (by raising the α parameter) will cause the MC states to drop in energy and the MLCT states to rise.^[114] Therefore, we tested three sets of parameters, in particular ($\alpha = 0, \omega = 0.14$), ($\alpha = 0.15, \omega = 0.09$) and ($\alpha = 0.2, \omega = 0.08$). The calculated spectra are shown in figure 3.30 and obtained by broadening the vertical transitions by a Lorentzian function with a full-width-half-maximum of 0.25 eV.

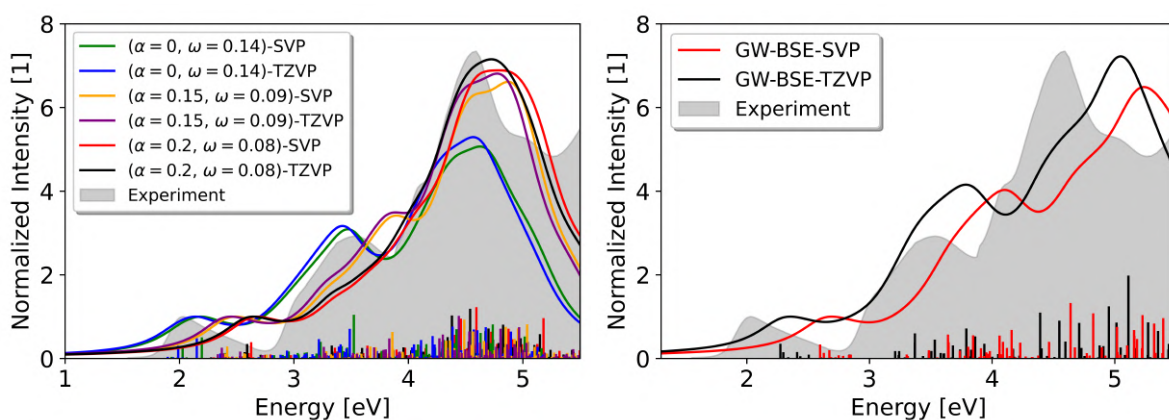


Figure 3.30: Spectra obtained using DFT (left figure) and GW-BSE (right figure). In both cases, we used the LC-BLYP functional, however, in the left figure we also made changes to the tuning parameters α and ω . Both calculations are also performed for two different basis sets. TZVP refers to the def2-TZVP basis set, whereas SVP stands for a mix of def2-SVP for the ligand and def2-TZVP for the central iron atom. The starting point for the GW-BSE calculation was a DFT LC-BLYP($\alpha = 0.2$) calculation. In the experimental spectrum, acetonitrile was used as a solvent, whereas all calculations were performed in vacuum. An increase of the α parameters leads to a worse description of the spectrum when compared to the experimental one. The GW-BSE method appears to provide a reasonable alignment with the experimental spectrum, comparable in quality to that of DFT. However, it seems to be more sensitive to changes in the basis set compared to DFT.

As expected we observe that the obtained spectra depend heavily on the set of tuning parameters in the DFT case. An increase of the exact HF exchange, for the range of small electron-electron distances, in the functional leads to the entire spectrum being shifted toward higher energies. Furthermore, also the oscillator strength is impacted, as the second absorption peak around 3.4 eV is lowered. Overall we can say that the alignment with the experiment worsens if the amount of exact exchange is increased. In the GW-BSE case, we observe that the GW-BSE spectra appear to be highly susceptible to a change of the basis set. In particular, for the mixed def2-SVP/def2-TZVP basis set we observe a significant worsening of the alignment of the spectrum with experimental values. However, in the case of the full def2-TZVP basis set, the produced spectra align better with the experiment when compared to the DFT calculation involving $\alpha = 0.2$.

Besides the alignment with the experimental absorption spectrum, the essential factor will although be the correct ordering of the excited states. Because of this, we performed an

analysis of the transition density matrix for all calculations using the mixed def2-SVP and def2-TZVP basis set for the DFT calculations as they appear to not vary drastically. The same analysis has also been performed for the GW-BSE calculation, however for the full def2-TZVP basis set. The obtained decompositions are shown in figure 3.31 and 3.32.

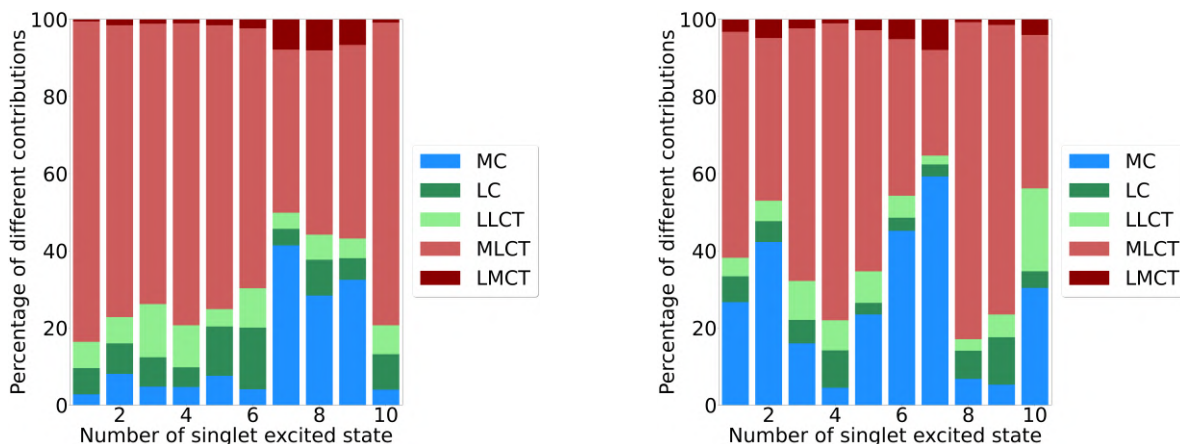


Figure 3.31: Analysis of the transition density matrix on the DFT level of theory. The left figure shows the charge transfer character of the lowest 10 singlet excited states using an LC-BLYP($\alpha = 0$, $\omega = 0.14$) functional, whereas the right figure shows the same analysis for the LC-BLYP($\alpha = 0.15$, $\omega = 0.09$) functional. In both cases, the mixed def2-SVP and def2-TZVP basis set has been used. One can observe that a change of functional has a strong impact on the ordering of excited states, as an increase of α leads to the MC states being shifted downwards in energy.

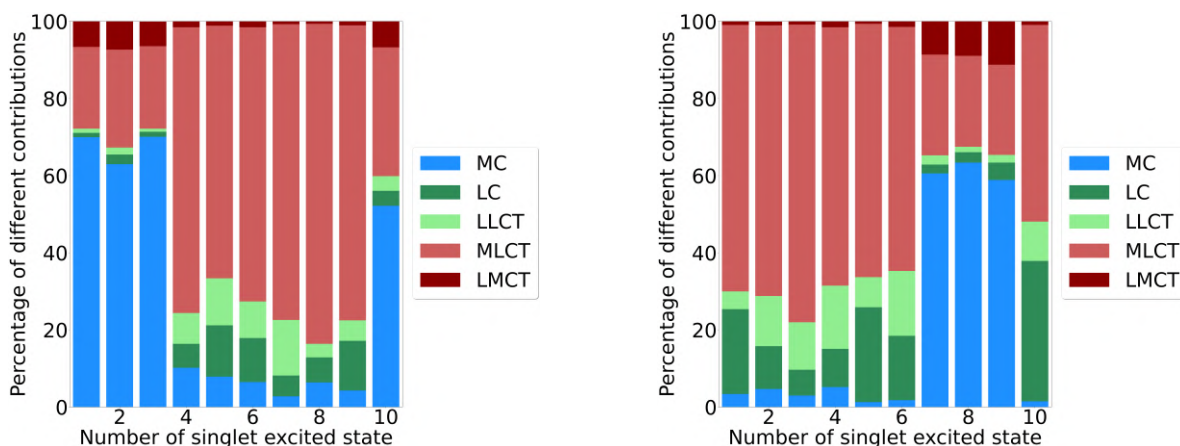


Figure 3.32: Analysis of the transition density matrix on the DFT (left figure) and GW-BSE (right figure) levels of theory for the 10 lowest singlet excited states. The mixed def2-SVP, def2-TZVP basis set has been used for the DFT calculation, which also relied on an LC-BLYP($\alpha = 0.2$, $\omega = 0.08$) functional. In the GW-BSE case, a full def2-TZVP basis set was employed. We observe that further increase of the exact HF exchange leads to the MC states becoming the lowest excited state. The GW-BSE calculation however yields the expected ordering of states with the lowest excited singlet states having a dominant MLCT character.

Based on these figures it is clear that an increase in the exact HF exchange leads to the MC states being shifted down in energy and eventually surpassing the MLCT states becoming the lowest singlet excited states. We expect however the lowest singlet excited state to have a dominant MLCT character, whereas the MC states are the lowest triplet excited states. We can conclude that the GW-BSE yields the correct ordering in the prior case, whereas the DFT

calculations depend on the tuning parameters. However, to investigate the latter aspect we also analyzed the transition density matrix to identify the charge transfer character of the lowest triplet states. This has been done using the singlet equilibrium geometry and using the same parameters and basis sets as in the singlet case. The results are shown in figure 3.33 and 3.34

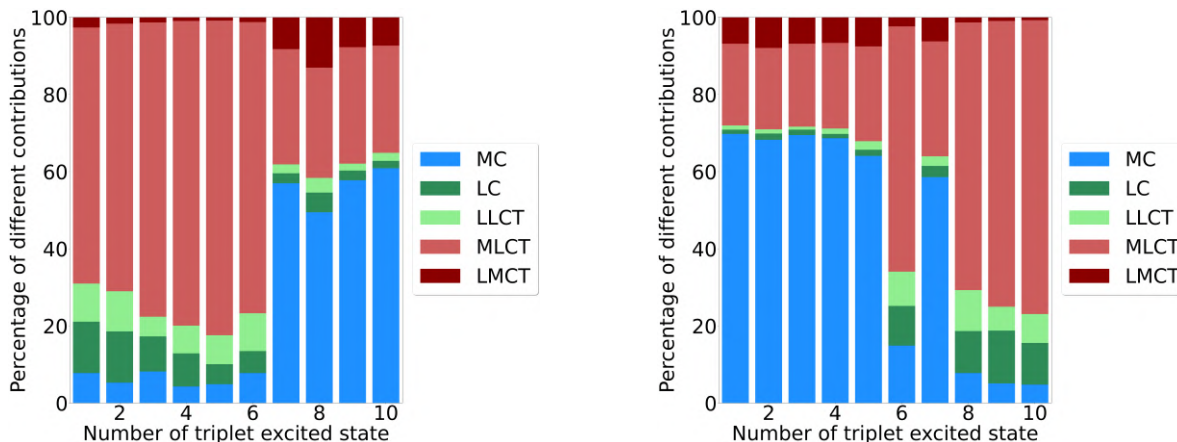


Figure 3.33: Analysis of the transition density matrix for the 10 lowest triplet excited states in the singlet DFT equilibrium geometry. The left figure shows the analysis for the LC-BLYP($\alpha = 0$, $\omega = 0.14$) functional, while the right figure shows the analysis for the LC-BLYP($\alpha = 0.15$, $\omega = 0.09$). Both calculations have been performed with the mixed def2-SVP, def2-TZVP basis set. We see that an initial exact HF exchange is required, as the otherwise lowest excited states have a dominant MLCT character.

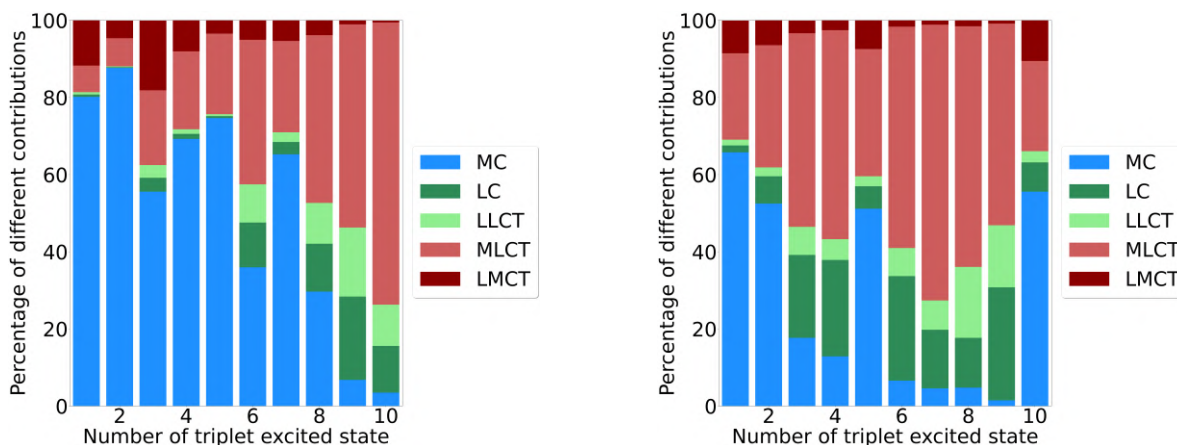


Figure 3.34: Analysis of the transition density matrix for both the DFT LC-BLYP($\alpha = 0.2$, $\omega = 0.08$) (left figure) and GW-BSE calculations in the singlet DFT equilibrium geometry. The DFT calculation has been performed using the mixed def2-SVP, def2-TZVP basis set, whereas the GW-BSE used only def2-TZVP basis functions. We observe that both levels of theory yield the correct ordering of states in the triplet case with the lowest excited states having a strong MC character.

A change of α has a similar effect for the triplet as for the singlet states. A higher exact exchange leads to a lowering of the MC state's energy. As discussed earlier, this step is required as the original LC-BLYP($\alpha = 0$, $\omega = 0.14$) yields the incorrect ordering of states. In the GW-BSE case, we can see that the expected ordering is obtained with the MC states being located in the low energy range. This analysis hints once more at the fact that the GW-BSE approach yields a more correct ordering of states, unlike the DFT framework where a change

in the functional leads to strong differences in the ordering and tuning of the parameters α and ω is necessary to reproduce experimental values. This appears to be a strong advantage of the GW-BSE framework and aligns well with our findings from chapter 3.4 where we already observed a similar behavior. The difference from our previous findings is that the GW-BSE predicts the lowest excited triplet state to have a dominant MC character in the singlet equilibrium geometry, whereas before we performed the analysis in the triplet one. In the example from chapter 3.4 this was necessary since GW-BSE predicted the lowest excited triplet state in the singlet geometry to have a dominant MLCT character. Therefore this is another observation that also the PES of chemically similar systems can vary strongly. In addition to that, the GW-BSE results appear to be more susceptible to the used basis, which may become an issue due to the higher computational cost that originates from solving Hedin's equations self-consistently.

With the previously obtained knowledge we now performed an LVC parameterization of the molecular Hamiltonian. Due to the large differences, we observed in the GW-BSE spectra, we decided to opt for a def2-TZVP basis set. However, this decision will perhaps require revision, once we attempt to extend this model to all normal modes, as it comes with a significant increase in computational cost. The results for the same parametrizations using the smaller mixed def2-SVP basis set can be found in the appendix 5.10. For this model, we used a displacement factor of 0.05 and discarded the first 49 core molecular orbitals to calculate the wavefunction overlaps. As discussed in the previous chapters, SOC matrix elements were obtained through second-order perturbation theory. Our LVC model included the lowest 10 singlet and 14 triplet states. Figure 3.35 shows the quality of the LVC model along the 25. normal mode with a frequency of 186.24 cm^{-1} for both the DFT LC-BLYP ($\alpha = 0.2$, $\omega = 0.08$) and the GW-BSE level of theory. The 25. normal mode is of particular interest since it is a breathing mode, meaning it impacts the bond length between the central metal and the ligand.

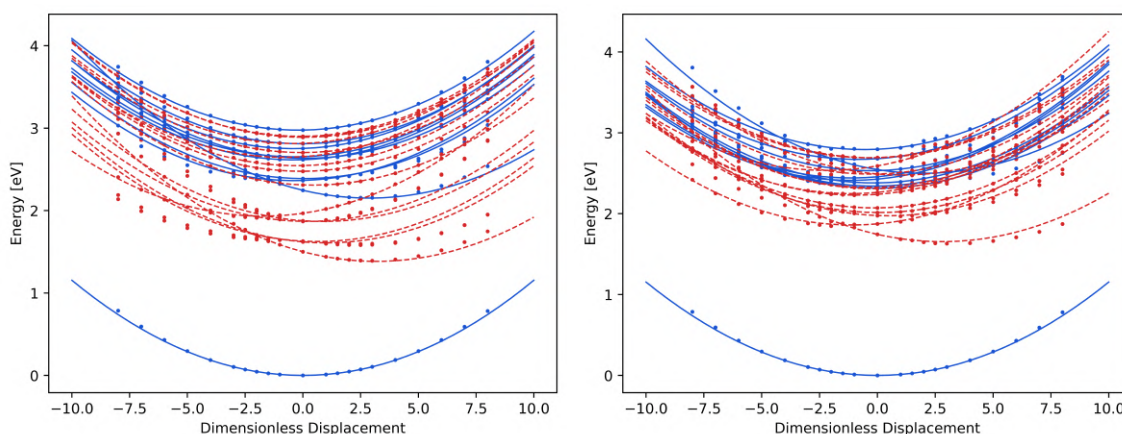


Figure 3.35: The PES in the diabatic representation for the lowest 10 singlet and 14 triplet states along the 25. normal coordinate, which is a breathing mode. The left figure shows the obtained curves using the newly developed interface and DFT with the LC-BLYP functional for $\alpha = 0.2$ and $\omega = 0.08$. The right figure shows the corresponding GW-BSE calculations. Singlet states are shown as solid blue lines, whereas triplet states are dashed red. The dot markers represent single-point calculations at the specified geometries. A positive displacement corresponds to an elongation of the Fe-N bond length.

Figure 3.35 shows the possibility of approximating the PES along a single normal mode for two different levels of theory. We see that the calculated LVC PES decently aligns with the

single-point calculations, especially around the equilibrium geometry, where the PES show strong harmonic characteristics. However, coupling between the states is only included through the off-diagonal elements, so we diagonalized the potential energy to obtain the PES in the adiabatic representation. They are shown in figure 3.36.

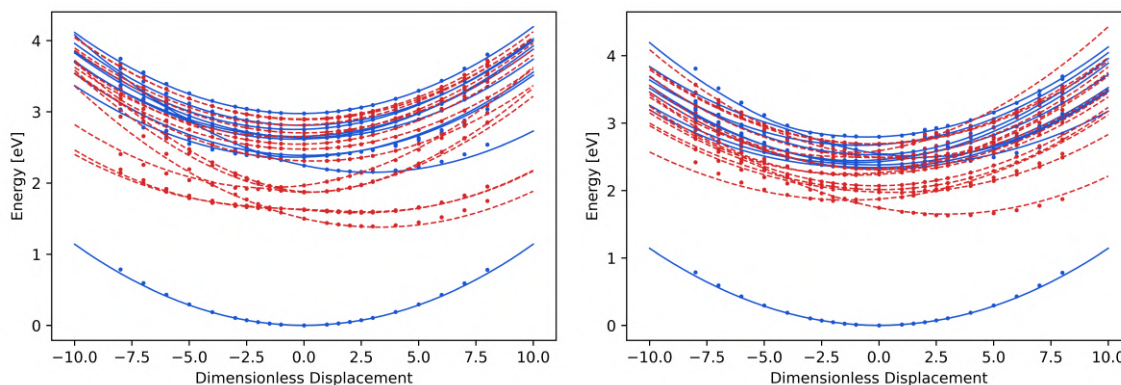


Figure 3.36: The PES in the adiabatic representation for both the DFT (left figure) and GW-BSE (right figure) levels of theory. For both calculations an LC-BLYP($\alpha = 0.2$, $\omega = 0.08$) functional was used. Singlet states are shown as solid blue lines, whereas triplet states are dashed red. The dot markers represent single-point calculations at the specified geometries.

If coupling between the two states is included, we can see that the LVC model is capable of properly approximating the PES. In particular, we observe a good alignment with the single-point calculations for the lowest triplet states, which are usually difficult to properly describe. In both figures, the LVC model yields decent results as long as the displacements become not too large. In the latter case, the anharmonic character of the PES becomes important.

By comparing the two sets of PES, it is clear that both will lead to different dynamics. This is an important result as the obtained spectra in figure 3.30 may lead to the conclusion that both levels of theory yield a similar electronic structure. However, a deeper investigation of the transition density matrix and the full PES shows that this is misleading. We furthermore observe that the harmonic approximation of the PES has merit in this case for this particular mode. Although we cannot generally expect the LVC model to yield an adequate description of the PES. For instance, a fundamental assumption of the LVC model is that normal modes of the molecular system in the excited state do not differ from the ones in the ground states. To test this assumption for future modes, we also performed a geometry optimization in the triplet configurations using the parameters $\alpha = 0.2$ and $\omega = 0.08$ for the LC-BLYP functional and the mixed def2-SVP and def2-TZVP basis sets. The Metal-to-Ligand bond length for both spin states is summarized in table 3.3.

Bond	Singlet (Å)	Triplet (Å)
Fe-N ₁	2.01639	2.15309
Fe-N ₂	2.00389	2.14124
Fe-N ₃	2.00389	2.14124
Fe-N ₄	2.01639	2.15309
Fe-N ₅	1.98361	1.97601
Fe-N ₆	1.98361	1.97601

Table 3.3: Comparison of bond lengths between the singlet and triplet states.

We observe that a change in the spin states leads to the system being stretched along two axes and squeezed along the third. With these geometries we calculated the scalar products between the two sets of obtained normal mode vectors. These results are shown in figure 3.37. If the LVC model is valid for all normal modes, we expect that every single triplet normal mode could be described by a single singlet normal mode, with an overlap of 1, located on the main diagonal, meaning that also the normal mode frequencies do not change.

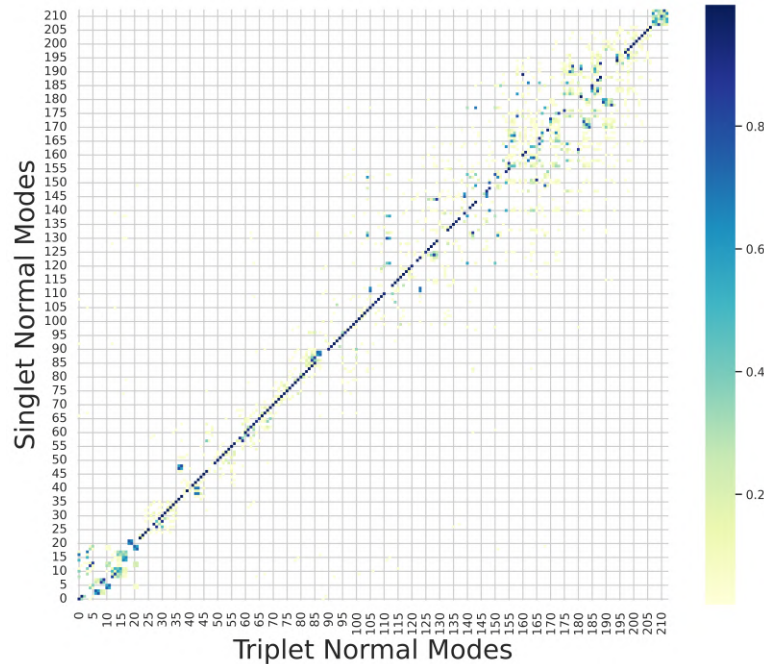


Figure 3.37: Analysis of the scalar products between a set of singlet and triplet normal modes. Each pixel represents the absolute value of the scalar product between two normal mode vectors. A threshold of 0.02 was applied for better illustration. All normal modes are sorted in order of increasing frequency. Many triplet normal modes share a large overlap with their singlet counterparts, indicated by the many pixels on the main diagonal. However, this decomposition becomes less clear, especially for higher frequencies, where a single triplet mode may also be composed of other singlet modes. Since many normal modes are close in energy and can therefore change their index, we swapped entries on the first 20 super- or subdiagonal with the main diagonal if they showed a dominant contribution of more than 0.9.

The decomposition of the triplet normal modes into the singlet ones shows that many normal modes maintain a large share of the corresponding singlet modes. This can be seen by the many pixels located on the main diagonal with a contribution that is close to 1. However, it is also clear that this assumption may not always be correct. Especially for normal modes with higher frequencies, we observe that we obtain entries, that are not located on the main diagonal, either because they swapped positions with neighboring normal modes or are entirely composed of more than one mode. This essentially means that a single triplet mode may be a superposition of more than one singlet mode or that it changes frequency and thus their index, even if the character of the modes remains nearly the same. We attempted to compensate for the latter effect, by swapping entries between the first 20 super- or subdiagonals with the main diagonal if they included a dominant contribution larger than 0.9.

To further estimate the quality of this result, we decided to generate a histogram for all possible values along the main diagonal. Furthermore, we generated a correlation plot to sort them according to their frequency. The results of this additional investigation are shown in figure 3.38.

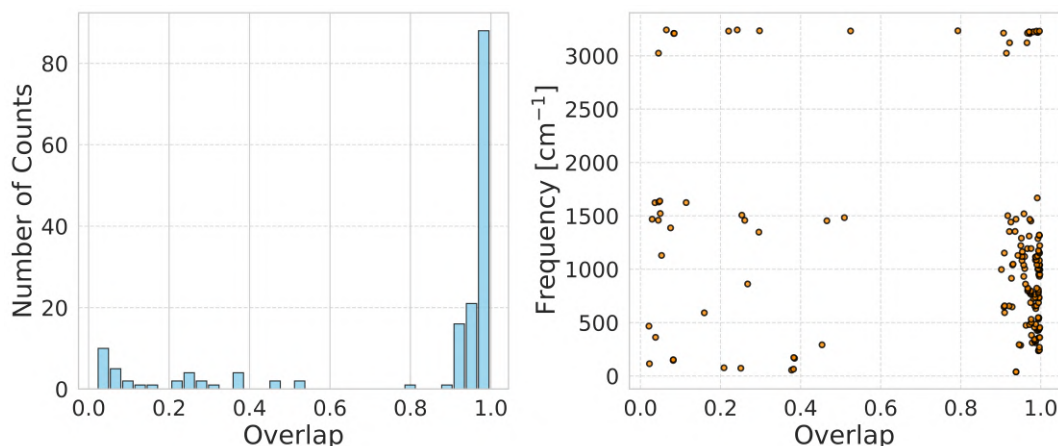


Figure 3.38: Histogram of the obtained overlap values along the main diagonal, alongside the position of each overlap value relative to the singlet normal mode frequencies. We observe that the overlap decreases for frequencies around 1500 cm^{-1} . However, normal modes across the entire spectrum are generally affected.

This analysis shows a similar result as figure 3.37. We see that more than half the normal modes are adequately described by their singlet counterparts. Most of the modes that are a superposition of multiple singlet modes are located around 1500 cm^{-1} , however, there exist normal modes through the entire spectrum, which fall into this category. For these modes we expect a Dushinsky rotation to be necessary to compensate for this effect as the LVC model otherwise will become invalid. ^{[115] [116]}

The last remaining aspect is an investigation of the obtained SOC matrix elements. For this, we calculated both as part of the LVC parametrizations. The results obtained from DFT and GW-BSE calculations are presented in a histogram, in figure 3.39.

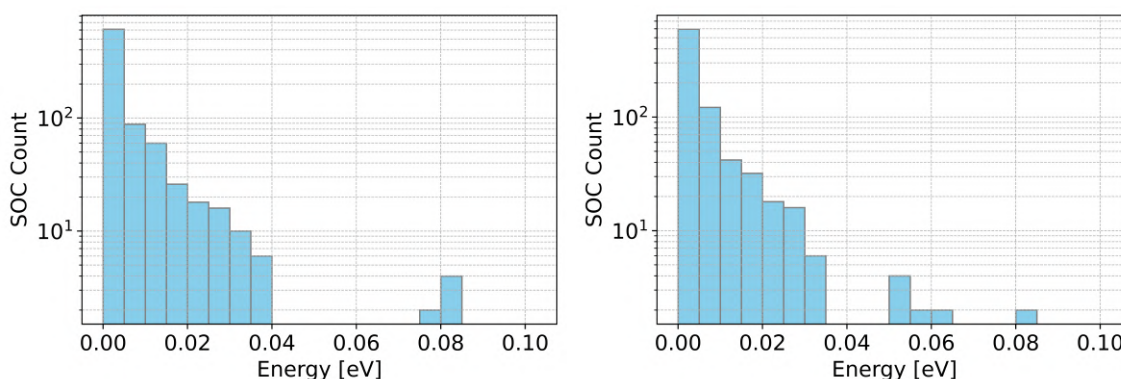


Figure 3.39: Distribution of SOC values for the DFT (left figure) and GW-BSE (right figure) LVC PES. In the low energy limit only small differences between the two distributions are observed. In the DFT case, most SOC matrix elements are smaller than 0.04 eV . In comparison yields SOC matrix elements that reach only 0.03 eV . In both cases, the highest SOC value is located between 0.08 eV and 0.085 eV .

Overall, we observe that the distribution of SOC matrix elements does not strongly change if the response vectors are calculated from GW-BSE and not TD-DFT. The main difference between them can be observed beyond 0.03 eV, with the majority of GW-BSE SOC values appearing below this threshold. In contrast, the DFT values reach 0.04 eV. The highest SOC matrix element can be found between 0.08 eV and 0.085 eV for both levels of theory, however, DFT yields 3 SOC matrix elements in the range whereas GW-BSE only produces a single entry. Furthermore GW-BSE yields entries around 0.06 eV, in contrast to DFT.

4 Conclusion and Outlook

Throughout this work, we have seen that the GW-BSE framework yields an important tool to investigate the electronic structure of transition metal complexes. We observed that it comes with many advantages compared to standard TD-DFT calculations. It offers solutions in areas where other levels of theory lack the required accuracy. In particular, this investigation has shown that the GW-BSE framework offers a balanced description of both charge transfer transitions and all other types of transitions for many systems. This feature is included in the framework directly and does not require separate tuning of the underlying DFT exchange-correlation functional or other parameters. In fact, we have observed that it is possible to reduce almost completely the dependency on the original functional, by solving Hedin's equations self-consistently. Overall, this means that it is possible to achieve a description of excited electronic states that is almost independent of other DFT variables to yield results that do not favor one particular type of transition. Especially the fact that the GW-BSE framework appears to yield the expected ordering of excited states is of particular interest. However, based on our investigations we have also seen that not only the characters of states are described more accurately but also the transition energies and oscillator strengths appear to be better suited to reproduce experimental values when compared to TD-DFT calculations. Other important quantities, such as SOC matrix elements also appear to be sufficiently accurate, which combined with the previous findings motivated the idea of a GW-BSE LVC model for the PES.

Nevertheless, we have also observed limitations of this level of theory. A major drawback is the lack of possibilities to describe ground state properties, such as the equilibrium geometry, the correct spin state, or normal modes. As previously discussed, if properties like these, or if the features of the electronic structure, cannot be adequately described by the initial calculations, the GW-BSE framework shows no improvements to these results. Besides that, the computation of quasiparticle energies, which is required to initialize the Bethe-Salpeter equation, comes with an additional computational cost up to the point that it may become the bottleneck of the entire calculation. In addition, we have observed that GW-BSE calculations are more susceptible to changes to the basis set. It should also be noted that other studies indicate that the GW-BSE formalism underestimates the energy of triplet states.^[117]

Based on these findings, it is clear that the next step will be to perform a full LVC parametrization of the entire PES. We have already observed that the ordering of states and the absorption spectrum appear to align well with the experiment, however, so far we have not been able to extend this to the entire PES. With the LVC parametrization, it will be possible to conduct either classical trajectory-based surface hopping or quantum mechanical wavepacket dynamics simulations. With them, one can gain insight into whether the lifetimes of different electronic states are described correctly or if the expected weaknesses of the GW-BSE framework persist for systems of transition metal complexes. These results may then be compared to experimental transient absorption data to estimate the accuracy of this theory's PES.

5 Appendix

5.1 Equation of Motion

Start with the definition of the Green's Function and its time derivative as given in equation (2.11).

$$iG(1, 2) = \langle N | \hat{\mathcal{T}} \left[\hat{\psi}(1) \hat{\psi}^\dagger(2) \right] | N \rangle \quad (5.1)$$

$$\begin{aligned} i \frac{\partial G(1, 2)}{\partial t_1} &= \frac{\partial \Theta(t_1 - t_2)}{\partial t_1} \langle N | \hat{\psi}(1) \hat{\psi}^\dagger(2) | N \rangle - \frac{\partial \Theta(t_2 - t_1)}{\partial t_1} \langle N | \hat{\psi}^\dagger(2) \hat{\psi}(1) | N \rangle + \\ &+ \langle N | \hat{\mathcal{T}} \left[\frac{\partial \hat{\psi}(1)}{\partial t_1} \hat{\psi}^\dagger(2) \right] | N \rangle \end{aligned} \quad (5.2)$$

with the Hamiltonian

$$\hat{H} = \int dx \hat{\psi}^\dagger(x) h(x) \hat{\psi}(x) + \frac{1}{2} \iint dx_1 dx_2 \hat{\psi}^\dagger(x_1) \hat{\psi}^\dagger(x_2) v(x_1 - x_2) \hat{\psi}(x_2) \hat{\psi}(x_1). \quad (5.3)$$

We conclude based on the Heisenberg picture that

$$i \frac{\partial \hat{\psi}(1)}{\partial t_1} = \left[\hat{\psi}(1), \hat{H} \right] = \left[e^{i\hat{H}t_1} \hat{\psi}(x_1) e^{-i\hat{H}t_1}, \hat{H} \right] = e^{i\hat{H}t_1} \left[\hat{\psi}(x_1), \hat{H} \right] e^{-i\hat{H}t_1} \quad (5.4)$$

because \hat{H} commutes with itself.

Now, we search for the derivative of $\hat{\psi}(x)$, given by the commutator with the Hamiltonian

$$\begin{aligned} \left[\hat{\psi}(x_1), \hat{H} \right] &= \left[\hat{\psi}(x_1), \int dx \hat{\psi}^\dagger(x) h(x) \hat{\psi}(x) \right. \\ &+ \left. \frac{1}{2} \iint dx_1 dx_2 \hat{\psi}^\dagger(x_1) \hat{\psi}^\dagger(x_2) v(x_1 - x_2) \hat{\psi}(x_2) \hat{\psi}(x_1) \right] \\ &= \underbrace{\left[\hat{\psi}(x_1), \int dx \hat{\psi}^\dagger(x) h(x) \hat{\psi}(x) \right]}_{=I} \\ &+ \underbrace{\frac{1}{2} \left[\hat{\psi}(x_1), \iint dx_2 dx_3 \hat{\psi}^\dagger(x_2) \hat{\psi}^\dagger(x_3) v(x_2 - x_3) \hat{\psi}(x_3) \hat{\psi}(x_2) \right]}_{=II}. \end{aligned} \quad (5.5)$$

Now focus on each part separately and use the anti-commutator relation

$$\left\{ \hat{\psi}(x), \hat{\psi}^\dagger(x') \right\} = \delta(x - x').$$

$$\begin{aligned} I &= \int dx \left(\delta(x - x_1) - \hat{\psi}^\dagger(x) \hat{\psi}(x_1) \right) h(x) \hat{\psi}(x) - \int dx \hat{\psi}^\dagger(x) h(x) \hat{\psi}(x) \hat{\psi}(x_1) \\ &= h(x_1) \hat{\psi}(x_1) + \int dx \hat{\psi}^\dagger(x) h(x) \hat{\psi}(x) \hat{\psi}(x_1) - \int dx \hat{\psi}^\dagger(x) h(x) \hat{\psi}(x) \hat{\psi}(x_1) \\ &= h(x_1) \hat{\psi}(x_1) \end{aligned} \quad (5.6)$$

Now work on the second term and use the anti-commutator relation again.

$$\begin{aligned}
2 \cdot II &= \iint dx_2 dx_3 v(x_2 - x_3) \left[\hat{\psi}(x_1) \hat{\psi}^\dagger(x_2) \hat{\psi}^\dagger(x_3) \hat{\psi}(x_3) \hat{\psi}(x_2) - \hat{\psi}^\dagger(x_2) \hat{\psi}^\dagger(x_3) \hat{\psi}(x_3) \hat{\psi}(x_2) \hat{\psi}(x_1) \right] \\
&= \iint dx_2 dx_3 v(x_2 - x_3) \left[\left(\delta(x_1 - x_2) - \hat{\psi}^\dagger(x_2) \hat{\psi}(x_1) \right) \hat{\psi}^\dagger(x_3) \hat{\psi}(x_3) \hat{\psi}(x_2) - \hat{\psi}^\dagger(x_2) \hat{\psi}^\dagger(x_3) \hat{\psi}(x_3) \hat{\psi}(x_2) \hat{\psi}(x_1) \right] \\
&= \int dx_3 v(x_1 - x_3) \hat{\psi}^\dagger(x_3) \hat{\psi}(x_3) \hat{\psi}(x_1) - \iint dx_2 dx_3 v(x_2 - x_3) \hat{\psi}^\dagger(x_2) \hat{\psi}(x_1) \hat{\psi}^\dagger(x_3) \hat{\psi}(x_3) \hat{\psi}(x_2) \\
&\quad - \iint dx_2 dx_3 v(x_2 - x_3) \hat{\psi}^\dagger(x_2) \hat{\psi}^\dagger(x_3) \hat{\psi}(x_3) \hat{\psi}(x_2) \hat{\psi}(x_1) \\
&= \int dx_3 v(x_1 - x_3) \hat{\psi}^\dagger(x_3) \hat{\psi}(x_3) \hat{\psi}(x_1) \\
&\quad - \iint dx_2 dx_3 v(x_2 - x_3) \hat{\psi}^\dagger(x_2) \left(\delta(x_1 - x_3) - \hat{\psi}(x_3) \hat{\psi}^\dagger(x_1) \right) \hat{\psi}(x_3) \hat{\psi}(x_2) \\
&\quad - \iint dx_2 dx_3 v(x_2 - x_3) \hat{\psi}^\dagger(x_2) \hat{\psi}^\dagger(x_3) \hat{\psi}(x_3) \hat{\psi}(x_2) \hat{\psi}(x_1) \\
&= \int dx_3 v(x_1 - x_3) \hat{\psi}^\dagger(x_3) \hat{\psi}(x_3) \hat{\psi}(x_1) - \int dx_2 v(x_2 - x_1) \hat{\psi}^\dagger(x_2) \hat{\psi}(x_3) \hat{\psi}(x_2) \\
&\quad - \iint dx_2 dx_3 v(x_2 - x_3) \hat{\psi}^\dagger(x_2) \hat{\psi}(x_3) \hat{\psi}^\dagger(x_1) \hat{\psi}(x_3) \hat{\psi}(x_2) \\
&\quad - \iint dx_2 dx_3 v(x_2 - x_3) \hat{\psi}^\dagger(x_2) \hat{\psi}^\dagger(x_3) \hat{\psi}(x_3) \hat{\psi}(x_2) \hat{\psi}(x_1)
\end{aligned} \tag{5.7}$$

By renaming x_3 to x_2 in the first term and using $v(x - x') = v(x' - x)$ one can combine the two. The last two terms cancel out to 0.

$$II = \int dx_2 v(x_1 - x_2) \hat{\psi}^\dagger(x_2) \hat{\psi}(x_2) \hat{\psi}(x_1) \tag{5.8}$$

Therefore one concludes

$$\begin{aligned}
&e^{i\hat{H}t_1} \left[\hat{\psi}(x_1), \hat{H} \right] e^{-i\hat{H}t_1} \\
&= e^{i\hat{H}t_1} \left[h(x_1) \hat{\psi}(x_1) + \int dx_2 v(x_1 - x_2) \hat{\psi}^\dagger(x_2) \hat{\psi}(x_2) \hat{\psi}(x_1) \right] e^{-i\hat{H}t_1} = i \frac{\partial \hat{\psi}(1)}{\partial t_1}.
\end{aligned} \tag{5.9}$$

Inserting this into (5.2) leads to

$$\begin{aligned}
i \frac{\partial G(1, 2)}{\partial t_1} &= \delta(t_1 - t_2) \langle N | \hat{\psi}(1) \hat{\psi}^\dagger(2) + \hat{\psi}^\dagger(2) \hat{\psi}(1) | N \rangle \\
&\quad - i \langle N | \hat{\mathcal{T}} \left[h(x_1) \hat{\psi}(1) \hat{\psi}^\dagger(2) + \int d3 \hat{\psi}^\dagger(3^+) v(1, 3) \hat{\psi}(3) \hat{\psi}(1) \hat{\psi}^\dagger(2) \right] | N \rangle.
\end{aligned} \tag{5.10}$$

where we wrote $d1 = dx_1 dt_1$ and $v(1, 2) = v(x_1 - x_2) \delta(t_1, t_2)$. The 3^+ refers to an infinitesimal shift to a later time, such the time ordering operator produces the correct ordering, like in equation (5.9).

The first term is the commutator relation, which yields a delta distribution.

$$\begin{aligned}
i \frac{\partial G(1, 2)}{\partial t_1} &= \delta(2, 3) - ih(x_1) \langle N | \hat{\mathcal{T}} \left[\hat{\psi}(1) \hat{\psi}^\dagger(2) \right] | N \rangle \\
&\quad - i \int d3 v(1, 3) i^2 G_2(1, 3; 2, 3^+)
\end{aligned} \tag{5.11}$$

with the definition of two-particle Green's Function

$$i^2 G_2(1, 3; 2, 3^+) = \langle N | \hat{\mathcal{T}} \left[\hat{\psi}(1) \hat{\psi}^\dagger(3^+) \hat{\psi}(3) \hat{\psi}^\dagger(2) \right] | N \rangle \quad (5.12)$$

This leads to the equation of motion

$$\left(i \frac{\partial}{\partial t_1} - h(1) \right) G(1, 2) + i \int d^3v(1, 3) G_2(1, 3; 2, 3^+) = \delta(1, 2). \quad (5.13)$$

We define the mass operator like this

$$\int d^3M(1, 3) G(3, 2) = -i \int d^3v(1, 3) G_2(1, 3; 2, 3^+) \quad (5.14)$$

which yields the final equation of motion in the form

$$\left(i \frac{\partial}{\partial t_1} - h(1) \right) G(1, 2) - \int d^3M(1, 3) G(3, 2) = \delta(1, 2). \quad (5.15)$$

5.2 Derivative of Field Operators

The goal is to investigate the following expression, where we dropped the operator notation

$$A = \frac{\delta}{\delta w(\mathbf{3})} \left[\hat{U}(T_0, -T_0) \left(\underbrace{\Theta(t_1 - t_2)\psi(1)\psi^\dagger(2)}_{=A^1} - \underbrace{\Theta(t_2 - t_1)\psi^\dagger(2)\psi(1)}_{=A^2} \right) \right]. \quad (5.16)$$

Let us take a look at the first term

$$\begin{aligned} A^1 &= \frac{\delta}{\delta w(\mathbf{3})} \left[\Theta(t_1 - t_2) \hat{U}(T_0, -T_0) \hat{U}(-T_0, t_1) \psi(x_1) \hat{U}(t_1, t_2) \psi^\dagger(x_2) \hat{U}(t_2, -T_0) \right] \\ &= \Theta(t_1 - t_2) \frac{\delta}{\delta w(\mathbf{3})} \left[\hat{U}(T_0, t_1) \psi(x_1) \hat{U}(t_1, t_2) \psi(x_2) \hat{U}(t_2, -T_0) \right]. \end{aligned} \quad (5.17)$$

Now perform product rule

$$\begin{aligned} A^1 &= \Theta(t_1 - t_2) \left[\frac{\delta \hat{U}(T_0, t_1)}{\delta w(\mathbf{3})} \psi(x_1) \hat{U}(t_1, t_2) \psi^\dagger(x_2) \hat{U}(t_2, -T_0) \right. \\ &\quad + \hat{U}(-T_0, t_1) \psi(x_1) \frac{\delta \hat{U}(t_1, t_2)}{\delta w(\mathbf{3})} \psi^\dagger(x_2) \hat{U}(t_2, -T_0) \\ &\quad \left. + \hat{U}(T_0, t_1) \psi(x_1) \hat{U}(t_1, t_2) \psi^\dagger(x_2) \frac{\delta \hat{U}(t_2, -T_0)}{\delta w(\mathbf{3})} \right] \end{aligned} \quad (5.18)$$

and insert equation (2.28) with the assumption $\hat{U}_0(t, t') = \hat{U}(t, t')$. This is justified because the difference between these two quantities is linear in $w(x, t)$, which we will set to 0 at the end of the derivation.

$$\begin{aligned} A^1 &= -i\Theta(t_1 - t_2) \left[\hat{U}(T_0, t_3) \rho(x_3) \hat{U}(t_3, t_1) \psi(x_1) \hat{U}(t_1, t_2) \psi^\dagger(x_2) \hat{U}(t_2, -T_0) \right. \\ &\quad + \hat{U}(T_0, t_1) \psi(x_1) \hat{U}(t_1, t_3) \rho(x_3) \hat{U}(t_3, t_2) \psi^\dagger(x_2) \hat{U}(t_2, -T_0) \\ &\quad \left. + \hat{U}(T_0, t_1) \psi(x_1) \hat{U}(t_1, t_2) \psi^\dagger(x_2) \hat{U}(t_2, t_3) \rho(x_3) \hat{U}(t_3, -T_0) \right] \\ &= -i\Theta(t_1 - t_2) \hat{U}(T_0, -T_0) \left[\rho(\mathbf{3})\psi(1)\psi^\dagger(2) + \psi(1)\rho(\mathbf{3})\psi^\dagger(2) + \psi(1)\psi^\dagger(2)\rho(\mathbf{3}) \right] \end{aligned} \quad (5.19)$$

Combing this with the second term, which can be treated in the same way, will lead to the final result

$$A = -i\hat{U}(T_0, -T_0) \hat{\mathcal{T}} \left(\hat{\rho}(\mathbf{3}) \hat{\psi}(1) \hat{\psi}^\dagger(2) \right). \quad (5.20)$$

5.3 Separation of the Mass Operator

The mass operator was defined in equation 2.14 as

$$\int d3M(1, 3)G(3, 2) = -i \int d3v(1, 3)G_2(1, 3; 2, 3^+). \quad (5.21)$$

In appendix 5.6 it is shown that the two-particle Green's Functions can be obtained by the following expression

$$G_2(1, 3; 2, 3^+) = G(3, 3^+)G(1, 2) - \frac{\delta G(1, 2)}{\delta w(3)}. \quad (5.22)$$

Inserting this into equation (5.21) will lead to

$$\int d3M(1, 3)G(3, 2) = -i \int d3v(1, 3) \left[G(3, 3^+)G(1, 2) - \frac{\delta G(1, 2)}{\delta w(3)} \right]. \quad (5.23)$$

Now multiply from the left-hand side with $G^{-1}(2, 4)$ and integrate both sides over 2.

$$\begin{aligned} \iint d2d3M(1, 3)G(3, 2)G^{-1}(2, 4) &= \int d3M(1, 3)\delta(3, 4) \\ &= M(1, 4) \\ &= -i \int d2d3v(1, 3) \left[G(3, 3^+)G(1, 2) - \frac{\delta G(1, 2)}{\delta w(3)} \right] G^{-1}(2, 4) \\ &= -i \int d2d3v(1, 3)G(3, 3^+)G(1, 2)G^{-1}(2, 4) + i \int d2d3v(1, 3)\frac{\delta G(1, 2)}{\delta w(3)}G^{-1}(2, 4) \\ &= -i \int d3v(1, 3)G(3, 3^+)\delta(1, 4) + i \int d2d3v(1, 3)\frac{\delta G(1, 2)}{\delta w(3)}G^{-1}(2, 4) \\ &= \underbrace{V(1)\delta(1, 4)}_{=V(1,4)} + i \underbrace{\int d2d3v(1, 3)\frac{\delta G(1, 2)}{\delta w(3)}G^{-1}(2, 4)}_{=\Sigma(1,4)} \\ &= V(1, 4) + \Sigma(1, 4) \end{aligned} \quad (5.24)$$

Here, the Hartree potential $V(1)$ and the self-energy operator $\Sigma(1, 4)$ have been introduced. We will continue investigating the latter by renaming 4 to 2.

$$\Sigma(1, 2) = i \int d3d4v(1, 3)\frac{\delta G(1, 4)}{\delta w(3)}G^{-1}(4, 2) \quad (5.25)$$

Multiplying from the right-hand side with $G(2, 5)$ and integrating over 2 leads to

$$\begin{aligned} \int d2\Sigma(1, 2)G(2, 5) &= i \iiint d2d3d4v(1, 3)\frac{\delta G(1, 4)}{\delta w(3)}G^{-1}(4, 2)G(2, 5) \\ &= i \iint d3d4v(1, 3)\frac{\delta G(1, 4)}{\delta w(3)}\delta(4, 5) \\ &= i \int d3v(1, 3)\frac{\delta G(1, 5)}{\delta w(3)} \end{aligned} \quad (5.26)$$

This leads to the following expression after renaming 5 to 4.

$$\int d2\Sigma(1, 2)G(2, 4) = i \int d3v(1, 3)\frac{\delta G(1, 4)}{\delta w(3)} \quad (5.27)$$

This expression can be inserted into equation (2.32) to obtain equation (2.36).
Now one can insert equation (2.35) into equation (5.25).

$$\begin{aligned}
\Sigma(1, 2) &= i \int d3d4v(1, 3) \frac{\delta G(1, 4)}{\delta w(3)} G^{-1}(4, 2) \\
&= -i \iint d3d4v(1, 3) \left[\iint d5d6G(1, 5) \frac{\delta G^{-1}(5, 6)}{\delta w(3)} G(6, 4) \right] G^{-1}(4, 2) \\
&= -i \iiint d3d5d6v(1, 3) G(1, 5) \frac{\delta G^{-1}(5, 6)}{\delta w(3)} \delta(6, 2) \\
&= -i \iint d3d5v(1, 3) G(1, 5) \frac{\delta G^{-1}(5, 2)}{\delta w(3)} \\
&= -i \iint d3d4v(1, 3) G(1, 4) \frac{\delta G^{-1}(4, 2)}{\delta w(3)}
\end{aligned} \tag{5.28}$$

In the last line, 5 was renamed to 4. This last step is equation (2.38).

5.4 Derivation of the screened Coulomb Potential

Start with the definition of W

$$W(1, 2) = \int v(1, 3) \frac{\delta V(2)}{\delta w(3)} d3 \quad (5.29)$$

where V is given as

$$\begin{aligned} \frac{\delta}{\delta w(3)} V(1) &= \frac{\delta}{\delta w(3)} \left[w(1) - i \int d3 v(1, 3) G(3, 3^+) \right] = \frac{\delta w(1)}{\delta w(3)} - i \int d3 v(1, 3) \frac{\delta G(3, 3^+)}{\delta w(3)} \\ &= \delta(1, 3) + i \int d3 d4 d5 v(1, 3) G(3, 4) \frac{G^{-1}(4, 5)}{\delta w(3)} G(5, 3). \end{aligned} \quad (5.30)$$

This will lead to

$$\begin{aligned} W(1, 2) &= \int d3 v(1, 3) \left[\delta(2, 3) + i \int d4 d5 d6 v(2, 4) G(4, 5) \frac{G^{-1}(5, 6)}{\delta w(3)} G(6, 4) \right] \\ &= v(1, 2) + i \int d3 d4 d5 d6 v(1, 3) v(2, 4) G(4, 5) \frac{\delta G^{-1}(5, 6)}{\delta w(3)} G(6, 4) \\ &= v(1, 2) + i \int d3 d4 d5 d6 v(1, 3) v(2, 4) G(4, 5) \int d7 \frac{\delta V(7)}{\delta w(3)} \frac{\delta G^{-1}(5, 6)}{\delta V(7)} G(6, 4) \\ &= v(1, 2) + i \int d3 d4 d5 d6 v(2, 4) G(4, 5) \int d7 v(1, 3) \frac{\delta V(7)}{\delta w(3)} \frac{\delta G^{-1}(5, 6)}{\delta V(7)} G(6, 4) \quad (5.31) \\ &= v(1, 2) + i \int d7 d4 d5 d6 v(2, 4) G(4, 5) \int d3 v(1, 3) \frac{\delta V(7)}{\delta w(3)} \frac{\delta G^{-1}(5, 6)}{\delta V(7)} G(6, 4) \\ &= v(1, 2) + i \int d7 d4 d5 d6 v(2, 4) G(4, 5) W(1, 7) \frac{\delta G^{-1}(5, 6)}{\delta V(2)} G(6, 4) \\ &= v(1, 2) + i \int d3 d4 d5 d6 W(1, 3) G(4, 5) G(6, 4) \frac{\delta G^{-1}(5, 6)}{\delta V(2)} v(2, 4). \end{aligned}$$

Where 7 was renamed to 3 in the last line. This last expression can be rewritten by defining the Polarisation P .

$$\begin{aligned} W(1, 2) &= v(1, 2) + \int d3 d4 W(1, 3) P(3, 4) v(2, 4) \\ P(2, 4) &= \iint d5 d6 G(4, 5) G(6, 4) \frac{\delta G^{-1}(5, 6)}{\delta V(2)} \end{aligned} \quad (5.32)$$

5.5 Derivation of Vertex Function

Start with the definition of the non-interacting Green's Function

$$\left(i\frac{\partial}{\partial t_1} - h(1) - V(1)\right) G_0(1, 2) = \delta(1, 2). \quad (5.33)$$

We can multiply the equation above from the right side with $G_0^{-1}(2, 3)$ and integrate over 2.

$$\begin{aligned} \int d2 \left(i\frac{\partial}{\partial t_1} - h(1) - V(1)\right) G_0(1, 2) G_0^{-1}(2, 3) &= \int d2 \delta(1, 2) G_0^{-1}(2, 3) \\ \left(i\frac{\partial}{\partial t_1} - h(1) - V(1)\right) \int d2 G_0(1, 2) G_0^{-1}(2, 3) &= G_0^{-1}(1, 3) \\ \left(i\frac{\partial}{\partial t_1} - h(1) - V(1)\right) \delta(1, 3) &= G_0^{-1}(1, 3) \end{aligned} \quad (5.34)$$

We rename 3 to 2 and take the derivative of the equation above.

$$\begin{aligned} \frac{\delta}{\delta V(3)} \left(i\frac{\partial}{\partial t_1} - h(1) - V(1)\right) \delta(1, 2) &= \frac{\delta G_0^{-1}(1, 2)}{\delta V(3)} \\ \frac{\delta}{\delta V(3)} \left(i\frac{\partial}{\partial t_1} - h(1)\right) \delta(1, 2) - \frac{\delta V(1)}{\delta V(3)} \delta(1, 2) &= \frac{\delta G_0^{-1}(1, 2)}{\delta V(3)} \end{aligned} \quad (5.35)$$

The term on the left is 0 since it has no V dependence and the second term on the left side yields an additional delta.

$$-\delta(1, 3) \delta(1, 2) = \frac{\delta G_0^{-1}(1, 2)}{\delta V(3)} \quad (5.36)$$

We can now insert this result into equation (2.44), to find an expression to calculate the vertex function.

$$\Gamma(1, 2; 3) = \delta(1, 2) \delta(1, 3) + \frac{\delta \Sigma(1, 2)}{\delta V(3)} \quad (5.37)$$

5.6 Derivative of Green's Function

We assume that the Green's function has the form $G = \frac{s}{t}$ like in equation (2.31). Therefore one obtains the following equation

$$\frac{\delta G(1, 2)}{\delta w(3)} = \frac{\delta}{\delta w(3)} \frac{s}{t} = \frac{\frac{\delta s}{\delta w(3)}}{t} - \frac{s}{t} \frac{\delta t}{\delta w(3)}. \quad (5.38)$$

For s and t both derivatives are easy to compute as s has the same structure as equation (2.30) and t is simply the derivative of the perturbed time evolution operator in equation (2.28). This yields

$$\begin{aligned} i \frac{\delta G(1, 2)}{\delta w(3)} &= \frac{-i \langle N | \hat{U}_0(-T_0 T_0) \hat{U}(T_0, -T_0) \hat{\mathcal{T}} \left(\hat{\rho}(3) \hat{\psi}(1) \hat{\psi}^\dagger(2) \right) | N \rangle}{\langle N | \hat{U}_0(-T_0, T_0) \hat{U}(T_0, -T_0) | N \rangle} \\ &\quad - \frac{-i \langle N | \hat{U}_0(-T_0 T_0) \hat{U}(T_0, -T_0) \hat{\rho}(3) | N \rangle}{\langle N | \hat{U}_0(-T_0, T_0) \hat{U}(T_0, -T_0) | N \rangle} \cdot G(1, 2). \end{aligned} \quad (5.39)$$

where the right-hand side is simply the difference between the two-particle Green's functions and the product of two one-particle Green's functions. With the correct choice of coordinate names, this reduces to the expression (2.56)

$$\frac{\delta G_1(1, 2)}{\delta w(x, x', t)} = -G_2(1, x't; 2, xt^+) + G_1(1, 2)G_1(x't, xt^+). \quad (5.40)$$

5.7 Fock Term of the Self-Energy Operator

The exchange part of the self-energy operator was defined in equation (2.52)

$$\Sigma^X(1, 2) = iG(1, 2)v(1, 2). \quad (5.41)$$

This can be rewritten in Fourier space in the following way if one inserts $v(1, 2) = v(x - x')\delta(t - t')$ and the Fourier transformation of the delta distribution.

$$\Sigma^X(1, 2) = \frac{i}{2\pi}v(x - x') \lim_{\Delta t \rightarrow 0} \oint d\omega e^{i\Delta t\omega} G(x_1, x_2, \omega) \quad (5.42)$$

Now insert the Lehmann representation of the Greens function from equation (2.8). For this, we define the quasiparticle energies as $\epsilon_l = E_0^N - E_l^{N-1}$ and $\epsilon_m = E_m^{N+1} - E_0^N$.

$$\Sigma^X(1, 2) = \frac{i}{2\pi}v(x - x') \lim_{\Delta t \rightarrow 0} \oint d\omega e^{i\Delta t\omega} \left[\sum_{l=0}^{occ.} \frac{f_l(x)f_l^*(x')}{\omega - \epsilon_l - i\eta} + \sum_{m=0}^{virt.} \frac{g_m(x')g_m^*(x)}{\omega - \epsilon_m + i\eta} \right] \quad (5.43)$$

We want to make use of the residue theorem to solve this integral, therefore we take a closer look at the term under the integral. The poles of this function are purely located in either the upper or lower part of the complex plane. We chose to integrate along a contour in the upper half, which means that the residues of the second term do not contribute. The remaining residues can be calculated in the following way

$$\begin{aligned} \text{Res}(G, \omega_i) &= \sum_l (\omega - \epsilon_l - i\eta) \frac{f_l(x)f_l^*(x')}{\omega - \epsilon_l - i\eta} \Big|_{\omega=\epsilon_m+i\eta} \\ &= \sum_l f_l(x)f_l^*(x'). \end{aligned} \quad (5.44)$$

Therefore we conclude

$$\begin{aligned} \Sigma^X(1, 2) &= \frac{i}{2\pi}v(x - x')2\pi i \sum_l f_l(x)f_l^*(x') \\ &= - \sum_l \frac{f_l(x)f_l^*(x')}{|x - x'|}. \end{aligned} \quad (5.45)$$

Taking the expectation value and replacing the Lehmann amplitudes with molecular orbitals ϕ_l results in the Fock exchange from Hartree Fock

$$\langle \phi_k | \Sigma^X(1, 2) | \phi_k \rangle = - \sum_l \iint dx dx' \frac{\phi_k(x')\phi_l(x)\phi_l^*(x')\phi_k^*(x)}{|x - x'|}. \quad (5.46)$$

5.8 First Order Response of the Transition Density Matrix

To justify 2.82 one can start by defining the one-particle density $\rho(x, t)$ and the one-particle density matrix $\gamma(x, x', t)$ with the following convention: $i, j, k =$ occupied orbitals, $a, b, c =$ virtual orbitals, $p, q =$ arbitrary orbitals^[68]

$$\rho(x, t) = \sum_{i=occ}^N |\phi_i(x, t)|^2 \quad (5.47)$$

and

$$\gamma(x, x', t) = \sum_{i=occ}^N \phi_i(x, t) \phi_i^*(x', t) \quad (5.48)$$

which fulfills the following equation of motion and idempotency relation if the wavefunction is described by a single Slater determinant, as in the case of DFT and GW-BSE.^[67]

$$i \frac{\partial \gamma(x, x', t)}{\partial t} = [H, \gamma(x, x', t)] \quad (5.49)$$

$$\gamma(x, x', t) = \int dx_1 \gamma(x, x_1, t) \gamma(x_1, x', t) \quad (5.50)$$

If one assumes an external potential, that is periodic with a frequency ω_α and can be expanded in a power series with respect to a certain coupling strength λ_α , one will obtain the following expansion for the field and the one-particle density matrix

$$v_{ext}(x, t) = v^{(0)}(x) + \sum_{\alpha>0} \lambda_\alpha \left[v^{(\alpha)}(\omega_\alpha, x) e^{i\omega_\alpha t} + v^{(\alpha)}(-\omega_\alpha, x) e^{-i\omega_\alpha t} \right]. \quad (5.51)$$

$$\gamma_\alpha(x, x', t) = \gamma_\alpha^{(0)}(x, x') + \lambda_\alpha \underbrace{\left[\gamma^{(\alpha)}(\omega_\alpha, x, x') e^{i\omega_\alpha t} + \gamma^{(\alpha)}(-\omega_\alpha, x, x') e^{-i\omega_\alpha t} \right]}_{\left. \frac{\partial \gamma(x, x', t)}{\partial \lambda_\alpha} \right|_{\lambda_\alpha=0}} + \dots \quad (5.52)$$

Inserting equation (5.52) into equation (5.50) leads to

$$\begin{aligned} & \gamma^{(0)}(x, x') + \lambda_\alpha \left[\gamma^{(\alpha)}(\omega_\alpha, x, x') e^{i\omega_\alpha t} + \gamma^{(\alpha)}(-\omega_\alpha, x, x') e^{-i\omega_\alpha t} \right] \\ &= \int dx_1 \left[\gamma^{(0)}(x, x_1) + \lambda_\alpha \left(\gamma^{(\alpha)}(\omega_\alpha, x, x_1) e^{i\omega_\alpha t} + \gamma^{(\alpha)}(-\omega_\alpha, x, x_1) e^{-i\omega_\alpha t} \right) + \dots \right] \\ & \cdot \left[\gamma^{(0)}(x_1, x') + \lambda_\alpha \left(\gamma^{(\alpha)}(\omega_\alpha, x_1, x') e^{i\omega_\alpha t} + \gamma^{(\alpha)}(-\omega_\alpha, x_1, x') e^{-i\omega_\alpha t} \right) + \dots \right] \\ &= \int dx_1 \gamma^{(0)}(x, x_1) \gamma^{(0)}(x_1, x') + \\ & \lambda_\alpha \left[\int dx_1 \gamma^{(0)}(x, x_1) \left(\gamma^{(\alpha)}(\omega_\alpha, x_1, x') e^{i\omega_\alpha t} + \gamma^{(\alpha)}(-\omega_\alpha, x_1, x') e^{-i\omega_\alpha t} \right) \right. \\ & \left. + \int dx_1 \lambda_\alpha \left(\gamma^{(\alpha)}(\omega_\alpha, x, x_1) e^{i\omega_\alpha t} + \gamma^{(\alpha)}(-\omega_\alpha, x, x_1) e^{-i\omega_\alpha t} \right) \gamma^{(0)}(x_1, x') \right] \\ & + \mathcal{O}(\lambda_\alpha^2). \end{aligned} \quad (5.53)$$

We drop the higher-order response term and keep only the constant and the linear term. This way we can perform a coefficient comparison of the oscillating terms through which we obtain

$$\gamma^{(0)}(x, x') = \int dx_1 \gamma^{(0)}(x, x_1) \gamma^{(0)}(x_1, x') \quad (5.54)$$

and

$$\gamma^{(\alpha)}(\omega_\alpha, x, x') = \int dx_1 \gamma^{(0)}(x, x_1) \gamma^{(\alpha)}(\omega_\alpha, x_1, x') + \gamma^{(\alpha)}(\omega_\alpha, x, x_1) \gamma^{(0)}(x_1, x'). \quad (5.55)$$

Now, we focus on the linear response (5.55) and transform the equation into the MO basis, resulting in the matrix element

$$\gamma_{pq}^{(0)} = \int dx dx' \phi_p^*(x) \gamma^{(0)}(x, x') \phi_q(x') = \sum_i \delta_{pi} \delta_{qi} \quad (5.56)$$

where the definition (5.48) was inserted in the last step.

Now, we investigate the occupied-occupied, the virtual-virtual, the occupied-virtual, and the virtual-occupied blocks individually. In the case of the occupied-occupied block, this leads to

$$\left(\gamma^{(\alpha)}\right)_{ij} = \int dx_1 \underbrace{\left(\gamma^{(0)}\gamma^{(\alpha)}\right)_{ij}}_{=I} + \underbrace{\left(\gamma^{(\alpha)}\gamma^{(0)}\right)_{ij}}_{=II}. \quad (5.57)$$

If we focus on the first term we obtain

$$\begin{aligned} I &= \int dx_1 dx dx' \phi_i^*(x) \gamma^{(0)}(x, x_1) \gamma^{(\alpha)}(x_1, x') \phi_j(x') \\ &= \int dx_1 dx dx' \phi_i^*(x) \sum_k \phi_k(x) \phi_k^*(x_1) \gamma^{(\alpha)}(x_1, x') \phi_j(x') \\ &= \sum_k \int dx_1 dx' \phi_k^*(x_1) \gamma^{(\alpha)}(x_1, x') \phi_j(x') \underbrace{\int dx \phi_i^*(x) \phi_k(x)}_{\delta_{ik}} \\ &= \int dx_1 dx' \phi_i^*(x_1) \gamma^{(\alpha)}(x_1, x') \phi_j(x') \\ &= \left(\gamma^{(\alpha)}\right)_{ij}. \end{aligned} \quad (5.58)$$

In the same way one can show that $II = \left(\gamma^{(\alpha)}\right)_{ij}$, which will lead to the final expression

$$\left(\gamma^{(\alpha)}\right)_{ij} = \left(\gamma^{(\alpha)}\right)_{ij} + \left(\gamma^{(\alpha)}\right)_{ij} = 2 \left(\gamma^{(\alpha)}\right)_{ij}. \quad (5.59)$$

This expression is only fulfilled if $\left(\gamma^{(\alpha)}\right)_{ij} = 0$ and the occupied-occupied block is consequently 0 in linear response. The same analysis can be done for the virtual-virtual block, which must also be equal to 0 in linear response.

For the occupied-virtual block, we obtain from equation (5.55)

$$\left(\gamma^{(\alpha)}\right)_{ia} = \int dx_1 \underbrace{\left(\gamma^{(0)}\gamma^{(\alpha)}\right)_{ia}}_I + \underbrace{\left(\gamma^{(\alpha)}\gamma^{(0)}\right)_{ia}}_{II} \quad (5.60)$$

with

$$\begin{aligned}
I &= \int dx_1 dx dx' \phi_i^*(x) \gamma^{(0)}(x, x_1) \gamma^{(\alpha)}(x_1, x') \phi_a(x') \\
&= \int dx_1 dx dx' \phi_i^*(x) \sum_j \phi_j(x) \phi_j^*(x_1) \gamma^{(\alpha)}(x_1, x') \phi_a(x') \\
&= \sum_j \int dx_1 dx' \phi_j^*(x_1) \gamma^{(\alpha)}(x_1, x') \phi_a(x') \underbrace{\int dx \phi_i^*(x) \phi_j(x)}_{\delta_{ij}} \\
&= \int dx_1 dx' \phi_i^*(x_1) \gamma^{(\alpha)}(x_1, x') \phi_a(x') \\
&= \left(\gamma^{(\alpha)} \right)_{ia}
\end{aligned} \tag{5.61}$$

, which is the same result as for the occupied-occupied block. However, for the second term we calculate

$$\begin{aligned}
II &= \int dx_1 dx dx' \phi_i^*(x) \gamma^{(\alpha)}(x, x_1) \gamma^{(0)}(x_1, x') \phi_a(x') \\
&= \int dx_1 dx dx' \phi_i^*(x) \gamma^{(\alpha)}(x_1, x') \sum_j \phi_j(x_1) \phi_j^*(x') \phi_a(x') \\
&= \sum_j \int dx_1 dx \phi_i^*(x) \gamma^{(\alpha)}(x_1, x') \phi_j(x_1) \underbrace{\int dx' \phi_j^*(x') \phi_a(x')}_{=\delta_{ja}=0} \\
&= 0.
\end{aligned} \tag{5.62}$$

The integral in the last line disappears because both sets of i and a orbitals have no intersection. This will result in the following expression

$$\left(\gamma^{(\alpha)} \right)_{ia} = \left(\gamma^{(\alpha)} \right)_{ia} \tag{5.63}$$

which means that the occupied-virtual block can have finite values. The same result is found for the virtual-occupied block. If we call the occupied-virtual block X_{ia} and the virtual-occupied block Y_{ia} , we can write down expression 2.80 and 2.82 as

$$\gamma^{(\alpha)}(x, x') = \sum_{ia} X_{ia}^{(\alpha)} \phi_i(x) \phi_a(x') + Y_{ia}^{(\alpha)} \phi_i(x') \phi_a(x). \tag{5.64}$$

As a final note, the same analysis may be performed for higher orders, particularly the second order. In this case, the final one-particle density reads^[67]

$$\gamma^{(\alpha\beta)}(x, x') = \sum_{uv} K_{uv}^{(\alpha\beta)} \phi_u(x) \phi_v(x') + \sum_{ia} X^{(\alpha\beta)} \phi_a(x) \phi_i(x') + Y_{ia}^{(\alpha\beta)} \phi_i(x) \phi_a(x') \tag{5.65}$$

with

$$\begin{aligned}
K_{ij}^{(\alpha\beta)} &= - \sum_a X_{ja}^{(\alpha)} Y_{ia}^{(\beta)} + Y_{ia}^{(\alpha)} X_{ja}^{(\beta)} \\
K_{ab}^{(\alpha\beta)} &= \sum_i Y_{ib}^{(\alpha)} X_{ia}^{(\beta)} + X_{ia}^{(\alpha)} Y_{ib}^{(\beta)}.
\end{aligned} \tag{5.66}$$

This second-order response will be used to calculate spin-orbit coupling matrix elements in chapter 2.8.

5.9 BSE in Fourier Space

The BSE in real space reads after the insertion of the equation (2.61) into (2.59)

$$\begin{aligned}
L(1, 2; 1', 2') &= L_0(1, 2; 1', 2') + i \int d3d4d5d6 L(1, 4; 1', 3) \delta(3, 6) \delta(4, 5) W(3, 4) L(6, 2; 5, 2') \\
&\quad - L(1, 4; 1', 3) \delta(3, 4) \delta(5, 6) v(3, 6) L(6, 2; 5, 2') \\
&= L_0(1, 2; 1', 2') + i \int d4d6 L_0(1, 4; 1', 6) W(6, 4) L(6, 2; 4, 2') \\
&\quad - L_0(1, 4; 1', 4) v(4, 6) L(6, 2; 6, 2').
\end{aligned} \tag{5.67}$$

After renaming some indices this results in

$$\begin{aligned}
L(1, 2; 1', 2') &= L_0(1, 2; 1', 2') + i \int d3d4 L_0(1, 3; 1', 4) W(4, 3) L(4, 2; 3, 2') \\
&\quad - L_0(1, 3; 1', 3) v(3, 4) L(4, 2; 4, 2').
\end{aligned} \tag{5.68}$$

We make the approximation that $W(1, 2) = W(x_1, x_2) \delta(t_1 - t_2)$ holds. This is motivated by the fact that the regular coulomb potential takes the form $v(1, 2) = v(x_1, x_2) \delta(t_1 - t_2)$. This leads to

$$\begin{aligned}
L(t_1 - t_2, t_2 - t_1) &= L_0(t_1 - t_2, t_2 - t_1) + i \int dt_3 L_0(t_1 - t_3; t_3 - t_1) W(x_3, x_4) L(t_3 - t_2; t_2 - t_3) \\
&\quad - L_0(t_1 - t_3; t_3 - t_1) v(x_3, x_4) L(t_3 - t_2; t_2 - t_3).
\end{aligned} \tag{5.69}$$

We make the substitution $\tau = t_1 - t_2$ and $\tau' = t_3 - t_1$

$$\begin{aligned}
L(\tau, -\tau) &= L_0(\tau, -\tau) + i \int d\tau' L_0(-\tau'; \tau') W(x_3, x_4) L(\tau + \tau'; -\tau - \tau') \\
&\quad - L_0(-\tau'; \tau') v(x_3, x_4) L(\tau' + \tau; -\tau - \tau').
\end{aligned} \tag{5.70}$$

We drop the second variable in each term, as they are the same in both terms under the integral. This way, we can factor out the term $W(x_3, x_4) - v(x_3, x_4)$.

$$L(\tau, -\tau) = L_0(\tau, -\tau) + i \int d\tau' L_0(-\tau'; \tau') L(\tau + \tau'; -\tau - \tau') [W(x_3, x_4) - v(x_3, x_4)] \tag{5.71}$$

This way we identify the definition of the convolution.

$$L(\tau) = L_0(\tau) + i [L_0(\tau) * L(\tau)] (W(x_3, x_4) - v(x_3, x_4)) \tag{5.72}$$

According to the convolution theorem, the Fourier transform of this expression is given by

$$L(\omega) = L_0(\omega) + i L_0(\omega) L(\omega) [W(x_3, x_4) - v(x_3, x_4)]. \tag{5.73}$$

5.10 LVC Model for a mixed def2-SVP/def2-TZVP basis set

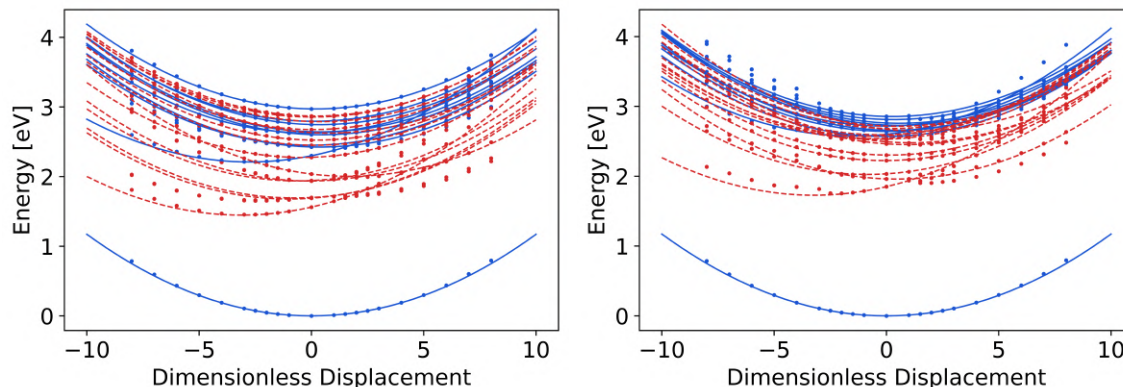


Figure 5.1: LVC Model along the 25. normal mode of the CPMP complex in the diabatic representation. The left figure shows this model for the DFT level of theory using an LC-BLY($\alpha = 0.2$, $\omega = 0.08$) functional. The right figure shows the corresponding results for the GW-BSE level of theory. Both calculations used a mixed def2-SVP basis set for the ligand and def2-TZVP for the central metal. The normal mode vector has a negative sign, which means that a negative displacement corresponds to an elongation of the Fe-N distance.

One can compare these PES to the diabatic surfaces obtained in figure 3.35. Doing that shows that in particular the GW-BSE PES depend strongly on the basis set used. In the case of DFT, the dependence is weaker, however also in this case they will lead to different dynamics. For this reason, we favored the use of a larger basis set especially for the GW-BSE PES.

Bibliography

- [1] I. P. on Climate Change (IPCC). Global Warming of 1.5°C: IPCC Special Report on Impacts of Global Warming of 1.5°C above Pre-industrial Levels in Context of Strengthening Response to Climate Change, Sustainable Development, and Efforts to Eradicate Poverty. Cambridge University Press (2022).
- [2] N. Armaroli and V. Balzani. “The future of energy supply: Challenges and opportunities”. *Angewandte Chemie International Edition* **46**, 52 (2007).
- [3] H. Arakawa, M. Aresta, J. N. Armor, M. A. Barteau, E. J. Beckman, A. T. Bell, J. E. Bercaw, C. Creutz, E. Dinjus, D. A. Dixon, K. Domen, D. L. DuBois, J. Eckert, E. Fujita, D. H. Gibson, W. A. Goddard, D. W. Goodman, J. Keller, G. J. Kubas, H. H. Kung, J. E. Lyons, L. E. Manzer, T. J. Marks, K. Morokuma, K. M. Nicholas, R. Periana, L. Que, J. Rostrup-Nielson, W. M. H. Sachtler, L. D. Schmidt, A. Sen, G. A. Somorjai, P. C. Stair, B. R. Stults, and W. Tumas. “Catalysis research of relevance to carbon management: Progress, challenges, and opportunities”. *Chemical Reviews* **101**, 953. PMID: 11709862 (2001).
- [4] Y. You and W. Nam. “Photofunctional triplet excited states of cyclometalated ir(III) complexes: beyond electroluminescence”. *Chem. Soc. Rev.* **41**, 7061 (2012).
- [5] S. Fischer, D. Hollmann, S. Tschierlei, M. Karnahl, N. Rockstroh, E. Barsch, P. Schwarzbach, S.-P. Luo, H. Junge, M. Beller, S. Lochbrunner, R. Ludwig, and A. Brückner. “Death and rebirth: Photocatalytic hydrogen production by a self-organizing copper–iron system”. *ACS Catalysis* **4**, 1845 (2014).
- [6] Y. Liu, P. Persson, V. Sundström, and K. Wärnmark. “Fe η -heterocyclic carbene complexes as promising photosensitizers”. *Accounts of Chemical Research* **49**, 1477. PMID: 27455191 (2016).
- [7] A. Pöpcke, A. Friedrich, and S. Lochbrunner. “Revealing the initial steps in homogeneous photocatalysis by time-resolved spectroscopy”. *Journal of Physics: Condensed Matter* **32**, 153001 (2020).
- [8] L. González and R. Lindh. Quantum Chemistry and Dynamics of Excited States: Methods and Applications. Wiley (2021).
- [9] R. Crespo-Otero and M. Barbatti. “Recent advances and perspectives on nonadiabatic mixed quantum–classical dynamics”. *Chemical Reviews* **118**, 7026. PMID: 29767966 (2018).
- [10] S. I. Bokarev, O. S. Bokareva, and O. Kühn. “Electronic excitation spectrum of the photosensitizer [Ir(ppy)₂(bpy)]⁺”. *The Journal of Chemical Physics* **136**, 214305 (2012).
- [11] B. Weber. Koordinationschemie, Grundlagen und aktuelle Trends. Springer Spektrum Berlin, Heidelberg (2022).
- [12] B. Figgis and M. Hitchman. Ligand Field Theory and Its Applications. Special Topics in Inorganic Chemistry. Wiley (2000).
- [13] O. S. Wenger. “Is iron the new ruthenium?”. *Chemistry – A European Journal* **25**, 6043 (2019).

- [14] T. P. Silverstein. “Marcus theory: Thermodynamics can control the kinetics of electron transfer reactions”. *Journal of Chemical Education* **89**, 1159 (2012).
- [15] B. Altenburger. Investigation of Iron Complexes as Photosensitizers by Transient Absorption and Emission Spectroscopy. Ph.D. thesis, University of Rostock (2019).
- [16] Y. Liu, T. Harlang, S. E. Canton, P. Chábera, K. Suárez-Alcántara, A. Fleckhaus, D. A. Vithanage, E. Göransson, A. Corani, R. Lomoth, V. Sundström, and K. Wärnmark. “Towards longer-lived metal-to-ligand charge transfer states of iron(ii) complexes: an n-heterocyclic carbene approach”. *Chem. Commun.* **49**, 6412 (2013).
- [17] T. Biswas and A. K. Singh. “py gwbse: a high throughput workflow package for gw-bse calculations”. *npj Computational Materials* **9**, 22 (2023).
- [18] X. Leng, F. Jin, M. Wei, and Y. Ma. “Gw method and bethe–salpeter equation for calculating electronic excitations”. *WIREs Computational Molecular Science* **6**, 532 (2016).
- [19] S. Salsa and G. Verzini. *Partial Differential Equations in Action*. Springer Cham (2022).
- [20] G. D. Mahan. *Many-particle physics*. New York Plenum Press (1981).
- [21] T. Lancaster and B. S. J. *Quantum Field Theory for the Gifted Amateur*. Oxford University Press (2014).
- [22] N. J. Horing. *Quantum Statistical Field Theory*. Oxford University Press (2017).
- [23] A. L. Fetter and J. D. Walecka. *Quantum Theory of Many-particle Systems*. Courier Corporation (2003).
- [24] L. Reining. “The gw approximation: content, successes and limitations”. *WIREs Computational Molecular Science* **8**, e1344 (2018).
- [25] L. G. Molinari. “A derivation of hedin’s equation”. <https://citeseerx.ist.psu.edu/document?repid=rep1&type=pdf&doi=c2f40737485cd5231454f54ca56dfe8b08f333dc>. [Accessed 05-05-2024] (2007).
- [26] S. Kurth. “Introduction to green functions, the gw approximation, and the bethe-salpeter equation”. https://nano-bio.ehu.es/files/kurth_green.pdf. [Accessed 06-05-2024] (2015).
- [27] X. Blase, C. Attaccalite, and V. Olevano. “First-principles calculations for fullerenes, porphyrins, phtalocyanine, and other molecules of interest for organic photovoltaic applications”. *Physical Review B* **83** (2011).
- [28] L. Hedin. “New method for calculating the one-particle green’s function with application to the electron-gas problem”. *Phys. Rev.* **139**, A796 (1965).
- [29] G. Strinati. “Application of the green’s functions method to the study of the optical properties of semiconductors”. *Revista del nuovo cimento* **11** (1988).
- [30] F. Kaplan, M. E. Harding, C. Seiler, F. Weigend, F. Evers, and M. J. van Setten. “Quasi-particle self-consistent gw for molecules”. *Journal of Chemical Theory and Computation* **12**, 2528 (2016).
- [31] L. D. Landau, E. M. Lifshitz, and L. P. Pitaevskij. *Statistical Physics: Part 2: Theory of Condensed State*. Oxford Landau and Lifshitz Course of Theoretical Physics (1980).

- [32] R. Mattuck. A Guide to Feynman Diagrams in the Many-body Problem. Dover Books on Physics Series. Dover Publications (1992).
- [33] D. Golze, M. Dvorak, and P. Rinke. “The gw compendium: A practical guide to theoretical photoemission spectroscopy”. *Frontiers in Chemistry* **7** (2019).
- [34] P. Rinke. “Gw quasiparticle calculations, hands-on tutorial on ab initio molecular simulations: Toward a first-principles understanding of materials properties and functions”. [Accessed 18-06-2024].
- [35] C. Faber. Electronic, excitonic and polaronic properties of organic systems within the many-body GW and Bethe-Salpeter formalisms: towards organic photovoltaics. Ph.D. thesis, Université Grenoble Alpes (2014).
- [36] S. Ghosh, P. Verma, C. J. Cramer, L. Gagliardi, and D. G. Truhlar. “Combining wave function methods with density functional theory for excited states”. *Chemical Reviews* **118**, 7249. PMID: 30044618 (2018).
- [37] C. Holzer. Die GW-Methode und Bethe-Salpeter-Gleichung in der Quantenchemie: Theorie und Anwendung. Ph.D. thesis, Karlsruhe Institute of Technology (2018).
- [38] Z. Li. “Introduction to gw, gw-bethe-salpeter-equation (gw-bse), and gw perturbation theory (gwpt)”. https://docs.epw-code.org/_downloads/376056430cfb845bbcb929548b7156a6/Fri.2.Li.pdf.
- [39] X. Gui, C. Holzer, and W. Klopper. “Accuracy assessment of gw starting points for calculating molecular excitation energies using the bethe–salpeter formalism”. *Journal of Chemical Theory and Computation* **14**, 2127. PMID: 29499116 (2018).
- [40] M. Govoni and G. Galli. “Large scale gw calculations”. *Journal of Chemical Theory and Computation* **11**, 2680. PMID: 26575564 (2015).
- [41] R. L. Panadés-Barrueta and D. Golze. “Accelerating core-level gw calculations by combining the contour deformation approach with the analytic continuation of w”. *Journal of Chemical Theory and Computation* **19**, 5450. PMID: 37566917 (2023).
- [42] D. Golze, J. Wilhelm, M. J. van Setten, and P. Rinke. “Core-level binding energies from gw: An efficient full-frequency approach within a localized basis”. *Journal of Chemical Theory and Computation* **14**, 4856. PMID: 30092140 (2018).
- [43] J. Wilhelm, D. Golze, L. Talirz, J. Hutter, and C. A. Pignedoli. “Toward gw calculations on thousands of atoms”. *The Journal of Physical Chemistry Letters* **9**, 306. PMID: 29280376 (2018).
- [44] X. Blase, I. Duchemin, and D. Jacquemin. “The bethe–salpeter equation formalism: From physics to chemistry”. *J. Phys. Chem. Lett.* **11** (2020).
- [45] W. Parson. Modern Optical Spectroscopy: With Exercises and Examples from Biophysics and Biochemistry. Springer Berlin Heidelberg (2015).
- [46] J. Tölle, T. Deilmann, M. Rohlfing, and J. Neugebauer. “Subsystem-based gw/bethe–salpeter equation”. *Journal of Chemical Theory and Computation* **17**, 2186. PMID: 33683119 (2021).
- [47] W.-k. Chen, X.-w. Sun, Q. Fang, X.-y. Liu, and G.-l. Cui. “GW/BSE nonadiabatic dynamics simulations on excited-state relaxation processes of zinc phthalocyanine-fullerene dyads: Roles of bridging chemical bonds †”. *Chinese Journal of Chemical Physics* **34**, 704 (2021).

- [48] D. Jacquemin, I. Duchemin, A. Blondel, and X. Blase. “Assessment of the accuracy of the bethe–salpeter (bse/gw) oscillator strengths”. *Journal of Chemical Theory and Computation* **12**, 3969. PMID: 27403612 (2016).
- [49] F. Plasser, M. Wormit, and A. Dreuw. “New tools for the systematic analysis and visualization of electronic excitations. I. Formalism”. *The Journal of Chemical Physics* **141**, 024106 (2014).
- [50] D. Rocca, M. Vörös, A. Gali, and G. Galli. “Ab initio optoelectronic properties of silicon nanoparticles: Excitation energies, sum rules, and tamm–dancoff approximation”. *Journal of Chemical Theory and Computation* **10**, 3290. PMID: 26588298 (2014).
- [51] M. J. G. Peach and D. J. Tozer. “Overcoming low orbital overlap and triplet instability problems in tddft”. *The Journal of Physical Chemistry A* **116**, 9783. PMID: 22971224 (2012).
- [52] T. Rangel, S. M. Hamed, F. Bruneval, and J. B. Neaton. “An assessment of low-lying excitation energies and triplet instabilities of organic molecules with an ab initio Bethe–Salpeter equation approach and the Tamm–Dancoff approximation”. *The Journal of Chemical Physics* **146**, 194108 (2017).
- [53] C. Holzer and W. Klopper. “Communication: A hybrid Bethe–Salpeter/time-dependent density-functional-theory approach for excitation energies”. *The Journal of Chemical Physics* **149**, 101101 (2018).
- [54] J. T. Skolnik and D. A. Mazziotti. “Cumulant reduced density matrices as measures of statistical dependence and entanglement between electronic quantum domains with application to photosynthetic light harvesting”. *Phys. Rev. A* **88**, 032517 (2013).
- [55] F. Plasser. Quantum Mechanical Simulations of Defect Dynamics in DNA and Model Systems. Ph.D. thesis, University of Vienna (2012).
- [56] F. Plasser and H. Lischka. “Analysis of excitonic and charge transfer interactions from quantum chemical calculations”. *Journal of Chemical Theory and Computation* **8**, 2777. PMID: 26592119 (2012).
- [57] F. Plasser. “Theodore: A toolbox for a detailed and automated analysis of electronic excited state computations”. *The Journal of Chemical Physics* **152**, 084108 (2020).
- [58] V. I. Hertel and C. P. Schulz. *Atoms, Molecules and Optical Physics 2*. Springer Berlin, Heidelberg (2015).
- [59] O. Kühn and V. May. *Charge and Energy Transfer Dynamics in Molecular Systems*. Wiley-VCH, Weinheim (2023).
- [60] F. Gatti, B. Lasorne, H. D. Meyer, and A. Nauts. *Applications of Quantum Dynamics in Chemistry*. Springer Cham (2017).
- [61] C. Cohen-Tannoudji, B. Diu, and F. Laloë. *Quantum Mechanics*. John Wiley and Sons, Ltd (1991).
- [62] A. Tokmakoff. “Diabatic and adiabatic states”. [https://chem.libretexts.org/Bookshelves/Physical_and_Theoretical_Chemistry_Textbook_Maps/Time_Dependent_Quantum_Mechanics_and_Spectroscopy_\(Tokmakoff\)/06%3A_Adiabatic_Approximation/6.03%3A_Diabatic_and_Adiabatic_States](https://chem.libretexts.org/Bookshelves/Physical_and_Theoretical_Chemistry_Textbook_Maps/Time_Dependent_Quantum_Mechanics_and_Spectroscopy_(Tokmakoff)/06%3A_Adiabatic_Approximation/6.03%3A_Diabatic_and_Adiabatic_States). [Accessed 19-06-2024].

- [63] H. Köppel, W. Domcke, and L. S. Cederbaum. Multimode Molecular Dynamics Beyond the Born-Oppenheimer Approximation, 59–246. John Wiley and Sons, Ltd (1984).
- [64] F. Plasser, S. Gómez, M. F. S. J. Menger, S. Mai, and L. González. “Highly efficient surface hopping dynamics using a linear vibronic coupling model”. *Phys. Chem. Chem. Phys.* **21**, 57 (2019).
- [65] F. Plasser, M. Ruckebauer, S. Mai, M. Oppel, P. Marquetand, and L. González. “Efficient and flexible computation of many-electron wave function overlaps”. *Journal of Chemical Theory and Computation* **12**, 1207. PMID: 26854874 (2016).
- [66] C. Holzer and W. Klopper. “Ionized, electron-attached, and excited states of molecular systems with spin-orbit coupling: Two-component GW and Bethe-Salpeter implementations”. *The Journal of Chemical Physics* **150**, 204116 (2019).
- [67] F. Furche. “On the density matrix based approach to time-dependent density functional response theory”. *The Journal of Chemical Physics* **114**, 5982 (2001).
- [68] S. M. Parker, D. Rappoport, and F. Furche. “Quadratic response properties from tddft: Trials and tribulations”. *Journal of Chemical Theory and Computation* **14**, 807. PMID: 29232511 (2018).
- [69] X. Gao, S. Bai, D. Fazzi, T. Niehaus, M. Barbatti, and W. Thiel. “Evaluation of spin-orbit couplings with linear-response time-dependent density functional methods”. *Journal of Chemical Theory and Computation* **13**, 515. PMID: 27959528 (2017).
- [70] S. G. Chiodo and M. Leopoldini. “Molsoc: A spin-orbit coupling code”. *Computer Physics Communications* **185**, 676 (2014).
- [71] “Turbomole v7.8 2023, a development of university of karlsruhe and forschungszentrum karlsruhe gmbh”. <https://www.turbomole.org> (1989-2007).
- [72] S. G. Balasubramani, G. P. Chen, S. Coriani, M. Diedenhofen, M. S. Frank, Y. J. Franzke, F. Furche, R. Grotjahn, M. E. Harding, C. Hättig, A. Hellweg, B. Helmich-Paris, C. Holzer, U. Huniar, M. Kaupp, A. Marefat Khah, S. Karbalaei Khani, T. Müller, F. Mack, B. D. Nguyen, S. M. Parker, E. Perlt, D. Rappoport, K. Reiter, S. Roy, M. Rückert, G. Schmitz, M. Sierka, E. Tapavicza, D. P. Tew, C. van Wüllen, V. K. Voora, F. Weigend, A. Wody’ski, and J. M. Yu. “Turbomole: Modular program suite for *ab initio* quantum-chemical and condensed-matter simulations”. *J. Chem. Phys.* **152**, 184107 (2020).
- [73] M. Häser and R. Ahlrichs. “Improvements on the direct scf method”. *Journal of Computational Chemistry* **10**, 104 (1989).
- [74] O. Treutler and R. Ahlrichs. “Efficient molecular numerical integration schemes”. *The Journal of Chemical Physics* **102**, 346 (1995).
- [75] P. Deglmann, K. May, F. Furche, and R. Ahlrichs. “Nuclear second analytical derivative calculations using auxiliary basis set expansions”. *Chemical Physics Letters* **384**, 103 (2004).
- [76] A. Klamt and G. Schürmann. “Cosmo: a new approach to dielectric screening in solvents with explicit expressions for the screening energy and its gradient”. *J. Chem. Soc., Perkin Trans. 2* 799–805 (1993).
- [77] F. Weigend and M. Häser. “Ri-mp2: first derivatives and global consistency”. *Theoretical Chemistry Accounts* **97**, 331 (1997).

- [78] C. Hättig and F. Weigend. “CC2 excitation energy calculations on large molecules using the resolution of the identity approximation”. *The Journal of Chemical Physics* **113**, 5154 (2000).
- [79] C. Hättig and K. Hald. “Implementation of ri-cc2 triplet excitation energies with an application to trans-azobenzene”. *Phys. Chem. Chem. Phys.* **4**, 2111 (2002).
- [80] C. Hättig. “Structure optimizations for excited states with correlated second-order methods: Cc2 and adc(2)”. In H. Jensen (Editor), Response Theory and Molecular Properties (A Tribute to Jan Linderberg and Poul Jørgensen), *Advances in Quantum Chemistry*, volume 50, 37–60. Academic Press (2005).
- [81] S. Mai, D. Avagliano, M. Heindl, P. Marquetand, M. F. S. J. Menger, M. Oppel, F. Plasser, S. Polonius, M. Ruckebauer, Y. Shu, D. G. Truhlar, L. Zhang, P. Zobel, and L. Gonzalez. “SHARC3.0: Surface hopping including arbitrary couplings — program package for non-adiabatic dynamics”. <https://sharc-md.org/> (2023).
- [82] S. Mai, P. Marquetand, and L. Gonzalez. “Nonadiabatic dynamics: The sharc approach”. *WIREs Comput. Mol. Sci.* **8**, e1370 (2018).
- [83] D. J. Tozer, R. D. Amos, N. C. Handy, B. O. Roos, and L. Serrano-Andres. “Does density functional theory contribute to the understanding of excited states of unsaturated organic compounds?”. *Molecular Physics* **97**, 859 (1999).
- [84] A. Dreuw, G. R. Fleming, and M. Head-Gordon. “Chlorophyll fluorescence quenching by xanthophylls”. *Phys. Chem. Chem. Phys.* **5**, 3247 (2003).
- [85] M. E. Casida. “Time-dependent density-functional theory for molecules and molecular solids”. *Journal of Molecular Structure: THEOCHEM* **914**, 3. Time-dependent density-functional theory for molecules and molecular solids (2009).
- [86] A. Dreuw and M. Head-Gordon. “Single-reference ab initio methods for the calculation of excited states of large molecules”. *Chemical Reviews* **105**, 4009. PMID: 16277369 (2005).
- [87] D. Jacquemin, I. Duchemin, and X. Blase. “Is the bethe–salpeter formalism accurate for excitation energies? comparisons with td-dft, caspt2, and eom-ccsd”. *The Journal of Physical Chemistry Letters* **8**, 1524. PMID: 28301726 (2017).
- [88] J. Deslippe, G. Samsonidze, D. A. Strubbe, M. Jain, M. L. Cohen, and S. G. Louie. “Berkeleygw: A massively parallel computer package for the calculation of the quasi-particle and optical properties of materials and nanostructures”. *Computer Physics Communications* **183**, 1269 (2012).
- [89] K. Wieghardt, U. Bossek, P. Chaudhuri, W. Herrmann, B. C. Menke, and J. Weiss. “1,4,7-triazacyclononane-*n,n',n''*-triacetate (tcta), a new hexadentate ligand for divalent and trivalent metal ions. crystal structures of [cruu(tcta)], [feiii(tcta)], and na[cuii(tcta)].*bul.2nabr.bul.8h2o*”. *Inorganic Chemistry* **21**, 4308 (1982).
- [90] K. Wieghardt, W. Schmidt, W. Herrmann, and H. J. Kueppers. “Redox potentials of bis(1,4,7-triazacyclononane complexes of some first transition series metals(ii,iii). preparation of bis(1,4,7-triazacyclononane)nickel(iii) perchlorate”. *Inorganic Chemistry* **22**, 2953 (1983).
- [91] J. L. Sessler, J. W. Sibert, and V. Lynch. “Bulky substituent effects on the iron(iii) complexation of 1,4,7-triazacyclononane”. *Inorganica Chimica Acta* **216**, 89 (1994).

- [92] M. Zlatar, M. Gruden-Pavlović, M. Güell, and M. Swart. “Computational study of the spin-state energies and uv-vis spectra of bis(1,4,7-triazacyclononane) complexes of some first-row transition metal cations”. *Phys. Chem. Chem. Phys.* **15**, 6631 (2013).
- [93] P. E.M. Siegbahn and M. Svensson. “Geometry optimization for second-row transition metal complexes”. *Chemical Physics Letters* **216**, 147 (1993).
- [94] K. Ghiassi and R. Lancashire. “Jahn-teller distortions”. [https://chem.libretexts.org/Bookshelves/Inorganic_Chemistry/Supplemental_Modules_and_Websites_\(Inorganic_Chemistry\)/Coordination_Chemistry/Structure_and_Nomenclature_of_Coordination_Compounds/Coordination_Numbers_and_Geometry/Jahn-Teller_Distortions](https://chem.libretexts.org/Bookshelves/Inorganic_Chemistry/Supplemental_Modules_and_Websites_(Inorganic_Chemistry)/Coordination_Chemistry/Structure_and_Nomenclature_of_Coordination_Compounds/Coordination_Numbers_and_Geometry/Jahn-Teller_Distortions). [Accessed 13-06-2024].
- [95] D. Moon and J.-H. Choi. “Crystal structure of bis[bis(1,4,7-triazacyclononane- κ^3 N,N',N'')chromium(III)] tris(tetrachloridozincate) monohydrate from synchrotron X-ray data”. *Acta Crystallographica Section E* **75**, 428 (2019).
- [96] F. Aquilante, J. Autschbach, R. K. Carlson, L. F. Chibotaru, M. G. Delcey, L. De Vico, I. Fdez. Galván, N. Ferré, L. M. Frutos, L. Gagliardi, M. Garavelli, A. Giussani, C. E. Hoyer, G. Li Manni, H. Lischka, D. Ma, P. A. Malmqvist, T. Müller, A. Nenov, M. Olivucci, T. B. Pedersen, D. Peng, F. Plasser, B. Pritchard, M. Reiher, I. Rivalta, I. Schapiro, J. Segarra-Martí, M. Stenrup, D. G. Truhlar, L. Ungur, A. Valentini, S. Vancoillie, V. Veryazov, V. P. Vysotskiy, O. Weingart, F. Zapata, and R. Lindh. “Molcas 8: New capabilities for multiconfigurational quantum chemical calculations across the periodic table”. *Journal of Computational Chemistry* **37**, 506 (2016).
- [97] F. Aquilante, J. Autschbach, A. Baiardi, S. Battaglia, V. A. Borin, L. F. Chibotaru, I. Conti, L. De Vico, M. Delcey, I. Fdez. Galván, N. Ferré, L. Freitag, M. Garavelli, X. Gong, S. Knecht, E. D. Larsson, R. Lindh, M. Lundberg, P. A. Malmqvist, A. Nenov, J. Norell, M. Odellius, M. Olivucci, T. B. Pedersen, L. Pedraza-González, Q. M. Phung, K. Pierloot, M. Reiher, I. Schapiro, J. Segarra-Martí, F. Segatta, L. Seijo, S. Sen, D.-C. Sergentu, C. J. Stein, L. Ungur, M. Vacher, A. Valentini, and V. Veryazov. “Modern quantum chemistry with [Open]Molcas”. *The Journal of Chemical Physics* **152**, 214117 (2020).
- [98] K. Wieghardt, W. Walz, B. Nuber, J. Weiss, A. Ozarowski, H. Stratemeier, and D. Reinen. “Crystal structure of bis[bis(1,4,7-triazacyclononane)nickel(III)] dithionate heptahydrate and its single-crystal epr spectrum”. *Inorganic Chemistry* **25**, 1650 (1986).
- [99] H. J. Kueppers, A. Neves, C. Pomp, D. Ventur, K. Wieghardt, B. Nuber, and J. Weiss. “Electron-transfer barriers in cobalt(III) and cobalt(II) bis complexes of 1,4,7-triazacyclononane (tacn) and 1,4,7-trithiacyclononane (ttcn). crystal structures of [Co(II)(tacn)₂](H₂O)₂ and of [Co(III)(ttcn)₂](ClO₄)₃”. *Inorganic Chemistry* **25**, 2400 (1986).
- [100] R. D. Adamson, J. P. Dombroski, and P. M. W. Gill. “Efficient calculation of short-range coulomb energies”. *Journal of Computational Chemistry* **20**, 921 (1999).
- [101] S. Refaely-Abramson, R. Baer, and L. Kronik. “Fundamental and excitation gaps in molecules of relevance for organic photovoltaics from an optimally tuned range-separated hybrid functional”. *Phys. Rev. B* **84**, 075144 (2011).
- [102] O. S. Bokareva, O. Baig, M. J. Al-Marri, O. Kühn, and L. González. “The effect of n-heterocyclic carbene units on the absorption spectra of Fe(II) complexes: a challenge for theory”. *Phys. Chem. Chem. Phys.* **22**, 27605 (2020).

- [103] T. Körzdörfer and N. Marom. “Strategy for finding a reliable starting point for G_0W_0 demonstrated for molecules”. *Phys. Rev. B* **86**, 041110 (2012).
- [104] M. Dorn, J. Kalmbach, P. Boden, A. Kruse, C. Dab, C. Reber, G. Niedner-Schatteburg, S. Lochbrunner, M. Gerhards, M. Seitz, and K. Heinze. “Ultrafast and long-time excited state kinetics of an nir-emissive vanadium(iii) complex i: synthesis, spectroscopy and static quantum chemistry”. *Chem. Sci.* **12**, 10780 (2021).
- [105] L. G. Gagliardi, C. B. Castells, C. Rafols, M. Roses, and E. Bosch. “Static dielectric constants of acetonitrile/water mixtures at different temperatures and debye hückel a and a₀b parameters for activity coefficients”. *Journal of Chemical & Engineering Data* **52**, 1103 (2007).
- [106] B. O. Roos, R. Lindh, P. Åke Malmqvist, V. Veryazov, and P. O. Widmark. *Multiconfigurational SCF Theory*. John Wiley and Sons, Ltd (2016).
- [107] H. F. Schaefer. *Methods of Electronic Structure Theory*. Springer New York, NY (2013).
- [108] S. Mai, F. Plasser, M. Pabst, F. Neese, A. Köhn, and L. González. “Surface hopping dynamics including intersystem crossing using the algebraic diagrammatic construction method”. *The Journal of Chemical Physics* **147**, 184109 (2017).
- [109] M. Sala, S. Guérin, and F. Gatti. “Quantum dynamics of the photostability of pyrazine”. *Phys. Chem. Chem. Phys.* **17**, 29518 (2015).
- [110] T. Suzuki. “Ultrafast internal conversion of aromatic molecules studied by photoelectron spectroscopy using sub-20 fs laser pulses”. *Molecules (Basel, Switzerland)* **19**, 2410 (2014).
- [111] “D_{2h} point group”. <https://www.webqc.org/symmetrypointgroup-d2h.html>. [Accessed 03-07-2024].
- [112] I. Yamazaki, T. Murao, T. Yamanaka, and K. Yoshihara. “Intramolecular electronic relaxation and photoisomerization processes in the isolated azabenzene molecules pyridine, pyrazine and pyrimidine”. *Faraday Discuss. Chem. Soc.* **75**, 395 (1983).
- [113] I. C. Walker and M. H. Palmer. “The electronic states of the azines. iv. pyrazine, studied by vuv absorption, near-threshold electron energy-loss spectroscopy and ab initio multi-reference configuration interaction calculations”. *Chemical Physics* **153**, 169 (1991).
- [114] J. P. Zobel, A. Kruse, O. Baig, S. Lochbrunner, S. I. Bokarev, O. Kühn, L. González, and O. S. Bokareva. “Can range-separated functionals be optimally tuned to predict spectra and excited state dynamics in photoactive iron complexes?”. *Chem. Sci.* **14**, 1491 (2023).
- [115] Q. Peng, Y. Yi, Z. Shuai, and J. Shao. “Excited state radiationless decay process with Duschinsky rotation effect: Formalism and implementation”. *The Journal of Chemical Physics* **126**, 114302 (2007).
- [116] G. Tian, S. Duan, G.-P. Zhang, W. Hu, and Y. Luo. “The effect of duschinsky rotation on charge transport properties of molecular junctions in the sequential tunneling regime”. *Phys. Chem. Chem. Phys.* **17**, 23007 (2015).
- [117] F. Bruneval, S. M. Hamed, and J. B. Neaton. “A systematic benchmark of the ab initio Bethe-Salpeter equation approach for low-lying optical excitations of small organic molecules”. *The Journal of Chemical Physics* **142**, 244101 (2015).

Acknowledgements

Finally, I would like to say thank you to all the people who supported me throughout my entire academic career.

Starting with Professor Kühn, who gave me the opportunity to work in his group, who supervised me during my work, and who had to endure the countless questions I had throughout the past year. I was always welcomed open-hearted, which I truly appreciate.

Special thanks go of course to all members of the entire molecular quantum dynamics group, who always supported me with technical problems or gave me advice. In particular, I would like to thank Lorenz Dettmann, Andy Kaiser, Olga Bokareva, Sergey Bokarev, Hamada Rezk, Ashour Ahmed, and Mohammad Sadegh Talezadehlari.

I also have to thank all the people who worked with me on this project. Especially, I would like to express my gratitude to Christof Holzer and Sebastian Mai for their in-depth support, when performing calculations. Special recognition also goes to the groups of Professor Lochbrunner and Professor Seidel, who supplied me with recommendations and/or experimental data.

At last, I would like to thank all of my family and friends who supported me in different manners. Without your help, this work would not have been possible.

Statement of Authorship

I hereby certify that I have written this thesis independently and that I have not used any sources and aids other than those specified. I certify that the electronic version submitted corresponds to the printed copies.

Rostock, 30th of August 2024

Florian Bogdain